Modelling the spatial distribution, direct radiative forcing and impact of mineral dust on boundary layer dynamics

---

A thesis

submitted in partial fulfilment

of the requirements for the degree

of

Doctor of Philosophy in Environmental Science

by

Omid Alizadeh Choobari

May 9, 2013

*To my loving wife **Parya** for her support and consideration all these years.*

*To my caring and loving mother and father **Monir** and **Parviz**, may their souls rest in peace.*

*To my dear in-laws **Hassan** and **Parvin** for adopting me as a son.*

Acknowledgments

Thanks to my PhD supervisors **Dr Peyman Zawar-Reza** and **Prof. Andrew Sturman** whose expertise, understanding and patience added considerably to my experience as a graduate and future researcher. In particular, I greatly appreciate Prof. Andrew Sturman's timely review of each chapter of the thesis and the published papers. I have been able to present the results of my research at many conferences within New Zealand, Australia and the United States, which would not have been possible without the support of my PhD supervisors. Many thanks go to **Tony Dale** from the High-Performance Computing Centre and **Steven Skyes**, the departmental system administrator, for resolving my computer issues. Thanks to **Anna Petrie**, the department administrator, who was always available for all types of administrative purposes. Thanks to my dear friends I had the fortune to meet during my study at the University of Canterbury: **Arash**, **Basit**, **Colin**, **Iman**, **Marwan**, **Mohammad**, **Sandipan**, **Zahid** and other students at the University of Canterbury I had the opportunity to meet. Thanks to the Foundation for Research, Science and Technology and the National Institute for Water and Atmospheric Research (New Zealand) for providing financial support throughout the duration of this work.

Abbreviations

AOD	Aerosol optical depth	-
AERONET	AErosol RObotic NETwork	-
α	Vegetation mask	-
β	Fraction of clay content	-
CAD	Cloud-aerosol discrimination	-
CALIOP	Cloud-Aerosol Lidar with Orthogonal Polarization	-
CALIPSO	Cloud-Aerosol Lidar and Infrared Pathfinder Satellite Observation	-
CBM-Z	Carbon-Bond Mechanism version Z	-
CCN	Cloud condensation nuclei	-
DOD	Dust optical depth	-
DUSTRAN	Dust transport	-
EDGAR	Emission Database for Global Atmospheric Research	-
ENSO	El Niño Southern Oscillation	-
f	Coriolis parameter	s^{-1}
f_w	Soil wetness factor	-
FNL	Final Analysis	-
GOCART	Goddard Global Ozone Chemistry Aerosol Radiation and Transport	-
IN	Ice nuclei	-
ITCZ	InterTropical Convergence Zone	-
LSM	land-surface models	-
MISR	Multiangle Imaging SpectroRadiometer	-
MODIS	Moderate Resolution Imaging Spectrometer	-
MOSAIC	Model for Simulating Aerosol Interactions and Chemistry	-
MYJ	Mellor-Yamada-Janjic	-

N^2	Brunt Vaisala frequency	-
NCAR	National Center for Atmospheric Research	-
NCEP	National Centers for Environmental Predictions	-
PBL	Planetary boundary layer	-
PM_{10}	Particle matter less than 10 μm in diameter	μg m^{-3}
$PM_{2.5}$	Particle matter less than 2.5 μm in diameter	μg m^{-3}
RETRO	RE-analysis of the TRO-pospheric (chemical composition)	-
ρ	Air density	g cm^{-3}
$Ri_{b,cr}$	Critical bulk Richardson number	-
Ro	Rossby number	-
RUC	Rapid Update Cycle	-
τ	Shear stress	g cm^{-1} s^{-2}
TKE	Turbulent kinetic energy	m^2 s^{-2}
TOA	Top of the atmosphere	
u_*	Friction velocity	cm s^{-1}
u_{10}	Wind speed at 10 m	cm s^{-1}
$w(\%)$	Gravimetric soil moisture	-
WRF/Chem	Weather Research and Forecasting with Chemistry	-
YSU	Yonsei University	-
z_0	Roughness length	m

Preface

All new investigations can uncover the boundless complexities and unknowns of the science. The present thesis is the result of a three year research programme conducted by the author to investigate mineral dust distribution and its direct radiative forcing over Australia to fulfil doctoral degree requirements in Environmental Science at the University of Canterbury. The author has benefited from detailed comments of specialists in the field which have helped to improve the investigation results. However, this does not mean that the current study is free of possible shortcomings, rather the author believes that it is a small step in endless scientific investigation. If this small step is considered to provide a few new insights in the investigation of mineral dust distribution and its direct radiative forcing, the author will be delighted.

My initial interest in the impacts of mineral dust on the radiation budget and atmospheric dynamics goes back to an interesting discussion with Dr P. Zawar-Reza who pointed out the importance of suspended dust in the atmosphere in modulating wind speed. In essence, while wind speed is a major contributor to dust emission over susceptible lands, suspended dust in turn has a feedback on wind speed through its radiative forcing. Later on, I realized the importance of the influence of radiative forcing by mineral dust on other atmospheric characteristics, as well as the climate system. Significant lack of investigation in this field over the Australian region, and my firm belief that radiative forcing of atmospheric aerosols should be considered in weather and climate studies motivated me to do my PhD research in this field. Such forcing has been included in the Weather Research and Forecasting with Chemistry (WRF/Chem) regional model, the first community (a model that is publicly available) online-coupled model in the United States. It considers a wide range of aerosol schemes with both sectional and modal approaches. Consequently, I selected the WRF/Chem model as a framework for the research, while satellite and ground-based measurements have been used as complements to the model simulations. Since starting this research in April 2010, the degree of coupling of atmospheric and chemistry processes in the WRF/Chem model has gradually increased. Accordingly,

the simulation results in each chapter are based on the last version of the model at the time of completing the analysis. For example, estimates of the longwave direct radiative forcing by mineral dust over Australia is presented in Chapter 5, when this feature was included in the model.

Three papers from the results of this research programme have already been published and one paper is currently under review. While my PhD supervisors' doors were always open for any help and their comments have helped enormously in examining the quality of the final product, I have made the greatest contribution to this research and the published papers, including configuration and running the model simulations, gathering observational ground-based and remote sensing data, post-processing and analysing the results, as well as writing the papers and thesis. The following published or under-review papers are based on the results of the current research programme:

- Most of Chapter 2 has been submitted as a review paper to *Meteorology and Atmospheric Physics*: **Alizadeh Choobari, O., P. Zawar-Reza and A. Sturman (2013), The global distribution of mineral dust and its impacts on the climate system: A review**

- Chapter 3 has been peer reviewed and published in the *Journal of Geophysical Research-Atmospheres*: **Alizadeh Choobari, O., P. Zawar-Reza and A. Sturman (2012), Atmospheric forcing of the three-dimensional distribution of dust particles over Australia: A case study. *J. Geophys. Res., 117*, D11206, doi:10.1029/2012JD017748.**

- Chapter 4 has been peer reviewed and published in *Atmospheric Environment*: **Alizadeh Choobari, O., P. Zawar-Reza and A. Sturman (2012), Feedback between wind-blown dust and planetary boundary- layer characteristics: Sensitivity to boundary and surface layer parameterizations. *Atmos. Environ., 61*, 294-304, doi:10.1016/j.atmosenv.2012.07.038.**

- Chapter 5 has been peer reviewed and published in *Tellus B*: **Alizadeh Choobari, O., P. Zawar-Reza and A. Sturman (2013), Simulation of the spatial distribu-**

tion of mineral dust and its direct radiative forcing over Australia. ***Tellus B, 65*****, 19856, doi:10.3402/tellusb.v65i0.19856.**

Preface to Chapter 2

This chapter is entitled: "Mineral Dust Overview" and is divided into three main sections. The first section provides an overview of mineral distribution in the atmosphere on a global scale, including identifying the major potential sources of dust around the globe and estimates of dust emission from these sources, as well as transport and deposition processes affecting dust particles. The second section reviews current understanding of the radiative effects of mineral dust, including the direct radiative effect through scattering and absorption of shortwave and longwave radiation, the semi-direct effect through burning off of cloud droplets, and the indirect effect through impacts on the optical properties and lifetime of clouds, as well as on precipitation processes. Finally, the influence of direct radiative forcing by dust aerosols on surface energy exchanges is discussed in the last section.

Preface to Chapter 3

This chapter is entitled: "Australian Dust Transport." It explores the frontogenetic evolution of the boundary layer and its contribution to horizontal and vertical distribution of mineral dust using the WRF/Chem regional model complemented by available observations, including the Moderate Resolution Imaging Spectroradiometer (MODIS) and Cloud-Aerosol Lidar with Orthogonal Polarization (CALIOP) satellite datasets, as well as ground-based measurements. This study aims to address a number of key questions. First, what are the exit pathways of Australian dust during severe dust events and can the WRF/Chem model adequately simulate the spatial distribution of dust during such events? To address this question, model results were analysed and compared with available satellite datasets and ground-based measurements in Australia. Second, what atmospheric

processes are responsible for the three-dimensional distribution of Australian dust during the passage of a cold front associated with an intense extratropical cyclone? This question cannot be addressed by using observations alone, so that numerical modelling represents a useful tool for extending knowledge of such processes. Finally, what is the vertical and horizontal extent of Australian dust plumes during transport? This question has been addressed using available satellite data in combination with the model results.

Preface to Chapter 4

This chapter is entitled: "Feedback Between Windblown Dust and Boundary-layer Characteristics." It investigates dust radiative feedback effects on boundary layer dynamics using the WRF/Chem regional model. Furthermore, this study examines the sensitivity of the direct radiative effect of dust associated with two different planetary boundary layer (PBL) schemes: the Yonsei University (YSU) scheme with both Noah and RUC (Rapid Update Cycle) land-surface models (LSMs), and the Mellor-Yamada-Janjic (MYJ) scheme. To this end, initially two simulations were performed, both using the Monin-Obukhov surface layer scheme and the unified Noah LSM (referred to as YSU-Noah). The first comprised a model set up that did not include the direct radiative effect of aerosols, despite the inclusion of dust. This model run was used as a control experiment. The second interactive experiment simulated the two-way interaction between atmospheric processes and aerosols, so that meteorological variables respond to the direct radiative effect of aerosols. Radiative forcing by mineral dust and dynamic atmospheric responses were calculated from the differences between the results of the two simulations (referred to as an anomaly).

In addition, four other simulations were conducted. Two of them employed the YSU PBL parameterization with the Monin-Obukhov surface layer scheme and the RUC LSM (referred to as YSU-RUC). The radiative forcing of mineral dust was turned off and on for these two simulations, respectively. Two other experiments employed the MYJ PBL parameterization, including the Monin-Obukhov (Janjic Eta) surface layer scheme and

the unified Noah LSM (referred to as MYJ-Noah). Again, radiative forcing by dust for these two simulations was turned off and on, respectively.

Preface to Chapter 5

This chapter is entitled: "Direct Radiative Forcing by Dust over Australia." It aims to improve understanding of the regional climate impacts of mineral dust over Australia. To this end, multi-month simulations that include both shortwave and longwave direct radiative forcing of mineral dust were conducted using the WRF/Chem model. The objective of this particular study is twofold: (1) to observe and simulate monthly variation of mineral dust over Australia during austral spring and summer when dust outbreaks over central eastern Australia are most frequent; and (2) to simulate shortwave and longwave direct radiative forcing of mineral dust at the surface and top of the atmosphere (TOA).

Abstract

Mineral dust aerosols, the tiny soil particles in the atmosphere, play a key role in the atmospheric radiation budget through their radiative and cloud condensation nuclei effects. It is therefore important to evaluate the radiative forcing of mineral dust and subsequent changes in atmospheric dynamics. The Weather Research and Forecasting with Chemistry (WRF/Chem) regional model with the integrated dust modules and available observations have been used to investigate the three-dimensional distribution of mineral dust over Australia. Additionally, the WRF/Chem model was used to estimate the direct radiative forcing by mineral dust over Australia. Particular emphasize has been given to direct radiative feedback effect of mineral dust on boundary layer dynamics. Two dust emission schemes embedded within the WRF/Chem model have been utilized in this study: the dust transport (DUSTRAN) and the Goddard Global Ozone Chemistry Aerosol Radiation and Transport (GOCART) schemes. The refractive index of mineral dust depends on the mineralogy, size and composition of dust over a given region. The refractive index of mineral dust for shortwave radiation was considered to be wavelength independent and set based on previous mineralogical studies over North Africa and Australia. However, the refractive index of mineral dust for longwave radiation was considered to be wavelength dependent and to vary for 16 longwave spectral bands. Model results were compared with observations to validate the performance of the model, including satellite datasets from the Moderate Resolution Imaging Spectroradiometer (MODIS), Multi-angle Imaging SpectroRadiometer (MISR) and Cloud-Aerosol Lidar with Orthogonal Polarization (CALIOP), as well as ground-based measurements obtained from air quality monitoring sites over Australia. The major results can be summarized as follows: (1) Lake Eyre Basin is the most important source of dust in Australia, with a peak activity identified to be during austral spring and summer, and dust emission within the basin is often associated with the passage of dry cold fronts; (2) Mineral dust from Lake Eyre Basin can be transported long distances to southeastern Australia in association with eastward propagating frontal systems, reaching as far as New Zealand and beyond, and to northern tropical Australia by postfrontal southerly winds, and subsequently towards northwestern Australia and the

Indian Ocean by southeasterly trade winds; (3) Australian dust plumes are mainly transported in the lower atmosphere, although variation of boundary layer depth during the passage of cold frontal systems, as well as ascending motion at the leading edge of these systems and descending motion where postfrontal anticyclonic circulation is dominant contribute to the vertical extent of mineral dust aerosols; (4) the shortwave direct radiative effect of mineral dust results in cooling of the atmosphere from the surface to near the boundary layer top, but warming of the boundary layer top and lower free atmosphere; (5) changes in the vertical profile of temperature result in an overall decrease of wind speed in the lower boundary layer and an increase within the upper boundary layer and lower free atmosphere; (6) the longwave warming effect of mineral dust partly offsets its shortwave cooling effect at the surface. This compensation is significantly larger over and immediately downwind of dust source regions where coarse particles are more abundant, as they have stronger interaction with longwave radiation emitted from the Earth's surface; (7) both shortwave and longwave radiative forcing by mineral dust was found to have a diurnal variation in response to changes in solar zenith angle and in the intensity of longwave radiation, respectively; (8) the absorptive nature of dust was shown to be associated with the shortwave heating of the atmosphere; (9) on the other hand, longwave cooling of the atmosphere was identified because absorption of longwave radiation by dust is less than its emission to the surface and top of the atmosphere (TOA).

Contents

List of Figures

List of Tables

Chapter 1

Introduction

The atmosphere is a mixture of gases and aerosols surrounding the Earth. The gaseous component is primarily composed of molecular nitrogen (78.1% volume mixing ratio) and oxygen (20.9% volume mixing ratio), but also a range of trace gases, including water vapour, carbon dioxide, nitrogen oxides, ozone and methane (*Korsholm*, 2009). Despite the predominance of nitrogen and oxygen, these gases are of little climatic importance. In contrast, in spite of their relative scarcity, trace gases are radiatively important as they scatter, absorb and re-emit radiation. They are also chemically active and contribute to the gas-to-particle conversion processes (i.e. new particle formation by nucleation, condensation and coagulation of gaseous precursors; *Gillani and Wilson*, 1983). Aerosols, the tiny particles in the atmosphere from both natural and anthropogenic sources (including suspended particles of sea-salt, mineral dust, organic matter and smoke), are categorized into primary and secondary, and make a considerable, but complex contribution to the climate system through their radiative and cloud condensation nuclei effects (e.g. *McCormick and Ludwig*, 1967; *Hansen et al.*, 1997; *Gunn and Phillips*, 1957; *Ferek et al.*, 2000; *Rosenfeld*, 2000). Primary aerosols are solid or liquid particles that are emitted directly into the atmosphere, while secondary aerosols are often produced through gas-to-particle conversion processes (*Korsholm*, 2009).

Among the different components of aerosols in the atmosphere, wind-blown dust is emitted in large quantities over arid and semi-arid regions where alluvial sediments have been accumulated. Mineral dust, from both natural and anthropogenic sources, is the most abundant atmospheric aerosol component in terms of aerosol dry mass, contributing more than half of the total global aerosol burden (*Textor et al.*, 2006). It has a significant influence on the climate system directly through scattering and absorption of solar and infrared radiation (*McCormick and Ludwig*, 1967; *Miller and Tegen*, 1998), semi-directly through

changes in atmospheric temperature structure and the evaporation rate of cloud droplets (i.e. the cloud burning effect; *Hansen et al.*, 1997; *Ackerman et al.*, 2000; *Koren et al.*, 2004), and indirectly in a complex way through impact on optical properties of clouds (i.e. enhancing cloud reflectance by increasing total droplet cross-sectional area; *Gunn and Phillips*, 1957; *Liou and Ou*, 1989) and suppression (*Ferek et al.*, 2000; *Rosenfeld*, 2000) or enhancement (*Andreae et al.*, 2004) of precipitation formation. Additionally, mineral dust aerosols degrade air quality (*Prospero*, 1999) and adversely affect human health (*Pope et al.*, 2002). Dust is also a source of iron which is a nutrient for phytoplankton (*Fung et al.*, 2000). Therefore, it can affect marine biogeochemical processes, thereby contributing to the oceanic uptake of carbon (*Jickells et al.*, 2005).

The most important sources of mineral dust aerosols are located in the Northern Hemisphere "dust belt", primarily over the Sahara and Sahel regions in North Africa, the Middle East, as well as Southwest, Central and East Asia (*Prospero et al.*, 2002; *Ginoux et al.*, 2012). Suspended dust from these major sources can be transported long distances (Long-Range Transboundary Air Pollution (LRTAP)) and have considerable influence on the local, regional and global climate system. However, there are other relatively small sources of dust that influence the climate system at least on local and regional scales. Among them, Australia is the most important source of dust in the Southern Hemisphere (*Prospero et al.*, 2002; *Ginoux et al.*, 2012), with an estimated annual dust emission of 61 Mt (*Ginoux et al.*, 2004). As such, there is a critical need to understand seasonal variation and transport pathways of Australian dust, as well as its optical properties. Yet, knowledge of the three-dimensional distribution of Australian dust is limited and contains high uncertainty. Specifically, the vertical structure of dust plumes near the source regions and during the transport, and the physical mechanisms responsible for the observed vertical and horizontal distribution of Australian dust remain largely unknown. The lack of investigation is more pronounced in terms of the climate impacts of Australian dust, partly because investigation of the aerosols optical properties requires an aerosol model that is fully coupled with meteorology (*Grell et al.*, 2005), but also because unlike the "dust belt" of the Northern Hemisphere, Australian dust appears not to be considered an important

agent in modifying the Earth's climate system on a global scale, as it only accounts for about 5% of the global total dust emission (*Mitchell et al.*, 2010). However, mineral dust from Australia is an important component of the atmosphere that affects the regional climate through its radiative impacts. The rapid development of online and coupled aerosol-atmosphere models which have the ability to include radiative effects of aerosols (*Grell et al.*, 2005), as well as the advent of satellites with the capability for retrieving mineral dust over bright land surfaces (*Kahn et al.*, 2005), and recent field campaigns for identifying mineral composition of Australian dust (e.g. *Qin and Mitchell*, 2009; *Radhi et al.*, 2010) have improved our ability to better monitor mineral dust distribution and understand its optical properties over Australia.

The present study is therefore an effort to better understand the three-dimensional distribution of mineral dust, its direct radiative forcing (i.e. perturbation of the radiation balance due to scattering and absorption of shortwave and longwave radiation by mineral dust aerosols) and subsequent impacts on boundary layer dynamics over Australia using the Weather Research and Forecasting with Chemistry (WRF/Chem) regional model. The model results are complemented by ground-based and satellite observations to investigate mineral dust distribution and monthly variation of aerosol optical depth (AOD) over Australia. Investigation of radiative effects of Australian dust has been limited to a few field campaigns by *Qin and Mitchell* (2009) and *Radhi et al.* (2010) to identify its absorption properties and iron content. Therefore, to our knowledge the present study is the first attempt in quantifying the direct radiative effect of mineral dust and its subsequent impact on atmospheric dynamics over Australia on a regional scale.

Methodology

The WRF/Chem model is used in the present study. It is the most advanced online coupled regional model in terms of the number of available schemes, complexity of the aerosol and chemical schemes, as well as the coupling between gases, aerosols and meteorology (*Zhang*, 2008). It incorporates a chemistry module that simultaneously simulates the

emission, turbulent diffusion, transport and transformation of trace gases and aerosols, their removal processes, and their radiative effects (*Grell et al.*, 2005). Two aerosol schemes embedded within the WRF/Chem model have been used in the present study: (1) the Model for Simulating Aerosol Interactions and Chemistry (MOSAIC) (*Zaveri et al.*, 2008), with eight sectional bins, that incorporates the dust transport (DUSTRAN) scheme developed by *Shaw et al.* (2008); and (2) the Goddard Global Ozone Chemistry Aerosol Radiation and Transport (GOCART) aerosol module, with five discrete size bins of dust particles, that incorporates the dust scheme developed by *Ginoux et al.* (2001, 2004). The MOSAIC aerosol module is more complicated than GOCART and is the most actively developed aerosol module in WRF/Chem (*Li et al.*, 2012), but it requires more computing time. As a result, the MOSAIC aerosol module was applied to investigate both the three-dimensional and direct radiative forcing of Australian dust for an individual severe dust event (Chapters 3 and 4), while the GOCART aerosol module was used to simulate the long term distribution and direct radiative forcing of mineral dust over Australia (Chapter 5). A detailed description of these aerosol schemes are provided in Chapters 3 to 5. An individual dust event of 22-23 September 2009 has been selected in Chapters 3 and 4 as there was severe drought and low rainfall prior to this event, causing one of the most severe dust events that have occurred over Australia since 1940 (*Leys et al.*, 2011). Additionally, a series of long-term simulations was carried out during austral spring and summer (discussed in Chapter 5) when dust outbreaks over central eastern Australia are most frequent. As there was a severe drought over Australia associated with the establishment of the El Niño Southern Oscillation (ENSO) phenomenon in 2009, simulations were conducted for the period September 2009 to February 2010.

This thesis is organized in the form of four main chapters (including mineral dust overview in Chapter 2), all of them are based on journal articles as outlined at the beginning of each chapter. This implies some overlap in the text, in particular with respect to the model description in each chapter. The aim of the thesis is to simulate mineral dust distribution, including its vertical extension, and provide estimates of direct radiative forcing of mineral dust and subsequent impacts on boundary layer dynamics over the Australian region.

The semi and indirect effects of mineral dust are not investigated in this study. The thesis is organized as follows. Chapter 2 provides an overview of mineral dust distribution on a global scale and its radiative and cloud condensation nuclei effects. Transport pathways and vertical distribution of Australian dust during a severe dust event on 22-23 September 2009 is the subject of Chapter 3. The dust event was caused by the passage of an extratropical cold frontal system across central Australia. As passage of cold fronts is the main reason for dust storms over central Australia, the present study provides typical pathways of dust plumes over Australia and their vertical distribution during such events. The transport pathways of Australian dust are investigated in the thesis as there is still uncertainty in terms of exit pathways of Australian dust and the directions in which most of the dust is being transported. In particular, the vertical distribution of mineral dust aerosols from Australia and the height at which they are being transported was largely unknown. It is noteworthy that the vertical extent of mineral dust is also an important factor for determining direct radiative forcing of dust. Therefore, the vertical extent of dust and its driving mechanisms need to be discussed before providing estimates of the direct radiative forcing of dust in the following chapters. Chapter 4 discusses the impact of mineral dust on atmospheric dynamics over Australia as a result of its shortwave direct radiative forcing. As the impact of mineral dust on atmospheric characteristics is more detectable during a dust event when aerosols within the atmosphere are more abundant, a series of simulations have been conducted for the severe dust event of 22-23 September 2009. Nevertheless, monthly and seasonal variation of mineral dust distribution and its associated unexplored direct radiative effect also need to be investigated for Australian region. Consequently, monthly variation of AOD over Lake Eyre Basin throughout the year, and estimates of shortwave and longwave direct radiative forcing by mineral dust during spring and summer have been discussed in Chapter 5. An overall conclusion is provided at the end of the thesis in Chapter 6.

Chapter 2

Mineral Dust Overview

Alizadeh Choobari, O., P. Zawar-Reza and A. Sturman (2013), The global distribution of mineral dust and its impacts on the climate system: A review. Under review in *Meteorology and Atmospheric Physics*.

2.1 Dust Aerosols in the Atmosphere

Mineral dust is the most abundant atmospheric aerosol component in terms of aerosol dry mass, contributing more than half of the total global aerosol burden (*Textor et al.*, 2006), with an estimated global annual average atmospheric dust load ranging from 8 to 35 Mt, and an annual dust emission ranging from 1000 to 3000 Mt (*Zender et al.*, 2004). Therefore, its contribution to the climate system and atmospheric environment is of considerable significance, underlining the essential need for investigation into the origin of dust aerosols, their transport pathways in the atmosphere and deposition processes, and radiative forcing and impact on the hydrological cycle.

2.1.1 Dust Sources

Due to its global coverage, satellite remote sensing is the best tool for investigating the spatial and temporal distribution of mineral dust aerosols around the globe. Remote sensing analysis has shown that major sources of mineral dust are located in arid regions, including deserts, semi-arid deserts, dry lake beds and ephemeral channels, where annual rainfall is extremely low (Goudie and Middelton, 2006) and substantial amounts of alluvial sediment have been accumulated over years (*Prospero et al.*, 2002; *Ginoux et al.*, 2012). In addition to these natural sources, human-induced disturbance of the land sur-

face and climate variability (i.e. the anthropogenic sources for mineral dust) (*Prospero et al.*, 2002; *Tegen et al.*, 2004) has also contributed to an increase of mineral dust aerosols within the atmosphere.

Long-term seasonally averaged aerosol optical depth (AOD, column integrated aerosol amount from the surface to the top of the atmosphere) at 0.55 μm over the 11-year period (2001-2011) obtained from the Multiangle Imaging Spectroradiometer (MISR) satellite instrument is shown in Figure 2.1. The most important sources of dust are located in the Northern Hemisphere, primarily over the Sahara and Sahel regions in North Africa, the Middle East, and Southwest, Central and East Asia (*Prospero et al.*, 2002; *Ginoux et al.*, 2012). Note that high AOD values along the coast of the Gulf of Guinea near the western coast of Africa (in winter and spring), and southern Africa and Amazonia (in austral winter (JJA) and spring (SON)), as well as over southern China (in summer) and the Indonesian region are mostly attributed to biomass burning. The Sahara is the largest natural source of dust on Earth (see Figure 2.1), with an estimated global emission of 670 Mt yr[1] (*Rajot et al.*, 2008). Saharan dust accounts for 40-70% of the global annual emission (*Engelstaedter et al.*, 2006). The maximum aerosol concentration is in the summer period (JJA) over North Africa, the Middle East and Southwest Asia (*Goudie and Middelton*, 2006), while East Asia (The Gobi and Taklimakan deserts) has a spring peak (MAM, *Sun et al.* (2001)). Some relatively small sources of mineral dust are located in the Southern Hemisphere, including desert areas in southern Africa, South America and Australia, with dust emissions estimated to be 22, 55 and 61 Mt yr^{-1}, respectively (*Ginoux et al.*, 2004). For example, Lake Eyre Basin in central Australia is the most important source of dust in the Southern Hemisphere (*Prospero et al.*, 2002; *Ginoux et al.*, 2012), with more frequent dust emission occurring in austral spring-summer (September to February), while Patagonia is the most important source of dust in South America (*Gaiero et al.*, 2007) and Botswana is an active source of dust in central southern Africa (*Prospero et al.*, 2002). The total dust emission in the Southern Hemisphere only accounts for about 6.7% of the total global dust emission and is estimated to be about 138 Mt yr^{-1}, which is substantially lower than the total dust emission from the Northern Hemisphere with an estimated value

of 1935 Mt yr^{-1} (*Ginoux et al.*, 2004).

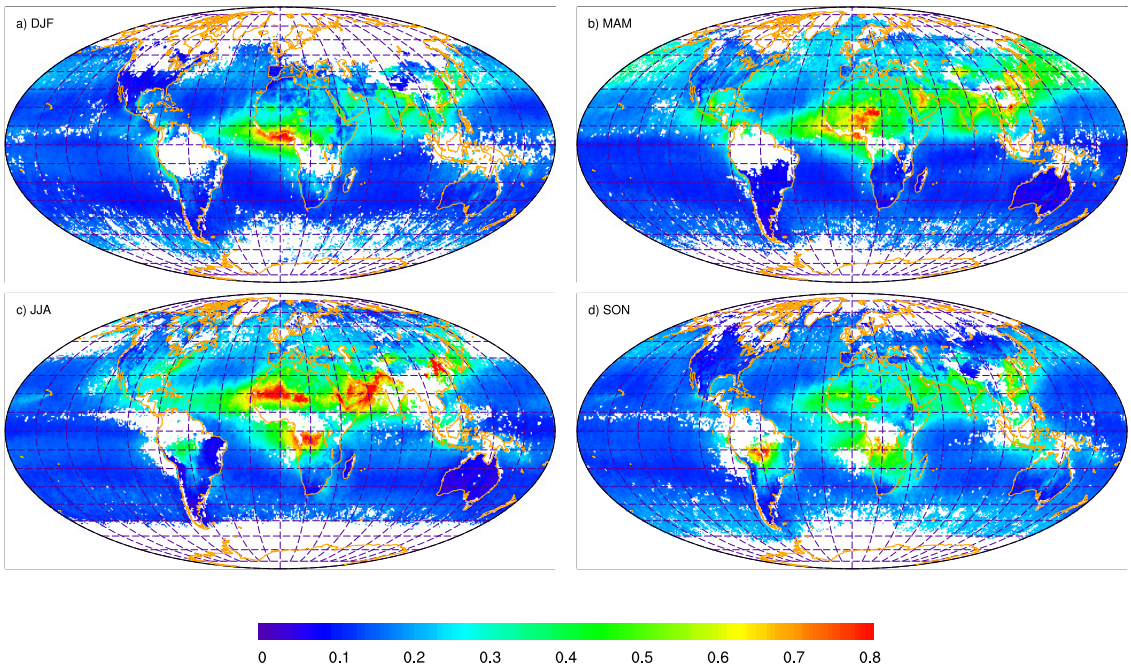

Figure 2.1. Seasonally averaged AOD at 0.55 μm from 2001 to 2011 retrieved from the Multiangle Imaging Spectroradiometer (MISR) in (a) DJF, (b) MAM, (c) JJA and (d) SON.

Mineral dust is produced from both natural and anthropogenic sources. Natural source regions are primarily deserts, semi-arid deserts and dry lake beds, but also areas with extreme soil moisture deficit and reduced vegetation cover. Lack of vegetation cover and soil dryness are associated with areas receiving small amounts of rainfall, and this is reflected in dust source regions such as over the Western Sahara (*Goudie and Middelton*, 2006) and the Sistan Basin in eastern Iran (*Mansoori*, 1995), where annual precipitation is less than 100 mm.

In addition to natural sources, anthropogenic sources of mineral dust from disturbance of the land surface and climate variability due to human activities can also significantly increase dust entrainment (*Prospero et al.*, 2002; *Tegen et al.*, 2004). Indeed, *Tegen and Fung* (1995) estimated that between 30-50% of the atmospheric dust loading originates from disturbed land, while the *Sokolik and Toon* (1996) study indicated that 20% of the atmospheric suspended dust is caused by such sources. Some other studies suggest that

anthropogenic dust has a much lower contribution to the total atmospheric dust burden. For example, *Tegen et al.* (2004) estimated that less than 10% of the atmospheric dust burden comes from agricultural areas. Even if the lower estimate is more realistic, the contribution of anthropogenic sources of mineral dust is still a major concern as it is expected to increase in the future in response to greater human impact on changes in land use, such as through agriculture, deforestation and overgrazing (*Moulin and Chiapello*, 2006).

2.1.2 Dust Transport

Once in the atmosphere, dust particles can be transported over long distances (as shown in Figure 2.1) by prevailing winds, suggesting that they are constituents of atmospheric aerosols far from source regions. In particular, dust aerosols can be transported an extraordinarily long distance when they are lifted up to the upper troposphere by a warm conveyor belt mechanism (*Eguchi et al.*, 2009). Mineral dust particles from North Africa are carried by the tropical easterly trade winds across the tropical Atlantic to the Caribbean, Central America and United States in summer (*Perry et al.*, 1997; *Griffin et al.*, 2002; *Prospero and Lamb*, 2003), as well as being spread westward as far away as South America during spring and winter (see Figure 2.1; *Griffin et al.*, 2002). It has also shown that mineral dust aerosols are occasionally transported more than one full circuit around the globe (*Uno et al.*, 2009). Using the MODIS data, *Kaufman et al.* (2005) estimated that 240 ± 80 Tg of African dust are transported over the Atlantic Ocean annually. The transported dust fertilizes the Atlantic phytoplankton (*Jickells et al.*, 2005) and the Amazon rain forest (*Kaufman et al.*, 2005; *Koren et al.*, 2006). During summer the Saharan Air Layer (SAL) containing African dust has been observed above the marine boundary layer of the Atlantic Ocean at 1-6 km height (*Tesche et al.*, 2011). Massive summer dust plumes over the Arabian Peninsula are also carried towards the Arabian Sea (*Prospero et al.*, 2002) by the mid-latitude westerlies. Dust aerosols originating from sources of dust in East Asia are transported by mid-latitude prevailing westerlies across the Pacific Ocean and reach as

far east as the west coast of North America and beyond during spring (Figure 2.1; *Husar et al.*, 2001; *McKendry et al.*, 2001; *Takemura et al.*, 2002). *McKendry et al.* (2001) estimated that 38-55% of the observed PM_{10} at the Lower Fraser Valley, British Columbia, Canada is attributed to the transported dust from Asia. *Husar et al.* (2001) showed that on 15 April 1998, dust clouds originated from the Gobi desert crossed the Pacific Ocean in 5 days and reached as far east as British Columbia and California.

Mineral dust particles from smaller sources are less likely to be transported on an intercontinental scale, but they certainly influence downwind areas on a regional scale. For example, mineral dust aerosols originating from the Sistan Basin in Southwest Asia are carried by a strong northerly low level jet (LLJ) and reach the Oman Sea, approximately 800 km distance away, while mineral dust from the Karakum Desert in Central Asia influences northeastern Iran and northwestern Afganistan (*Alizadeh Choobari et al.*, 2013a,b). In the Southern Hemisphere, transport of Australian dust in a southeast direction by prefrontal northwesterly winds, in a northward direction by post-frontal southwesterly winds, and subsequently to northwestern Australia and the Indian Ocean by southeasterly trade winds has long been identified (*McGowan et al.*, 2000, 2005; *McGowan and Clark*, 2008; *Alizadeh Choobari et al.*, 2012a).

2.1.3 Dust Deposition

The atmospheric residence time for aerosols depends on their location in the atmosphere, with a longer atmospheric lifetime for aerosol particles in the upper troposphere than those in the lower troposphere (*Bolin et al.*, 1973). It is also size dependent, in which relatively large particles fall out rapidly near their sources due to the effect of gravity, while small particles can be suspended in the air for extended periods of time (*Bolin et al.*, 1973). All aerosols, however, are finally extracted from the atmosphere either by dry deposition because of gravitational settling and/or turbulent fluxes (*Shao*, 2008) or wet deposition through in-cloud (by cloud droplets) and below-cloud (by raindrops) scavenging (*Goncalves et al.*, 2002).

Large dust particles are primarily removed by dry deposition, while the smaller far-travelled ones are mostly scavenged through wet deposition (*Miller and Tegen*, 1998) because dry deposition is inefficient for particles less than 2 μm in diameter (*Seinfeld and Pandid*, 1997). Dry and wet deposition rates vary with season and location. Generally, in summer months when dust emission is higher and precipitation is lower, dry deposition is the major removal process. Furthermore, while dry deposition is a determinant factor in arid regions, wet deposition only dominates in regions with high amounts of rainfall (e.g. regions that are affected by the InterTropical Convergence Zone (ITCZ)) (*Goudie and Middelton*, 2006). Using the GOCART model, *Ginoux et al.* (2004) estimated that dry deposition accounts for around 90% of total removal of dust particles, while using the Global Transport Model of Dust (GMOD), *Yue et al.* (2009) indicated that about 67% of the total removal is through dry deposition. Another study by *Zender et al.* (2003) using the Mineral Dust Entrainment and Deposition (DEAD) model also indicated the dominance of dry (59%) over wet (41%) deposition. More significant contribution of dry deposition is partly due to the fact that substantial amounts of large dust particles are generally removed by dry deposition over and immediately downwind of dust source regions where annual rainfall is very low. Nevertheless, over oceanic regions wet deposition is dominant and estimated to be account for 89% of oceanic deposition (*Zender et al.*, 2003).

Due to these removal processes, tropospheric aerosols typically have a short atmospheric lifetime of 1 to 2 weeks (*Haywood and Boucher*, 2000). Their short atmospheric lifetime, combined with non-uniform distribution of aerosol sources contribute to a notable heterogeneous spatial distribution of aerosols around the globe (*IPCC*, 1994).

2.2 Radiative Forcing by Dust

2.2.1 Direct, Semi-direct and Indirect Effects of Dust Aerosols

The climate impacts of mineral dust aerosols have been identified as direct, semi-direct and indirect effects. They have an influence on radiative processes directly through absorption and scattering of shortwave and longwave radiation (*McCormick and Ludwig*, 1967; *Miller and Tegen*, 1998), semi-directly through changes in atmospheric temperature structure and burning off of cloud droplets due to absorption of radiation (*Hansen et al.*, 1997; *Ackerman et al.*, 2000; *Koren et al.*, 2004), and indirectly through impacts on the optical properties and lifetime of clouds (i.e. the first indirect effect) (*Gunn and Phillips*, 1957; *Liou and Ou*, 1989), and suppression (*Ferek et al.*, 2000; *Rosenfeld*, 2000) or enhancement (*Andreae et al.*, 2004) of precipitation processes (i.e. the second indirect effect). Note that mixed aerosols, that consist of mineral dust and other particles may have higher (dust + soot) (*Arimoto et al.*, 2006; *Garcia et al.*, 2011) and lower (dust + sulphate) absorption properties.

A schematic picture of the interaction of dust aerosols with different radiative components of the atmosphere, the direct radiative effect, is shown in Figure 2.2. Shortwave and longwave absorption by dust aerosols causes the heating of the dust layer. The combination of absorption and backscattering of shortwave radiation reduces the incoming solar radiation reaching the surface, and thereby decreases the heating rate of the atmosphere below the dust layer. In contrast, by trapping the outgoing longwave radiation, thermal radiative forcing of dust at the surface is always positive (*Haywood and Boucher*, 2000; *Hansell et al.*, 2010), suggesting that mineral dust warms the surface during night when it only interacts with longwave radiation. It should be noted that direct radiative forcing by dust aerosols is also dependent on the albedo of the underlying surface due to the interaction of mineral dust with reflected solar radiation (*Liao and Seinfeld*, 1998). For example, higher reflection of solar radiation by bright desert surfaces leads to a greater absorption of radiation by dust aerosols, thereby increasing the degree of atmospheric heating. Likewise,

absorbing dust aerosols above low-level clouds increase the atmospheric heating rate due to the high reflectivity of clouds (*Podgorny and Ramanathan*, 2001). Dependence of the direct radiative effect of dust to the albedo of the underlying surface was highlighted in the Saharan Mineral Dust Experiment (SAMUM-1) project, so that positive and negative net top of the atmosphere (TOA) radiative forcing for bright and dark surfaces was identified, respectively (*Heintzenberg*, 2009).

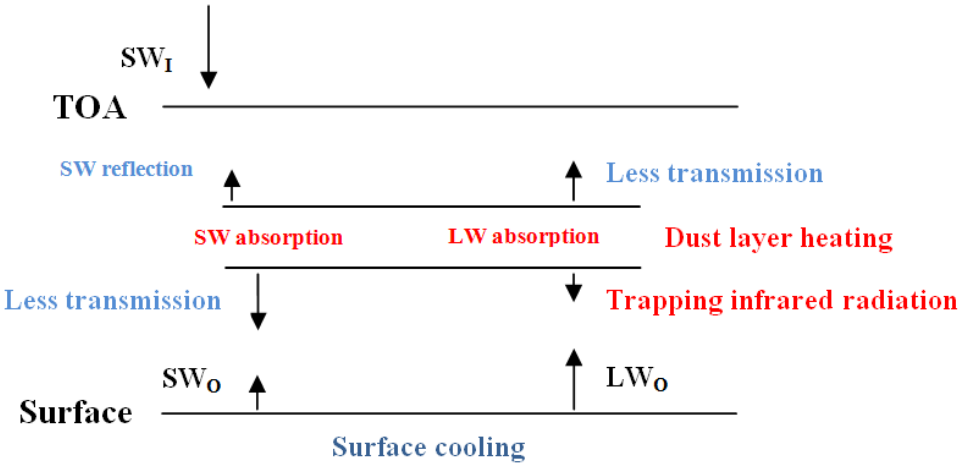

Figure 2.2. A schematic illustration of interaction of mineral dust with different radiative components of the atmosphere during daytime. Daytime surface cooling is caused by the fact that shortwave reflection dominates over longwave trapping by dust aerosols.

The term semi-direct effect was first used by *Hansen et al.* (1997) to describe the effects of the absorption of radiation by aerosols on clouds (*Ackerman et al.*, 2000). Dust aerosols embedded within clouds absorb radiation which leads to a reduction of relative humidity, enhancement of cloud evaporation (*Ackerman et al.*, 2000; *Koren et al.*, 2004; *Huang et al.*, 2006) (i.e. the cloud burning effect), and therefore a reduction in cloud cover. This suggests that there is a negative correlation between absorbing aerosols that are embedded within clouds and cloud development. Such negative correlation is more pronounced for larger dust aerosols as they are more absorptive. The reduced cloud cover is associated with warming of the ground surface, in contrast to the general daytime surface cooling effect of mineral dust aerosols. Note that the semi-direct effect of mineral dust is sensitive to the position of the dust layer relative to clouds. If the aerosol layer is located below cloud, heating within the dust layer can enhance convection and thus cloud cover. The

warming effect of absorbing dust aerosols above the cloud top, on the other hand, stabilizes the underlying layer, so that vertical development of clouds is inhibited, while their horizontal development may be increased (*Koch and Del Genio*, 2010).

Mineral dust particles are efficient ice nuclei (IN) and contribute to the formation of ice crystals in high clouds (*Targino et al.*, 2006; *Teller and Levin*, 2006), indicating the important role of dust particles in cold cloud processes. However, during their transport dust particles may have chemical interaction with trace gases and other aerosols (undergo aging), which modify their properties. Those dust particles that are coated with soluble materials (e.g. sea salt and anthropogenic pollutants) can become efficient cloud condensation nuclei (CCN) (*Levin et al.*, 2005; *Astitha et al.*, 2010). They can also act as CCN through water adsorption (*Karydis et al.*, 2011).

An increase in (dust) aerosol concentration leads to formation of a larger number of smaller cloud droplets for a constant liquid water content, thereby enhancing cloud reflectance by increasing total droplet cross-sectional area, the process known as the first indirect effect (because it is through modification of cloud radiative properties due to changes in CCN or IN) or the cloud albedo effect (*Twomey*, 1974, 1977; *Twomey et al.*, 1984). Indeed, it has been found that cloud droplets have smaller sizes in the Northern Hemisphere compared to the Southern Hemisphere, and this feature has been attributed to a higher atmospheric aerosol load in the Northern Hemisphere (*Breon and Colzy*, 2000). A reduction in cloud droplet size suppresses collision and coalescence processes (*Rosenfeld*, 1999), and hence precipitation formation (*Ferek et al.*, 2000; *Rosenfeld*, 2000), the so-called second indirect or "Albrecht" effect (*Albrecht*, 1989). This leads to an increase in cloud lifetime or cloud fraction, which increases its reflectivity over time (*Albrecht*, 1989). Suppressing precipitation (known as the warm-rain suppression effect) resulting in an increase of freezing processes in mixed-phase clouds, as well as greater latent heat release (*Tao et al.*, 2012), thereby leads to formation of large hail, higher cloud top heights and enhancement of cold-rain processes (*Andreae et al.*, 2004; *Rosenfeld and Woodley*, 2000), the process known as the aerosol invigoration effect (*Andreae et al.*, 2004; *Rosenfeld et al.*, 2008). Indeed, using the Integrated Community Limited Area Modeling Sys-

tem (ICLAMS), *Solomos et al.* (2011) have shown that adding hygroscopic dust particles can lead to enhanced convection and updrafts, a delay in the initiation and reduction of precipitation and consequently higher cloud top heights.

An increase in aerosol loading does not necessarily lead to an increase in cloud albedo as the reflectivity of clouds depends on several factors, including the optical depth of the cloud, the single scattering albedo of the droplets and the asymmetry parameter (*Tao et al.*, 2012). For example, for heavily polluted clouds with absorbing aerosols such as black carbon, the single scattering albedo of droplets and hence the reflectivity of clouds decreases. Reflectivity of clouds may also be decreased by giant aerosols as they form a smaller number of giant CCN, in contradiction to the first indirect or Twomey's effect. Rainfall suppression also does not necessarily occur with higher aerosol concentrations as rainfall formation is also a function of the size and absorbing nature of aerosols. For example, natural large sea salt particles that are acting as giant CCN can initiate and increase the warm-rain process (*Johnson*, 1982; *Cheng et al.*, 2007), a common feature that has long been used for artificial rain enhancement (*Tao et al.*, 2012). Aerosol microphysics is also an important factor that influences precipitation processes. For example, absorbing aerosols such as biomass smoke and mineral dust may invigorate convective clouds and increase precipitation (*Andreae et al.*, 2004; *Lin et al.*, 2006; *Koren et al.*, 2005).

2.2.2 Previous Estimates of the Direct Radiative Forcing by Dust

As discussed earlier, direct radiative forcing by mineral dust at the surface is negative due to reflection and absorption of shortwave radiation. The global annual net (shortwave + longwave) direct radiative forcing by dust aerosols at the surface was estimated to be about -1.64 W m^{-2} using the NASA GISS AGCM (National Aeronautics and Space Administration Goddard Institute for Space Studies Atmospheric General Circulation Model) (*Miller et al.*, 2004a). Quite similar results have been identified by *Miller and Tegen* (1998) with a net radiative forcing of -2.08 W m^{-2}, while *Woodward* (2001) and *Miller et al.* (2006) estimated substantially lower values of -0.82 W m^{-2} and -0.84 W m^{-2}, respectively. The net

negative direct radiative forcing at the surface is due to the fact that trapping of longwave radiation by mineral dust during daytime is less than the attenuation of visible radiation through a combination of absorption and reflection. Large uncertainties in current estimates of the direct radiative forcing by dust (*Dubovik et al.*, 2002; *Durant et al.*, 2009) are primarily due to uncertainties in global dust burden (*McGowan and Soderholm*, 2012) and optical properties of soil dust particles (*Dubovik et al.*, 2002), as well as the complex physical and chemical properties of dust particles and their complex interaction with radiation budget (*Sokolik et al.*, 2001).

Seasonal and annual estimates of direct radiative forcing by mineral dust aerosols and its comparison with the annual warming effect of greenhouse gases (GHGs) is presented in Figure 2.3. Direct radiative forcing by dust has a peak negative forcing during the Northern Hemisphere summer season. In contrast, low dust concentrations during autumn contributes to a substantial reduction of the net direct radiative forcing. The global annual net direct radiative climate forcing by mineral dust at the surface was estimated to be -1.8 W m^{-2} (*Miller et al.*, 2004b), compared to positive global annual forcing of 2.63 W m^{-2} by anthropogenic GHGs (*Hofmann et al.*, 2006).

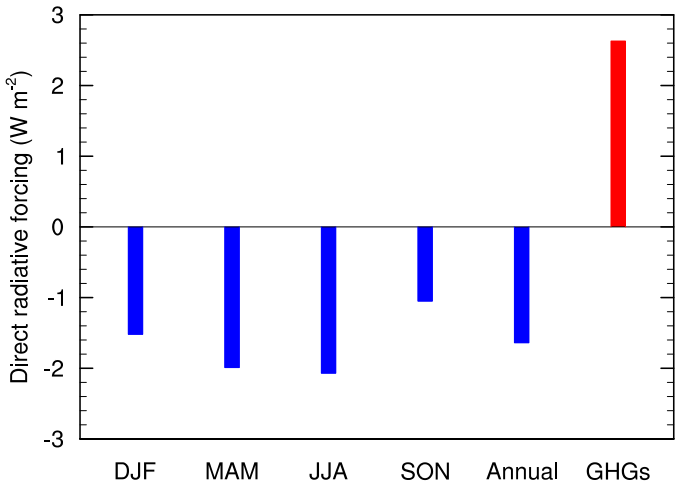

Figure 2.3. Globally averaged direct radiative forcing by mineral dust aerosols at the surface in different seasons and annually (blue) and its comparison with annually averaged radiative forcing by greenhouse gases (GHGs) (red) (data from: *Miller et al.* (2004a); *Hofmann et al.* (2006)).

2.2.3 Longwave Direct Radiative Forcing by Dust

Due to their large size and chemistry composition, mineral dust aerosols absorb and re-emit infrared radiation emitted by the Earth's surface, a feature that is similar to the GHGs warming effect. Empirically-based analysis has shown that infrared radiative forcing by mineral dust over desert surfaces under cloud-free conditions can reach up to 50 W m^{-2} (for July monthly average at 1200 UTC) (*Haywood et al.*, 2005). Nevertheless, the shortwave radiative cooling effect of dust has a larger contribution than its longwave warming effect, as highlighted by the net negative radiative forcing shown at the top of Figure 2.4. Note that values in Figure 2.4 are global annually averaged estimates, while radiative forcing at the regional scale over and immediately downwind of source regions of dust is more significant. For example, over North Africa *Yoshioka et al.* (2007) estimated -15.47 W m^{-2}, +14.74 W m^{-2} and -0.73 W m^{-2} values for annual shortwave, longwave and net direct radiative forcing by dust aerosols at the surface, respectively. The high contribution of infrared radiative forcing over North Africa, as well as over other source regions, is due to the presence of relatively large dust aerosols that have greater interaction with longwave radiation. Another contributing factor is that the thermal infrared radiative forcing occurs both during the day and night, while the interaction of dust aerosols with visible solar radiation is only present during the daytime.

There is some evidence suggesting that the longwave warming effect of dust at the surface is more significant during the night when surface temperature is lower (e.g. *Hansell et al.*, 2010). This was attributed to the fact that vertical mixing associated with the evolution of the daytime mixed layer transfers the surface longwave heating by dust to the whole boundary layer, while in the stable nocturnal boundary layer, the warming effect is mainly restricted to the near-surface layer and therefore is stronger (*Hansell et al.*, 2010). The positive nighttime direct radiative effect of dust aerosols suggests that dust has the potential to postpone nocturnal cooling. The longwave warming effect of dust particularly increases when large particles are more abundant due to their relatively high absorption within the infrared atmospheric window. Trapping of longwave radiation by dust aerosols

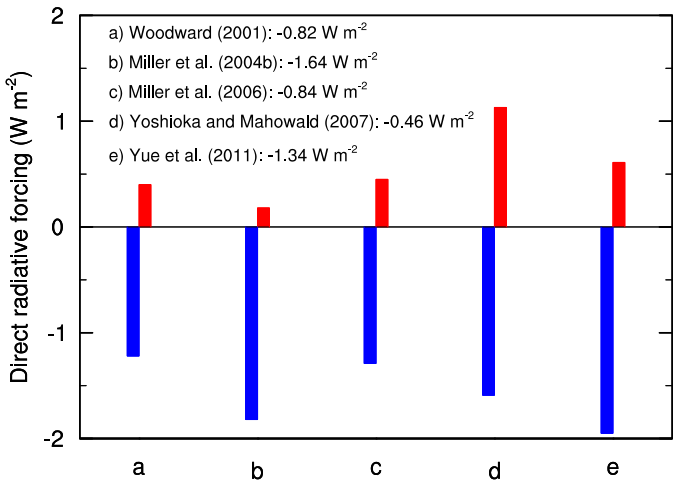

Figure 2.4. Global annually averaged shortwave (blue) and longwave (red) direct radiative forcing by dust aerosols at the surface obtained from previous work. The labels a) to e) relate to various previous studies listed at the top of the figure, along with the net (shortwave + longwave) radiative forcing derived in each study.

also induces cooling at upper levels (*Hansell et al.*, 2010). Therefore, the near-surface heating and upper level cooling contributes to destabilization of the boundary layer during night.

2.3 Dust Effects on Surface Energy Exchanges

As discussed earlier, the absorptive characteristic of dust aerosols is associated with dust layer heating. Heating of the dust layer aloft, combined with daytime surface cooling increases boundary layer stability, which reduces the intensity of convection and therefore partly prevents boundary layer development and atmospheric turbulent mixing (*Miller et al.*, 2004b). Since the atmosphere is in radiative equilibrium, surface cooling must be balanced by a reduction of upward thermal infrared radiation. The upward infrared radiation is related to surface sensible and latent heat fluxes, whose values depend upon surface temperature, as well as soil moisture availability for the latter (*Miller et al.*, 2004b). Over dry land surfaces where the main sources of atmospheric dust are located, surface latent heat flux is generally small, and hence surface cooling is balanced predominantly by decreased surface sensible heat flux to the atmosphere (*Miller et al.*, 2004b; *Mallet et al.*,

2009). In contrast, surface cooling is primarily balanced by the reduction of surface latent heat flux over the oceans.

Although direct radiative forcing by mineral dust is generally associated with the reduction of near-surface temperature, previous studies have shown that within regions of deep convection, surface temperatures are almost unchanged or only slightly perturbed (*Miller and Tegen*, 1998, 1999). For example, in spite of lower dust concentrations over the Arabian Sea in winter (as shown in Figures 2.1), surface cooling by mineral dust aerosols was found to be greater than summer (*Miller and Tegen*, 1998). This is caused by the fact that establishment of the ITCZ in the region during summer results in deep convection within the atmospheric boundary layer. Consequently, heat exchange from the dust layer to the surface in such a deep convective atmosphere can partially compensate for the surface cooling associated with the direct radiative effect of dust (*Miller and Tegen*, 1998).

Radiative impact of dust aerosols is also a function of dust layer height (*Zhu et al.*, 2007; *Forster et al.*, 2007). The low-level dust layer only marginally induces surface cooling, while a uniform distribution of dust aerosols and an elevated dust layer can cause more significant surface cooling, with the latter having the greatest impact (*Chung and Zhang*, 2004). For a low-level dust layer, vertical mixing and turbulent fluxes within the PBL partially offset the surface cooling by transferring the absorbed heat from the dust layer downward to the surface. In the elevated case, heating of the dust layer occurs well above the PBL where there is reduced vertical mixing and turbulent fluxes, and therefore there is little transfer of absorbed heat from the elevated dust layer to the surface (*Chung and Zhang*, 2004).

Chapter 3

Australian Dust Transport

Alizadeh Choobari, O., P. Zawar-Reza and A. Sturman (2012), Atmospheric forcing of the three-dimensional distribution of dust particles over Australia: A case study. *J. Geophys. Res., 117*, D11206, doi:10.1029/2012JD017748.

Abstract. Knowledge of atmospheric processes responsible for horizontal and vertical distribution of dust particles is important for identifying their transport pathways. The Weather Research and Forecasting with Chemistry (WRF/Chem) model, complemented by observations, was used to simulate and observe the three-dimensional distribution of Australian dust for a severe dust event during 22-23 September 2009. The passage of a cold front modified the boundary-layer structure during this event, allowing dust to be lifted and subsequently transported for a significant distance. The model simulated the maximum dust concentrations to be located behind the cold front as a result of strong post-frontal wind speeds. The boundary-layer depths were also shown to be significantly deeper behind the cold front where dust particles could be lifted to the top of the boundary layer by turbulent fluxes associated with strong mixing. However, dust was predicted to reach its maximum height ahead of the cold front as a result of lifting in the warm conveyor belt. Both Moderate Resolution Imaging Spectroradiometer (MODIS) data and the WRF/Chem model results for this event highlight two transport pathways of dust: southeastward to the Tasman Sea and northward towards tropical regions of Australia. The vertical distribution of dust from Cloud-Aerosol Lidar with Orthogonal Polarization (CALIOP) satellite data and cross-sectional analysis of the model results indicate that significant amounts of dust aerosols were transported over the Tasman Sea towards New Zealand within the lower atmosphere.

3.1 Introduction

As much of Australia is frequently under the influence of a subtropical high-pressure belt, subsiding air associated with this feature results in an arid or semi-arid climate over much of the interior region of the country. Associated with this arid climate, dust events often occur in the spring, but end in the early summer over northern regions of Australia when the monsoon season starts (*Goudie and Middelton*, 2006). In contrast, they continue over southern Australia until the end of March (*Shao*, 2008). Dust storms are often accompanied by strong winds associated with the passage of cold fronts (*McGowan et al.*, 2005) and the subsequent modification of the planetary boundary layer (PBL). Australian dust particles are frequently transported southeastward by pre-frontal northwesterly winds (*Knight et al.*, 1995; *McGowan et al.*, 2005) and can, on occasions, reach New Zealand (*Knight et al.*, 1995; *McTainsh et al.*, 2005) where they may degrade air quality. They may also be carried northwestward by southeasterly trade winds (*Shao*, 2008). In spite of this existing knowledge, further investigation is required to fully understand the atmospheric processes that affect long-range transport of Australian dust and the pathways that it follows.

The spatial distribution of dust over Australia has mostly been studied using such approaches as kinematic trajectory modelling (*McGowan et al.*, 2000), large-scale analysis of surface pressure charts (*McGowan et al.*, 2005; *McTainsh et al.*, 2005) and dispersion and trajectory models (*Knight et al.*, 1995; *McGowan et al.*, 2005). Although these approaches provide a broad scale view of the movement of dust across the region, they are unable to resolve the impact of boundary-layer characteristics and frontogenetically-forced vertical motion on the distribution of dust particles. In particular, trajectory approaches can only resolve the advection process and not the smaller scale convection and associated vertical mixing of dust particles present within the boundary layer. Numerical simulation of the 22-23 October 2002 dust event over Australia by *Shao et al.* (2007) identified potential dust sources, as well as the distribution of dust plumes under the action of a frontal system. However, knowledge is still limited of the vertical structure of

dust plumes near source regions and during transport, as well as the physical mechanisms responsible for the observed vertical distribution of dust. Indeed, the vertical structure of Australian dust events is poorly understood and is often estimated based on such factors as the height of the subsidence inversion (*McTainsh et al.*, 2005) or qualitative reports based on visual inspection of radar and radiosonde data from airports (*Leys et al.*, 2011). Given that dust plume height is a key factor for estimating continental dust loss (*Knight et al.*, 1995; *McTainsh et al.*, 2005) and the extent of dust transport (*Huang et al.*, 2006), as well as for assessment of dust radiative forcing (*Chung and Zhang*, 2004), more accurate estimates of the height of Australian dust plumes need to be determined. For example, the distance over which mineral dust is transported is very sensitive to dust layer elevation, as if the dust is able to enter the free atmosphere, it can be transported long distances. Furthermore, previous research suggests that an elevated dust layer has a larger impact on surface cooling than a low-level dust layer (e.g. *Chung and Zhang*, 2004), because heating of the dust layer associated with absorption of shortwave and thermal infrared radiation occurs well above the boundary layer, and is unlikely to be transferred to the surface. Elevated dust aerosols also have longer atmospheric lifetimes than low-level aerosols, so that their radiative impact is more long-lasting.

This chapter therefore aims to investigate the three-dimensional distribution of Australian dust during the 22-23 September 2009 dust storm by employing the Weather Research and Forecasting with Chemistry (WRF/Chem) regional model. In particular, this study attempts to identify the role of the major atmospheric mechanisms responsible for dust transport in frontal zones. These processes include those that are responsible for vertical distribution of dust plumes to the top of the boundary layer, horizontal transport of particles by divergent winds from high-pressure systems toward low-pressure regions, and rapid vertical transport of dust particles to the free atmosphere by the warm conveyor belt (*Sinclair et al.*, 2008) where strong ascending motions are present (*Eckhardt et al.*, 2004). Because of shortcomings in parameterization of the variety of complex physical mechanisms responsible for dust entrainment and its subsequent mixing within the boundary layer in pre- and post-frontal conditions, as well as errors that might be caused by sim-

ulation of sub-grid phenomenon, high resolution CALIOP (Cloud-Aerosol Lidar with Orthogonal Polarization) data sets have been used here to provide supporting information on the vertical structure of the dust plumes. The use of CALIOP data, in conjunction with WRF/Chem model results, should help to better understand the three-dimensional distribution of Australian dust.

This study therefore aims to address a number of key questions. First, what are the exit pathways of the dust event and can the WRF/Chem model effectively simulate the spatial distribution of dust during such events? To address this question, model results are analysed and compared with available satellite data sets, and ground-based measurements in Australia. Second, what atmospheric processes are responsible for the three-dimensional distribution of Australian dust during the passage of a cold front associated with an intense extratropical cyclone? This question cannot be addressed by using observations alone, so that numerical modelling represents a useful tool for extending knowledge of such processes. Finally, what is the vertical and horizontal extent of Australian dust plumes during transport? This question has been addressed using available satellite data in combination with model results.

This chapter is organized in the following way. Section 3.2 describes the model set up and satellite data set. Features of the dust event and its associated synoptic weather conditions are discussed in Section 3.3, along with the large-scale behaviour of the dust plume, while Section 3.4 presents a comparison of model results with satellite data and ground-based measurements. The impact of frontal systems on boundary-layer evolution and the vertical distribution of dust particles are the subject of Section 3.5. The vertical structure of the dust plumes shown by the CALIOP data set is discussed in Section 3.6, while a discussion and major conclusions are summarised in Section 3.7.

3.2 Numerical Model and Satellite Data

3.2.1 Numerical Model Description

The WRF/Chem model was set up with 230 × 170 horizontal grid points at 27 km horizontal grid spacing and 27 vertical layers with smaller increments in the lower part of the PBL, for a large domain covering Australia and New Zealand, thereby providing a large-scale synoptic view of weather systems affecting the region. The meteorological initial and boundary conditions come from the National Centers for Environmental Prediction (NCEP) Final Analysis (FNL) re-analysis data at 1 ° resolution (`http://www.nomad3.ncep.noaa.gov/ncep_data`), and the boundary conditions were updated every 6 hours, without data assimilation or analysis nudging. The model run was initialized at 0000 UTC on 20 September and continued until 0000 UTC on 26 September, 2009. Biomass burning sometimes occurs in the northern tropical regions of Australia, but its contribution to the aerosols mass is omitted here to focus only on dust transport.

3.2.1.1 Aerosol and Dust Parameterization Schemes

The aerosol parameterization is based on the Model for Simulating Aerosol Interactions and Chemistry (MOSAIC) (*Zaveri et al.*, 2008) with eight sectional bins for aerosols less than 10 μm (eight bins are for particles less than 2.5 μm ($PM_{2.5}$) and two bins for particles between 2.5 and 10 μm). Dry deposition includes turbulent and molecular diffusion, as well as gravitational settling which was configured in the simulation based on the approach of *Binkowski and Shankar* (1995). Wet deposition via in-cloud and below-cloud scavenging was also included in the simulation. In the in-cloud process, dust particles form condensation nuclei that are captured by water droplets that grow on them, while in the below-cloud process, raindrops scavenge dust particles as they fall.

The dust emission scheme is based on the dust transport (DUSTRAN) module developed by *Shaw et al.* (2008) which has been modified to adjust it to the 24-category USGS

land-use classes of WRF, which are different from the 59 land-use categories of the Olson database used in *Shaw et al.* (2008). Vertical dust flux from the surface was approximated by *Shaw et al.* (2008), as follows:

$$F = \alpha C u_*^4 \left(1 - \frac{f_w u_{*t}}{u_*}\right) \quad for \;\; u_* \geq u_{*t} \tag{3.1}$$

where α is the vegetation mask that ranges from zero to 1 and depends on vegetation cover, C (g cm^{-6} s^{-3}) = 1.0 $\times 10^{-14}$ is a dimensional empirical constant, u_{*t} (cm s^{-1}) is the threshold friction velocity below which there is no dust emission, considered here to be 20 cm s^{-1}, u_* (cm s^{-1}) is the friction velocity relating to the downward transfer of momentum flux to the surface ($u_* = \sqrt{\tau/\rho}$, where τ is shear stress at the surface and ρ is air density), and f_w is the soil wetness factor, which is estimated based on the approximation of *Fecan et al.* (1998):

$$f_w = \begin{cases} \sqrt{1 + A(w - w')^b} & w > w' \\ 1 & w \leq w' \end{cases} \tag{3.2}$$

where $\omega(\%)$ is the gravimetric soil moisture or ground wetness ($\frac{mass\ of\ water}{mass\ of\ soil} \times 100$) and obtained by converting model soil moisture ($\frac{m^3}{m^3}$) assuming a constant soil density of 2.6 g cm^{-3}:

$$w = \frac{soil\ moisture}{2.6} \times 100 \tag{3.3}$$

The coefficients A = 1.21 (indicating soil structure) and b = 0.68 (indicating moisture tension) were found by *Fecan et al.* (1998) on the basis of empirical data and ω' denotes the maximum amount of water that can be absorbed by the soil and is a function of soil clay content:

$$w' = 0.0014\beta_1^2 + 0.17\beta_1 \tag{3.4}$$

where β_1 is fraction of clay content in the soil as a percentage for 7 different Zobler soil

classes ($\beta_1 = \beta_{1,j} \times 100$, where j = 1, ... , 7 denotes the 7 Zobler classes, see Table 3.1). Since there are 16 soil classes in the WRF model which are different from the 7 Zobler soil categories used in *Shaw et al.* (2008), the WRF soil classes were mapped to Zobler soil categories as shown in Table 3.2. Note that the DUSTRAN module in the WRF/Chem model skips dust computations for WRF soil classes greater than 13, including organic material, water, bedrock and other types, such as land-ice. Based on Equation 3.4 and Table 3.1, ω' increases with the soil clay content, indicating that clay particles increase the adsorption capacity of soil. Equation 3.2 implies that when the soil moisture (ω) is smaller than the maximum amount of water that can be trapped by the soil (ω'), the wetness factor does not influence the erosion threshold, meaning that ω' corresponds to the minimum amount of soil moisture from which the threshold friction velocity increases (*Shaw et al.*, 2008).

Table 3.1. Fractions ($\beta_{k,j}$) of the soil texture categories in each Zobler soil class[a]

		$\beta_{k,j}$			
j	Zobler soil classes	Clay (k=1)	Small silt (k=2)	Large silt (k=3)	Sand (k=4)
1	Coarse	0.12	0.04	0.04	0.80
2	Medium	0.34	0.28	0.28	0.10
3	Fine	0.45	0.15	0.15	0.25
4	Coarse-medium	0.12	0.09	0.09	0.70
5	Coarse-fine	0.40	0.05	0.05	0.50
6	Medium-fine	0.34	0.18	0.18	0.30
7	Coarse-medium-fine	0.22	0.09	0.09	0.60

[a]After *Shaw et al.* (2008)

The initial background (unpolluted) dust concentrations at the start of the simulation are considered to be zero by the model and there is no lateral inflow of dust from outside of the domain, as the model assumes that all dust comes from the interior of the simulation domain, but dust can be freely advected out of the domain when it reaches the lateral boundaries. These assumptions mean that the model neglects the contribution of external sources and background aerosols. The model was initialized in the simulation at 0000 UTC on 20 September, which is at least two days before the cold front started to influence dust transport from local dust sources, while dust from outside the region is not considered of concern as Australia is located far from other source regions of dust, and therefore,

unlikely to be significantly affected by them.

3.2.1.2 Boundary-layer Parameterization Scheme

The main physics options used in the WRF/Chem simulation are listed in Table 3.3. The PBL scheme is particularly noteworthy as the vertical dust flux in Equation 3.1 is proportional to the shear stress via the friction velocity, which itself is strongly related to the turbulent fluxes within the boundary layer. Furthermore, boundary-layer structure plays a critical role in both the vertical distribution and amount of dry deposition of dust, as well as transport of dust away from the surface to the top of the boundary layer.

Table 3.2. WRF soil classes corresponding to the 7 Zobler soil categories

i	WRF soil classes	j	Zobler soil classes
1	Sand	1	Coarse
2	Loamy sand	1	Coarse
4	Silt loam	2	Medium
5	Silt	2	Medium
6	Loam	2	Medium
8	Silty clay loam	2	Medium
11	Silty clay	2	Medium
12	Clay	3	Fine
3	Sandy loam	4	Coarse-medium
10	Sandy clay	5	Coarse-fine
9	Clay loam	6	Medium-fine
7	Sandy clay loam	7	Coarse-medium-fine

Table 3.3. WRF/Chem model configuration[a]

Physical process	WRF/Chem option
Microphysics	Lin (*Lin et al.*, 1983)
Short-wave radiation	Goddard (*Wild et al.*, 2000)
Long-wave radiation	RRTM (*Wild et al.*, 2000)
Surface layer	Monin-Obukhov (*Obukhov*, 1971)
Land-surface model	NOAH (*Chen and Dudhia*, 2001; *Ek et al.*, 2003)
Boundary-layer scheme	YSU (*Hong et al.*, 2006; *Hong*, 2010)
Cumulus parameterization	Grell 3D (*Grell*, 1993)
Aerosol module	MOSAIC 8-bin (*Zaveri et al.*, 2008)
Dust scheme	DUSTRAN (*Shaw et al.*, 2008)

[a] Adapted from *Chapman et al.* (2009)

The PBL parameterization implemented in the WRF is based on the Yonsei University

(YSU) scheme (*Hong et al.*, 2006; *Hong*, 2010). The YSU scheme is a nonlocal closure model, which incorporates the contribution of large-scale eddies to the total flux. The nonlocal scheme includes a counter-gradient flux term, enabling realistic simulation of a well-mixed layer (*Hong et al.*, 2006; *Hong*, 2010). The boundary-layer top is defined as the height at which a critical bulk Richardson number ($Ri_{b,cr}$) reaches a constant value of 0.25 over land, but over ocean it is derived from (*Hong*, 2010):

$$Ri_{b,cr} = 0.16\ (10^{-7}Ro)^{-0.18} \tag{3.5}$$

where Rossby number (Ro) is defined as (*Hong*, 2010):

$$Ro = \frac{U_{10}}{f_0 z_0} \tag{3.6}$$

where U_{10} is the wind speed at 10 metres, f_0 the Coriolis parameter, and z_0 the surface roughness length. This method takes into account both buoyancy and mechanical mixing, thereby representing a realistic atmospheric boundary layer.

3.2.2 Satellite Data Description

Moderate Resolution Imaging Spectroradiometer (MODIS) instruments were launched on board NASA's Terra and Aqua satellites in 1999 and 2002, respectively, providing continuous multichannel measurements over ocean and land surfaces, allowing retrieval of aerosol optical properties. The retrieved aerosol optical depth (AOD) values are estimated to be reasonably accurate over the oceans, while accuracy decreases over land surfaces, and aerosol retrievals are limited over highly reflective land surfaces (*Remer et al.*, 2005).

A polarization-sensitive backscatter lidar known as CALIOP was launched on board NASA's Cloud-Aerosol Lidar and Infrared Pathfinder Satellite Observations (CALIPSO) satellite on 28 April 2006 (*Winker et al.*, 2007). Since then, CALIOP has provided nearly

continuous vertical profiles of aerosols and clouds globally, offering a unique opportunity to study vertical structure and transport of dust, as well as its optical properties. Nevertheless, CALIOP is unable to detect accurate aerosol profiles under thick aerosol and cloudy conditions, and when the quantity of aerosols is below its detection threshold.

CALIOP operates at 532 nm and 1064 nm. The Level 1B and Level 2 CALIOP data sets have been used in this study. The Level 1B (version 3.01) provides vertical profiles of the total attenuated backscatter coefficient at 532 nm (with horizontal and vertical resolutions of 333 m and 30 m, respectively) and 1064 nm (with horizontal and vertical resolutions of 333 m and 60 m, respectively) and the attenuated depolarization ratio at 532 nm. The depolarization ratio is the ratio of perpendicular to parallel components of received lidar signals at 532 nm, and is large for dust particles due to their non-sphericity (*Huang et al.*, 2009), so that they can be easily distinguished from other aerosols. Aerosol extinction coefficient profiles were derived from the Lidar Level 2 CALIOP data (with horizontal and vertical resolutions of 5 km and 300 m, respectively) during CALIOP flights over the Australian continent. Cloud-aerosol discrimination (CAD), an indicator used to discriminate between cloud (positive CAD) and aerosols (negative CAD), is used to exclude extinction caused by clouds.

3.3 The 22-23 September Dust Episode

3.3.1 Dust Event Features

The severe dust event during 22-23 September 2009 over Australia was associated with a cold front that produced limited precipitation and strong wind speeds. Prior to this intensive dust event, there was a severe drought over large parts of Australia for several years (*Zhao and Running*, 2010), combined with a record of very high maximum temperatures in 2009 (*Trewin and Vermont*, 2010), that contributed to an extreme soil moisture deficit and reduced vegetation cover. Correlation between Australian drought periods and the El Niño Southern Oscillation (ENSO) phenomenon has been found from records in

the past (*McTainsh et al.*, 2005). As a result of such extreme meteorology and drought conditions, the dust storm was one of the severest dust events since 1940, with the maximum hourly-averaged PM_{10} concentrations exceeding 15,000 μg m^{-3} at Bathurst (15,388 μg m^{-3}) and Bringelly (15,366 μg m^{-3}) air quality monitoring sites in New South Wales (*Leys et al.*, 2011). The network of ground-based measurement sites captured southeastward transport of Australian dust reaching Auckland, which is ~3600 km from the Lake Eyre Basin, Australia's most active dust source, producing PM_{10} concentrations reaching ~350 μg m^{-3}. These ground-based measurements indicate that dust transport from Brisbane on the east coast of Australia to the North Island of New Zealand (a ~2270 km distance) took approximately 1 day and 9 hours. The major dust emission sources in the region for this event have been determined to be Lake Eyre Basin (S1) in central southern Australia, the Channel Country (S2) in western Queensland, grazing land in northwestern New South Wales (S3), and mining areas near Cobar (S4) and Broken Hill (S5) (*Leys et al.*, 2011). Figure 3.1 shows the location of these major dust sources, as well as the Australian territories and surrounding seas mentioned in the text.

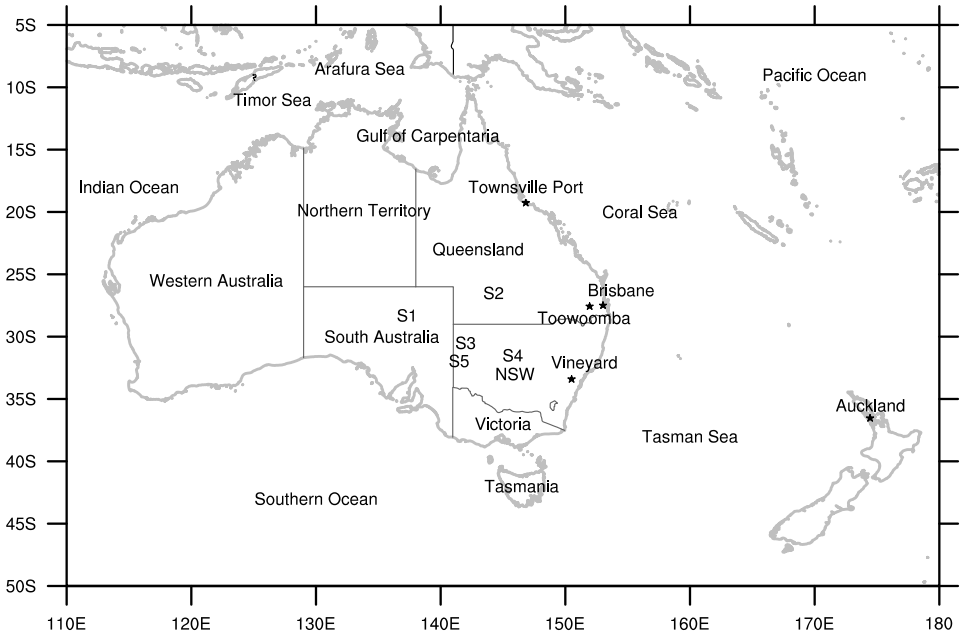

Figure 3.1. Position of Australian states and surrounding oceans and seas, the location of the main potential sources of dust: Lake Eyre Basin (S1), the Channel Country (S2), grazing lands in the northwest of New South Wales (NSW, S3), mining areas near Cobar (S4) and Broken Hill (S5), and places mentioned in the text.

3.3.2 *Synoptic Conditions during the Dust Storm and Large-scale Behaviour of the Dust Plume*

A strong mid-latitude cyclone (the minimum pressure that the cyclone achieved was simulated to be 974 hPa at 1700 UTC on 23 September 2009, see Figure 3.2c) crossed the Southern Ocean to the southeast of Australia (Figure 3.2a), and gradually intensifying over the next 24 hours as it moved further east (Figures 3.2b and 3.2c). By 0300 UTC on 24 September, the cyclone moved over the eastern Tasman Sea, while Australia was completely dominated by a high-pressure system (Figure 3.2d).

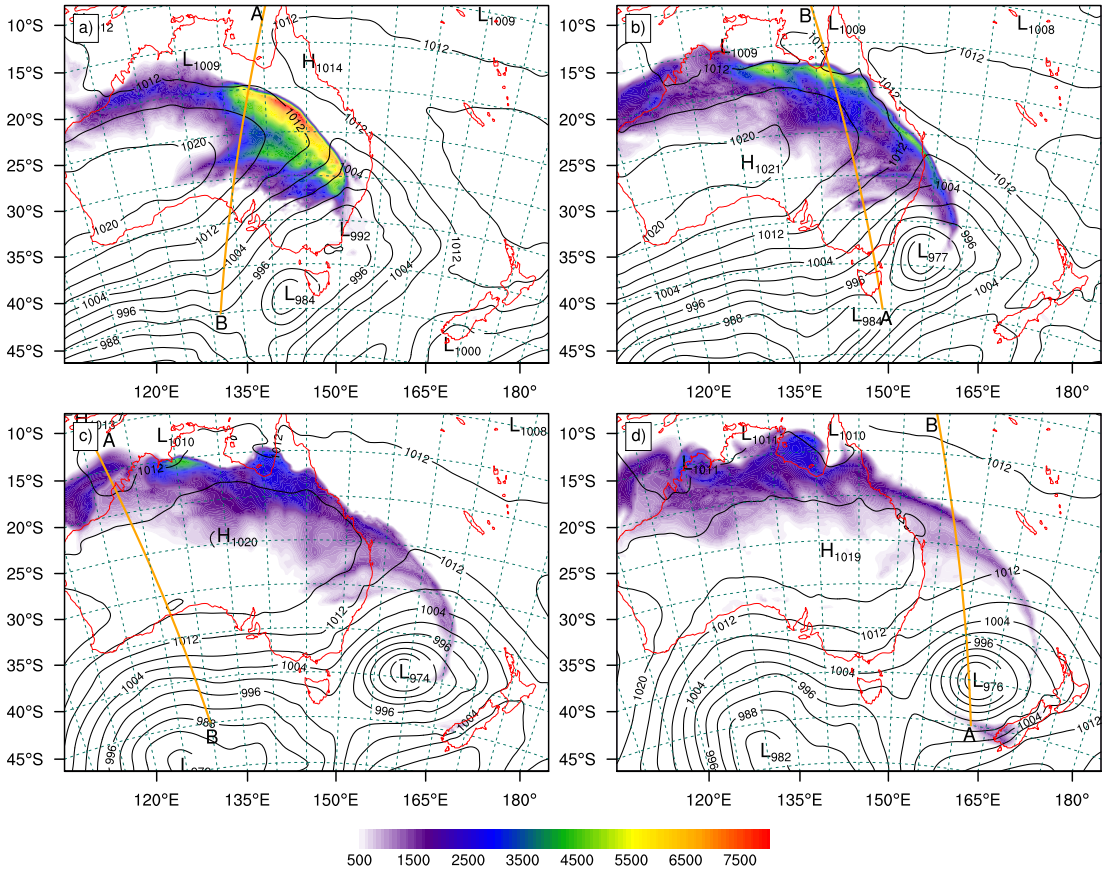

Figure 3.2. Simulated mean sea level pressure (contour interval of 4 hPa) and surface PM_{10} concentrations (μg m^{-3}, as shown in scale) over Australia at a) 1600 UTC on 22 September, b) 0400 UTC on 23 September, c) 1700 UTC on 23 September, and d) 0300 UTC on 24 September 2009. The orange lines labelled A and B show the CALIPSO orbit paths and their vertical cross-sections are plotted in Figures 3.12 and 3.13.

Figure 3.2a suggests that dust particles were initially entrained by strong cold post-frontal

southwesterly winds associated with the deep cyclonic system. The model simulated significant dust concentrations as a result of strong near-surface wind speeds that can be identified by tightly packed isobars. Dust particles were initially transported to northeastern Australia by these post-frontal southwesterly winds (Figures 3.2b and 3.2c), and to the Tasman Sea by pre-frontal northwesterly winds (Figures 3.2b, 2c and 2d). Model results also highlight transport of dust that was oriented from eastern central Australia to the northern tropical regions, and later to northwestern Australia under the influence of the anticyclonic circulation, with dust finally being advected to the Indian Ocean. By 0300 UTC on 24 September, part of the dust plume was predicted to have moved southeastward to the eastern Tasman Sea (Figure 3.2d), creating an arc shape to the dust clouds.

The long distance transport to the southeast appears to be due to the dominance of westerlies at higher altitudes both over the mid-latitudes and tropical regions (see Figure 3.3b). Also, strong fronts are typically associated with strong frontal jets that run parallel to the temperature gradient, strengthening northwesterly flows. This long-range southeastward transport is evident in the high PM_{10} concentrations observed at Auckland, New Zealand, as discussed earlier. The small amounts of dust predicted to occur only over the Tasman Sea at the 500 hPa level (Figure 3.3b), confirm that in the mid-troposphere, dust was only transported southeastward. Furthermore, the simulated PM_{10} concentrations at 700 hPa and 500 hPa (Figure 3.3) suggests that some of the dust particles over the Tasman Sea were transported in the opposite direction to the movement of the cyclonic weather system, reflecting the cyclonic turning within the warm conveyor belt. This rearward motion is also reflected in the potential temperature contours around the cyclonic circulation in Figure 3.3. It seems that dust was located within the warm conveyor belt and hence the transport pathway appears to be determined by the rising motion that occurs within this feature. As the dust seems to have been initially lifted from the surface into the atmosphere behind the cold front by strong winds, it appears that dust was transported through the frontal zone before being advected by the warm conveyor belt.

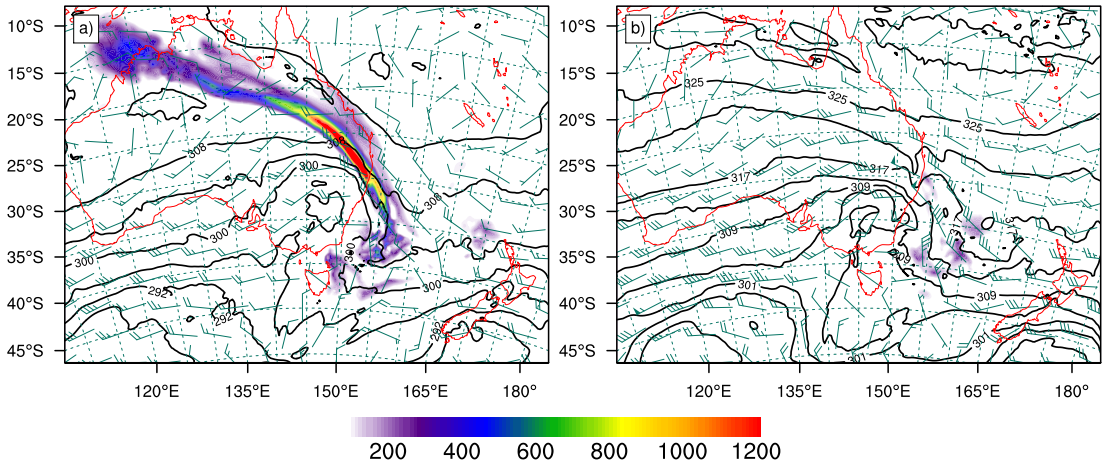

Figure 3.3. Simulated potential temperatures (contour interval of 4 K), horizontal wind speed (m s^{-1}) and PM_{10} concentrations (μg m^{-3}, as shown in scale) over Australia at 0000 UTC on 23 September at a) 700 hPa, and b) 500 hPa. In the wind vector scale, one full barb represents 10 m s^{-1}, with a soild triangle representing 50 m s^{-1}.

3.4 Comparison with Satellite and Ground-based Measurements

3.4.1 Satellite Data

Aerosol optical depth, attenuation of solar radiation by atmospheric aerosols, at 0.55 μm over both ocean and land at around 0100 UTC on 23 September and 0000 UTC on 24 September 2009 were obtained from the MODIS data set and simulated by the WRF/Chem model (Figure 3.4). Figure 3.5 also reveals eight-day (22-29 September 2009) AOD values at 0.55 μm retrieved from the MODIS data set. White regions in the MODIS image denote areas with no satellite measurements, either because of high surface albedo over bright surfaces or thick cloud cover. As the single-view sensors of the MODIS instrumentation are not able to differentiate between the visible solar radiation reflected by atmospheric aerosols from that reflected by the bright ground surfaces (note that most of the Australian land surface is covered by deserts), comparison of the model results and the MODIS data set is not reliable over land surfaces and only really possible over ocean. It should be noted that biomass burning is visible in satellite data (not shown) in the Queensland region (around 25°S and 147°E) on 24 September. These fires make it difficult to distinguish between the retrieved AOD from MODIS (Figures 3.4b and 3.5)

originating from mineral dust aerosols and smoke from biomass burning.

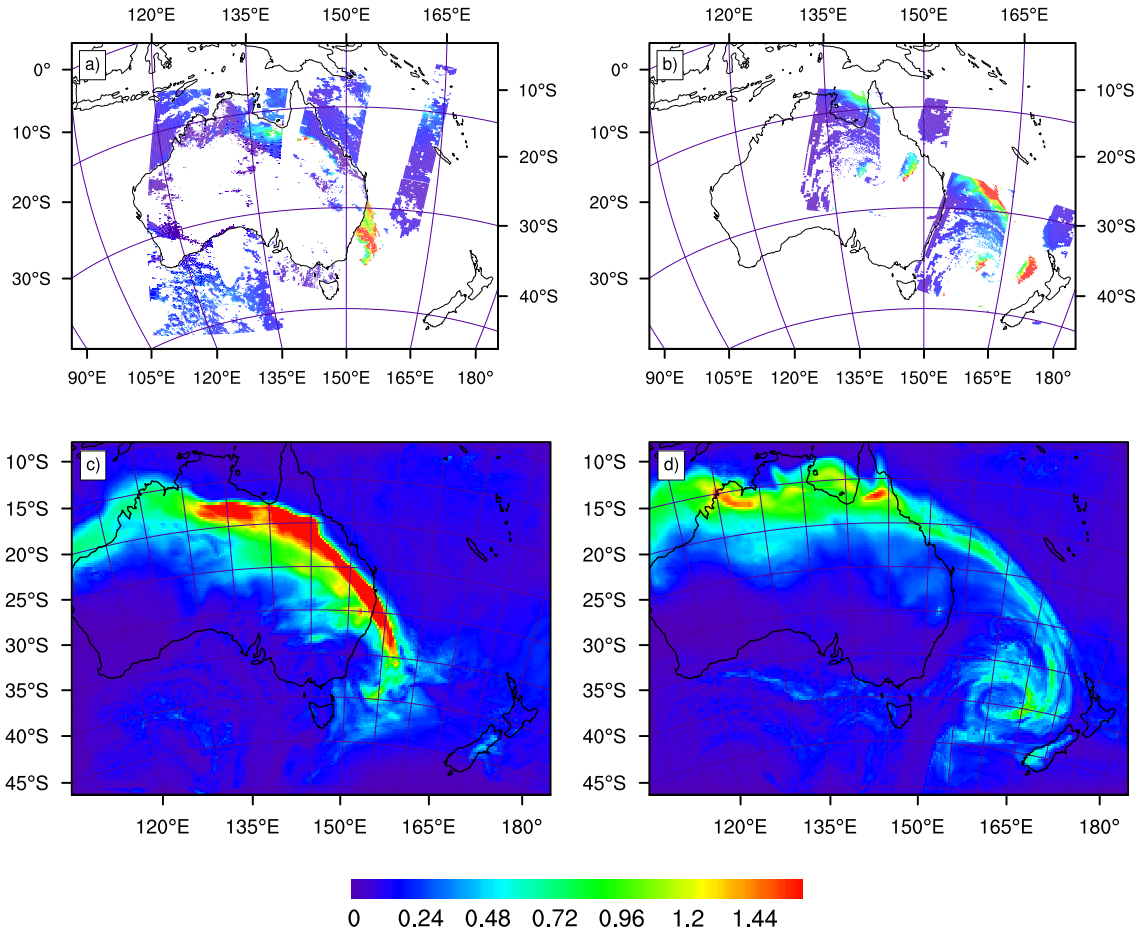

Figure 3.4. Comparison of aerosol optical depth (AOD) at 0.55 μm derived from MODIS on board the Terra satellite (top panel) and simulated by the WRF/Chem model (bottom panel) at around a), c) 0100 UTC on 23 September, and b), d) 0000 UTC on 24 September 2009.

Model simulations indicate that high AOD values extended from the Tasman Sea, offshore of the Australian east coast, to northeastern and northern Australia on 23 September (Figure 3.4c), showing some similarity to the MODIS measurements over the Tasman Sea (Figure 3.4a). Therefore, the modelled dust plume is approximately in the right location, although the model simulation overestimated aerosol concentrations extending from the northwest coast of Australia to the Indian Ocean (where the MODIS data set shows comparatively small amounts). As discussed earlier, the anticyclonic circulation (shown in Figure 3.2) was responsible for transport of dust across northern Australia towards the

Indian Ocean. High AOD values can be observed over the eastern part of the Tasman Sea, close to New Zealand at 0400 UTC on 24 September (Figure 3.4b). This pattern is quite well represented by the WRF/Chem model in Figure 3.4d, but with lower values. Overall, both simulation results and MODIS data indicate southeastward transport of dust to the Tasman Sea by the eastward propagating frontal system and to northern Australia by post-frontal southerly winds.

The eight-day AOD values obtained from MODIS indicate high AOD values off the south-east coast of Australia over the Tasman Sea (Figure 3.5), quite similar to the simulated AOD at 0100 UTC on 23 September (Figure 3.4c). It is highly likely that the aerosol plume would have extended over the Australian land area as well, because the aerosols mainly originated from the Australian deserts, but the MODIS instrumentation was not able to detect it adequately over the land area (for the reasons mentioned earlier). MODIS data also reveal moderate to high AOD values extending from the Coral Sea off the north-east coast of Australia towards the Gulf of the Carpentaria and the Arafura Sea to the north of the country, as well as to the Timor Sea to the northwest. Notice that the coastline of north and northeastern Australia is coincident with a sharp gradient in aerosol concentrations in Figure 3.5, except for northern Queensland, which strongly supports the argument that MODIS instrumentation was not able to accurately detect the aerosol concentrations over land, due to variations in surface albedo. As the source of dust is located on the Australian continent, it is safe to conclude that in reality significantly higher AOD values extended over northeastern Australian land toward the north and northwest, as shown in the model results in Figure 3.4c. The concentrations of aerosols simulated by the model and observed in the eight-day MODIS data set over the Southern Ocean, off Australia's south coast, are likely caused by sea salt due to increased wind speed associated with the low-pressure system moving across the Southern Ocean.

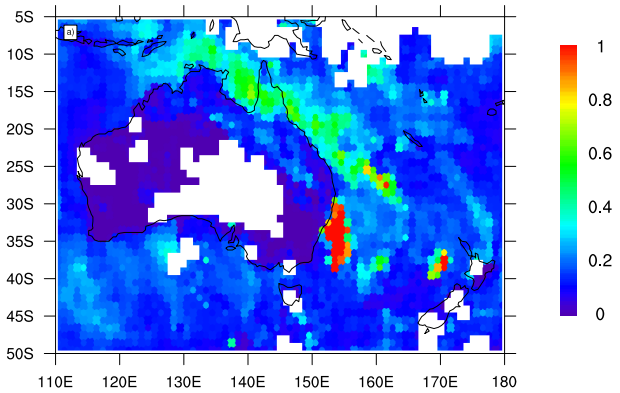

Figure 3.5. Eight-day aerosol optical depth (AOD) at 0.55 μm from 22-29 September 2009 retrieved from the MODIS data set.

3.4.2 In Situ Measurements

Ground-based hourly-averaged PM_{10} measurements obtained from air quality stations along the east coast of Australia (sites shown in Figure 3.1) and their comparison with simulated values are displayed in Figure 3.6. It should be noted that model values are representative of 27 $\times$ 27 km grid cells, while observations are point measurements. A comparison of the maximum simulated and observed PM_{10} concentrations and the time of their occurrence for these stations are shown in Table 3.4. The observed and simulated peak PM_{10} concentrations at Toowoomba occurred about 2 hours before the peak values at Brisbane to the east, indicating the eastward propagation of the dust plume. Furthermore, observed peak PM_{10} values decreased from south (Vineyard) to north (Townsville Port), due to the greater distance from major dust source regions as one moves to the north (*Leys et al.*, 2011).

Table 3.4. Maximum PM_{10} concentrations (μg m^{-3}) and the time of their occurrence observed and simulated by the WRF/Chem model during the 22-23 September 2009 dust event

		PM_{10} (μg m^{-3})		Time (UTC)	
Station	Location	Observed	Simulated	Observed	Simulated
Townsville Port	19.25°S, 146.83°E	1073	2076	23 Sep 1600	23 Sep 1600
Brisbane CBD	27.48°S, 153.03°E	6459	4703	23 Sep 0300	23 Sep 0100
Toowoomba	27.55°S, 151.95°E	6834	4858	23 Sep 0100	22 Sep 2300
Vineyard	33.39°S, 150.50°E	11174	1876	22 Sep 2000	22 Sep 1800

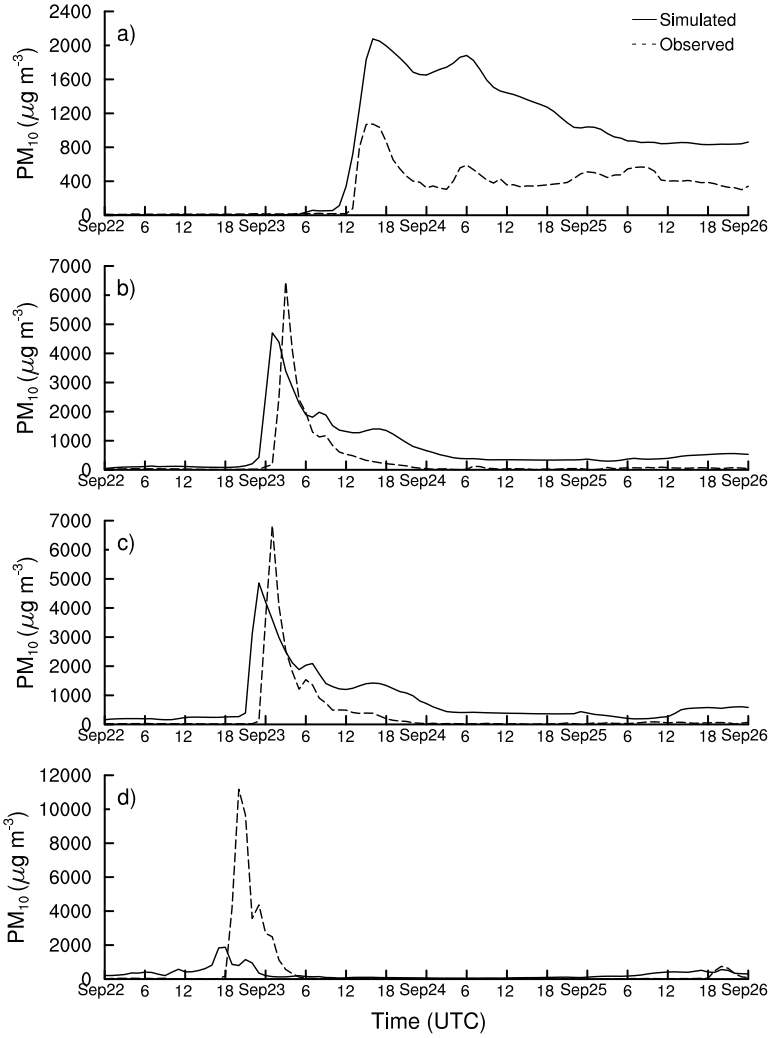

Figure 3.6. Hourly averaged PM_{10} concentrations (μg m^{-3}) measured (dashed line) and simulated (solid line) at four Australian air quality monitoring sites: a) Townsville Port (19.25°S, 146.83°E) in central Queensland, b) Brisbane CBD (27.48°S, 153.03°E), c) Toowoomba (27.55°S, 151.95°E), both in south Queensland, and d) Vineyard (33.39°S, 150.50°E) in New South Wales, Australia during 22-26 September 2009. Note the different Y axis scales in all panels. Locations of the air quality monitoring sites are shown in Figure 3.1.

For Brisbane and Toowoomba, the simulated PM_{10} concentrations followed the observations very well, and there is good agreement between the observed and simulated peak values, although the peaks were simulated 2 hours prior to the measurements and are less than observed values. Before and after the time of peak values when near-surface wind speeds were generally weaker, the simulated PM_{10} concentrations exceeded those observed. This bias arises because the threshold friction velocity is considered to be independent of particle size, having the constant value of 20 cm s^{-1}, causing the tendency

to overestimate dust emission at weaker wind speeds, as the stronger cohesive bonds between fine silt and clay particles are not considered. The similar pattern of PM_{10} concentrations observed and simulated at Brisbane and Toowoomba indicates that dust was being transported through the region rather than being entrained within it, otherwise local dust emission would have modified dust plume characteristics between sites, resulting in large variations in dust concentration over short distances (*Leys et al.*, 2011).

For Townsville Port, the model correctly simulated the time of dust arrival and temporal evolution, but overpredicted the PM_{10} concentrations by a factor of 2. PM_{10} concentrations stayed high for a long time compared to other stations, suggesting that the site is located downwind of a source that continued to supply dust for an extended period of time (*Leys et al.*, 2011). For Vineyard, the observed peak value exceeded the simulated peak value substantially. The underestimation of PM_{10} concentrations can be related to the underestimation of dust emission over source regions in New South Wales (S3, S4 and S5, shown in Figure 3.1). These areas could have acted as potential sources of dust, as prior to the dust event, there was a severe drought over the region.

3.5 Atmospheric Forcing of the Distribution of the Dust Plume

3.5.1 Boundary-layer Evolution during the Episode

Figure 3.7a clearly predicts considerable development of deep boundary-layer depths behind the cold front, driven by conditional instability close to the surface due to strong cold advection. Cold southwesterly air crossing the Southern Ocean onto the Australian land mass would have experienced significant heating as it moved across the surface that was still warm from the previous day, leading to deep boundary-layer development and subsequent vertical mixing. Bearing in mind that Figure 3.7a shows the situation at 0400 Eastern Standard Time (UTC + 10), synoptic-scale forcing would have been largely responsible for the evolution of the boundary layer rather than daytime heating. Similar development of a deep boundary layer behind a cold front caused by strong cold advec-

tion over the Atlantic Ocean was also evident in simulations performed by *Sinclair et al.* (2010). In contrast, warm advection in the warm sector of the cyclone (to the north-east of the low-pressure center) was associated with negative buoyancy, which reduced buoyancy-driven turbulent mixing, preventing the boundary layer from becoming well-mixed. As a result, there are notably shallower boundary-layer depths in this area due to a more stable boundary layer. It should be noted that even during warm air advection, shear-driven turbulence can cause the boundary-layer structure to evolve and reach moderate depths.

Figure 3.8a depicts a vertical cross-section perpendicular to the cold front along the line A to B in Figure 3.7a, showing potential temperature contours, boundary-layer depth, PM_{10} concentration and vertical velocity. The boundary-layer development behind the cold front can be related to enhanced vertical mixing, which increases near-surface wind speeds, leading to an increase of wind erosion and thus dust entrainment. Turbulent eddies associated with this well-mixed boundary layer are expected to have carried dust particles to the top of the boundary layer, and subsequent entrainment into the free atmosphere (as shown in Figure 3.8a). The reason that dust particles are predicted to have escaped from the boundary layer behind the cold front is partly due to the fact that the YSU PBL scheme defines the boundary-layer top as the level at which still minimum turbulent mixing occurs (*Hong*, 2010). Despite weak, or even a lack of, upward vertical motion behind the cold front (Figure 3.8a), the predicted vertical transport of particles through the depth of the boundary layer and to the lower layers of the free atmosphere indicates the importance of turbulent mixing for the vertical distribution of dust plumes. Note that the potential temperature contours slope backwards behind the cold front, demonstrating rearward tilting of the cold front with height.

There is a sharp decrease in boundary-layer depth from behind to ahead of the cold front (Figures 3.7a and 3.8a). However, ahead of the surface cold front, dust plumes are predicted to extend to a greater depth, reaching to approximately 8 km as a result of ascending motion in the warm conveyor belt (Figure 3.8a), demonstrating the contribution of dust to background tropospheric aerosols over the Australian region. The ascending motion

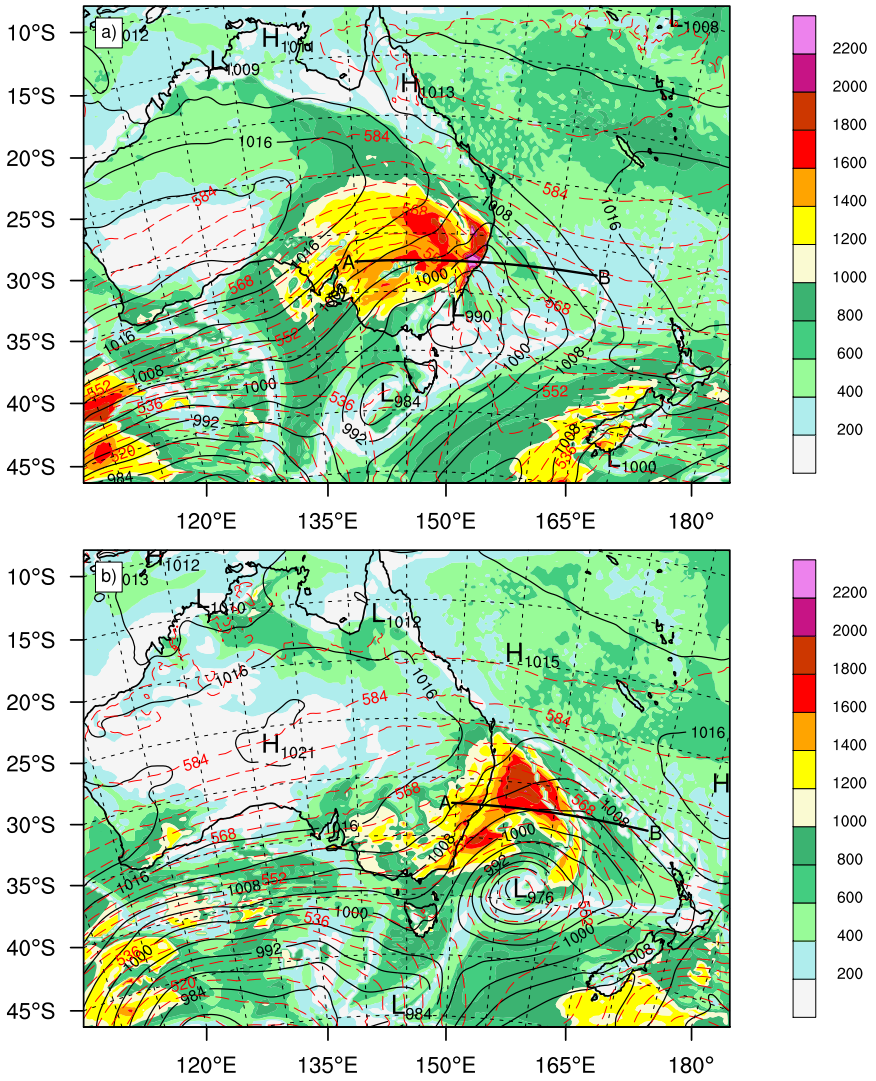

Figure 3.7. PBL depth (m, as shown in scale), mean sea level pressure (solid black contours with an interval of 4 hPa) and geopotential height contours at 500 hPa (dashed red contours with an interval of 4 dm) simulated by the WRF/Chem model at a) 1800 UTC on 22 September, and b) 1200 UTC on 23 September 2009. The bold black lines from A to B mark the vertical cross-sections plotted in Figure 3.8.

in the warm conveyor belt is evident in the strong positive vertical velocities at the leading edge of the cold front, demonstrating frontogenetically-induced vertical motions. The positive vertical velocities in the warm sector are consistent with the quasigeostrophic omega equation which indicates that warm advection is accompanied by rising motion when temperature and horizontal wind fields are sinusoidal (*Bluestein*, 1992).

Further west of the cold front, over the Australian continent, descending motion associated with the establishment of the anticyclonic circulation appears to be responsible for

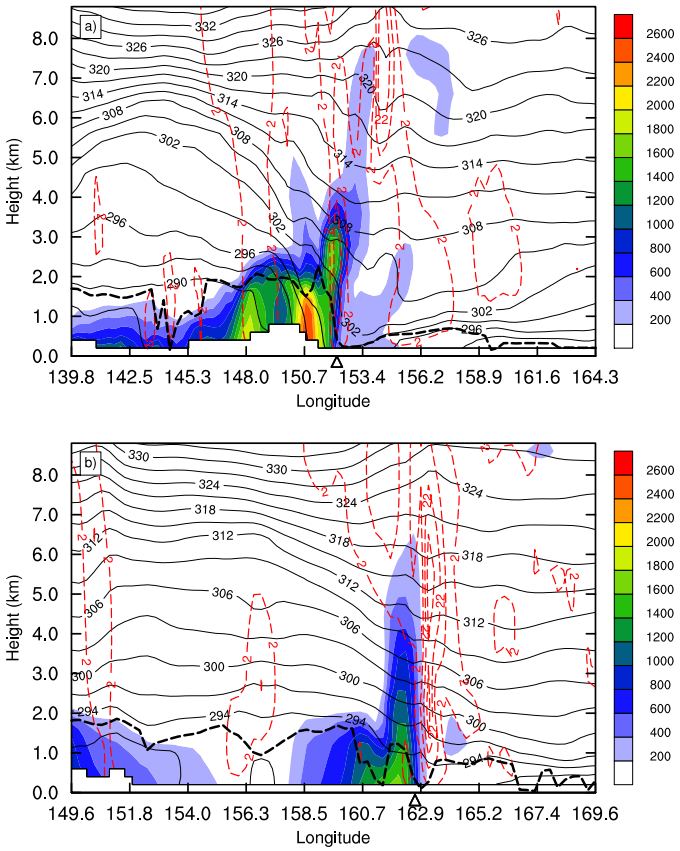

Figure 3.8. Simulation of vertical cross-sections of potential temperature (solid lines with a contour interval of 3 K), PM_{10} concentrations (μg m^{-3}, as shown in scale), vertical velocity (dashed red lines with contour interval of 10 cm s^{-1}) and PBL depth (dashed black line, km) perpendicular to the cold front along the line from A to B shown in Figure 3.7 at a) 1800 UTC on 22 September, and b) 1200 UTC on 23 September 2009. The approximate location of the cold front is shown by the arrow on the X axis. For clarity, only positive vertical velocities greater than 2 cm s^{-1} have been plotted, and it should be noted that Figures 3.8a and 3.8b cover different horizontal distances.

strong capping of the vertical extent of dust (Figure 3.8a). Consequently, the dust plumes are shown to be restricted to the lower atmosphere (below ~1.2 km), which can contribute to the increase of dry deposition. Furthermore, large-scale descending motion over the region associated with anticyclonic circulation contributes to divergent wind flows toward surrounding low-pressure regions. This motion is a key mechanism to advect particles horizontally to the warm conveyor belt region where there is a greater potential for the particles to be transported vertically to the free atmosphere (*Sinclair et al.*, 2008). This suggests that warm conveyor belt ascent is the main process acting to transport particles to the free atmosphere (*Kowol-Santen et al.*, 2001; *Sinclair et al.*, 2008), so that they can be subsequently transported over long distances by strong upper-level wind flows. Turbu-

lent mixing behind the cold front is also an important mechanism in the vertical transport of particles to the free atmosphere as it pushes particles to the altitudes where divergent motions from anticyclonic toward cyclonic circulation are stronger (*Sinclair et al.*, 2008). Even with the strong ascending motions ahead of the cold front, PM_{10} concentrations remained high near the surface, demonstrating the supply of dust particles through horizontal motions. This is also partly due to the fact that dust is mainly composed of coarse particles and its vertical transport is restricted by gravitational settling.

The predicted impact of the frontal system on the nighttime evolution of the marine boundary layer at 1200 UTC on 23 September 2009 is shown in Figure 3.7b. The boundary layer is deep behind the cold front extending from the central Tasman Sea to the coastal regions of southeastern Australia. Relatively shallow boundary-layer depths can be seen in the warm sector ahead of the cold front due to warm advection over colder surfaces. However, the lowest boundary-layer depths are located over central and western Australia where they are dominated by a high-pressure system with a central pressure of 1021 hPa.

A vertical cross-section perpendicular to the cold front, along the line AB in Figure 3.7b, shows that the plume of dust was advected up to around 6 km both behind and along the leading edge of the cold front (Figure 3.8b). The elevated PM_{10} concentrations are located to the west of the strong ascent in Figure 3.8b, while Figure 3.8a shows the high PM_{10} concentrations to be co-located with the strong frontal ascent. One possible cause for the difference is that the strong ascent would have been associated with high concentrations of dust when the frontal zone was moving over the source regions of dust and nearby areas, but as it moved away from the source regions to the Tasman Sea the rising air would have been increasingly dust-free, leaving the residual dust in the air lagging behind the front. Note that the PM_{10} concentrations are significantly reduced from a maximum concentration of $\sim$2600 μg m^{-3} in Figure 3.8a to $\sim$1600 μg m^{-3} in Figure 3.8b, demonstrating substantial dust loss during the transport from eastern Australia to the Tasman Sea.

Surface and mid-troposphere analysis of the low-pressure system located over the eastern

side of the Tasman Sea and close to New Zealand is shown in Figure 3.9. During the afternoon, deep boundary-layer depths can be seen over the Australian continent driven by daytime heating (Figure 3.9a), while they are substantially lower during the nighttime, as shown in Figure 3.9b. Deep boundary-layer depths over the Southern Ocean were caused by intense cold advection, while the boundary layer reached moderate depths close to the cyclonic circulation center over the Tasman Sea.

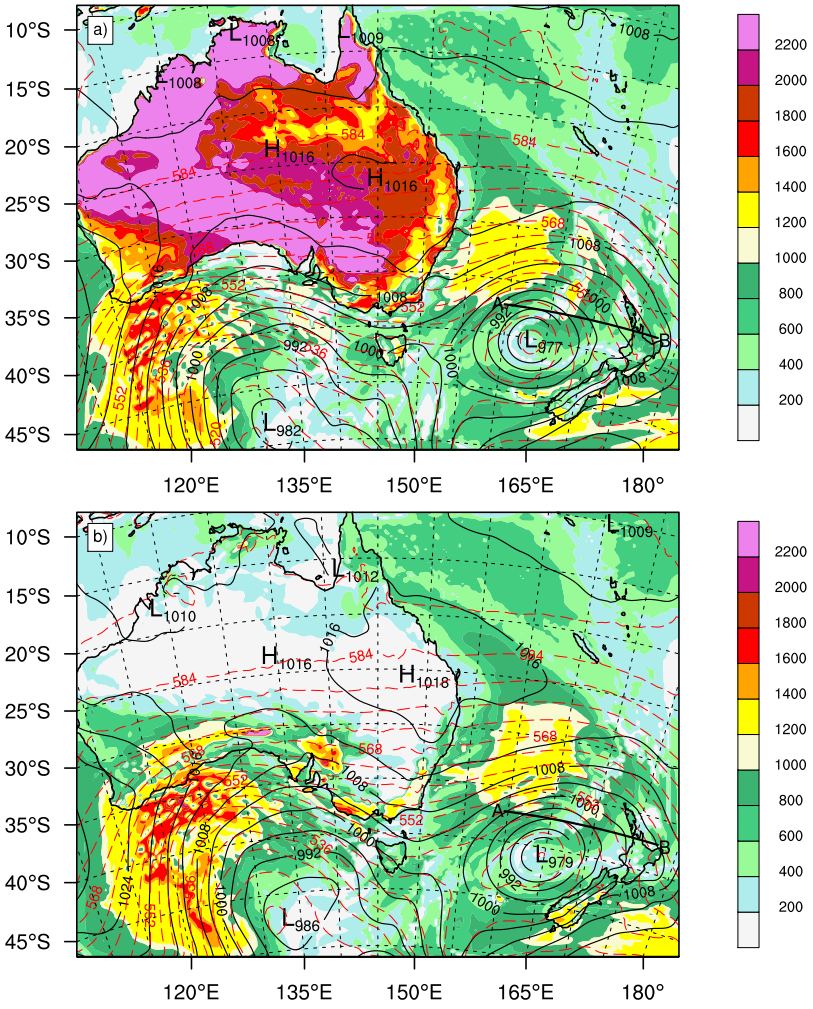

Figure 3.9. Similar to Figure 2.7 but at a) 0600 UTC on 24 September, and b) 1200 UTC on 24 September 2009. The bold black lines from A to B mark the vertical cross-sections plotted in Figure 3.10.

Vertical cross-sections over the eastern Tasman Sea and over the North Island of New Zealand along the line AB in Figure 3.9 are shown in Figure 3.10. Relatively high PM_{10} concentrations (up to ~400 μg m^{-3}) clearly illustrate the simulated long-range southeast-

ward transport of Australian dust over the Tasman Sea. The peak dust values are predicted to be primarily located below around 3 km, demonstrating the low-level nature of dust transport. The low-level dust plume was predicted to be located over the west of Auckland at 0600 UTC on 24 September 2009 (Figure 3.10a), but shifted further east by 1200 UTC (Figure 3.10b). Given that ground-based measurements at Auckland indicate that PM_{10} concentrations started to increase at around 0900 UTC on 24 September and reached the maximum value of ~350 μg m^{-3} at around 1300 UTC (not shown), Figure 3.10 shows that the model adequately predicted the time of dust arrival over the region.

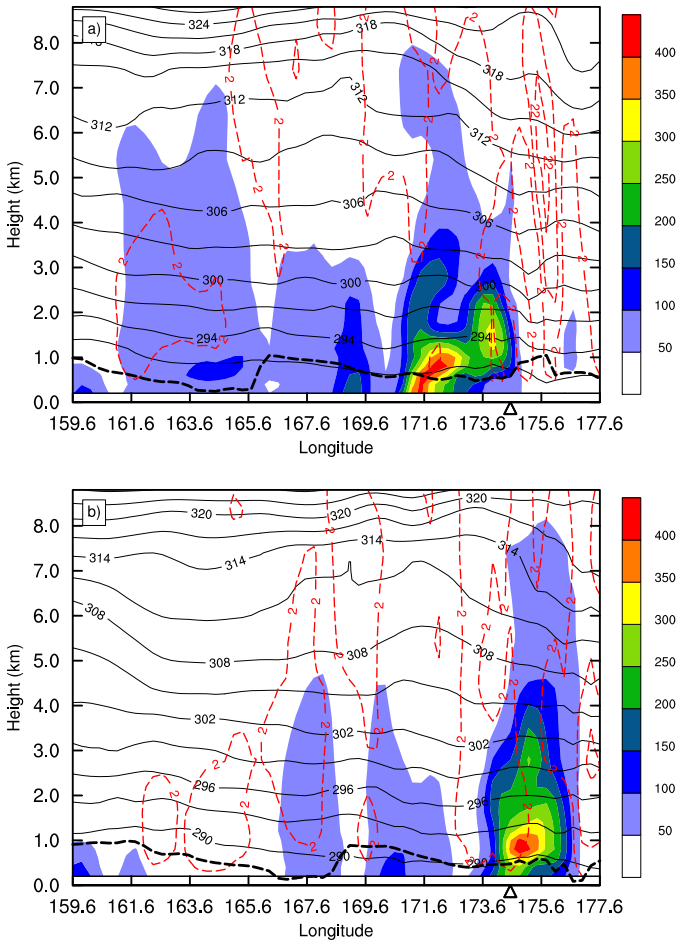

Figure 3.10. Similar to Figure 2.8, but cross-sections are along the line from A to B shown in Figure 3.9 at a) 0600 UTC on 24 September, and b) 1200 UTC on 24 September 2009. The approximate location of Auckland is shown by the arrow on the X axis.

3.5.2 Dust Concentration Prior to and After the Arrival of the Cold Front

The strong forcing imposed by the cold front is evident in the simulated vertical profiles of PM_{10} concentrations shown in Figure 3.11. It is clear that the cold front passed through the Elcombe region (29.97°S and 150.34°E), so that northwesterly winds were replaced by southwesterly winds (as shown by the isobars in Figure 3.11), causing the temperature to drop significantly. Before the air mass change, PM_{10} concentration is predicted to have increased with height in the lower atmosphere (Figure 3.11c). This is due to the development of a very stable near-surface boundary layer accompanied by low particle concentrations primarily due to surface deposition. As a result, the maximum particle concentration occurred at around 1 km height in the residual layer (the elevated portion of a mixed boundary layer that remains after a stable boundary layer establishes at the ground). The passage of the cold front was predicted to produce a significant increase of surface PM_{10} concentrations reaching 5000 μg m^{-3}, around one order of magnitude greater than the values before the arrival of the cold front. Even with vigorous vertical mixing, the PM_{10} concentration declined with height as gravity tends to settle dust particles. Furthermore, boundary-layer depth increased considerably from ~0.1 km in the pre-frontal to ~1.2 km in the post-frontal condition.

Vertical distribution of mineral dust in the pre- and post-frontal conditions depends on the stratification of the atmosphere which can be evaluated by analysing vertical profiles of potential temperature. These profiles derived from the WRF model for the Elcombe region are displayed in Figures 3.11c and 3.11d. The air mass change was predicted to cause a substantial decrease of surface potential temperature from 303 K to ~295 K and an increase of near-surface wind speeds (up to 4 m s^{-1}, not shown). Furthermore, before the arrival of the cold front, there is a nocturnal strongly stable near-surface layer, capped by a residual layer from the previous day, and a stable cap above that at around 2-3 km (Figure 3.11c). After the air mass change (Figure 3.11d), the near-surface layer is only weakly stable, before becoming well-mixed up to about 1 km, with a strong cap above that, indicating the contribution of the cold front to development of a well-mixed layer.

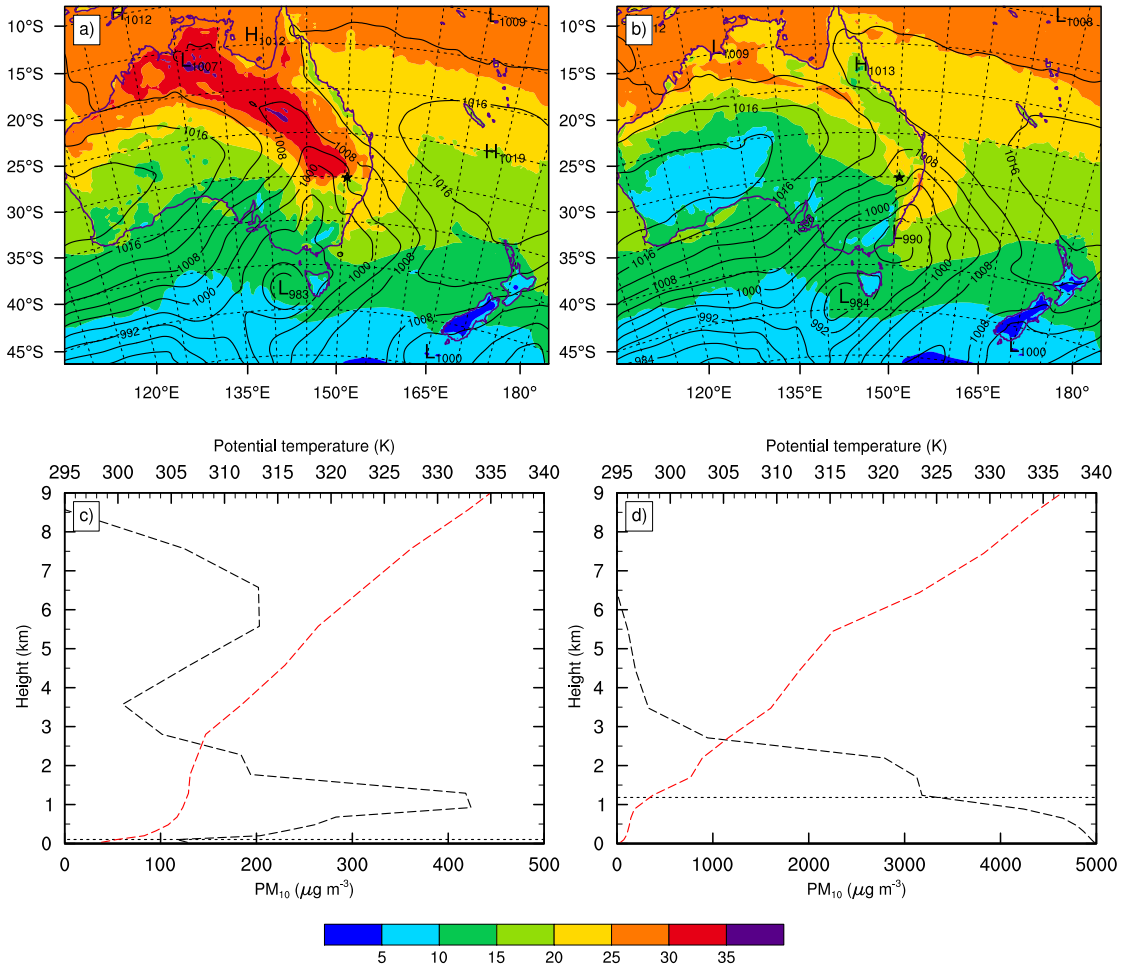

Figure 3.11. Simulation of mean sea level pressure (contour interval of 4 hPa), 2-metre temperature (°C, as shown in scale) and vertical profile of PM_{10} concentration (black dashed line, μg m^{-3}), PBL depth (black horizontal dotted line, km) and potential temperature (red dashed line, K) at Elcombe (29.97°S, 150.34°E, shown by the ⋆ symbol), Australia at 1000 UTC (left panel) and 1800 UTC (right panel) on 22 September 2009. Note the different X axis scales in panels c and d.

Note that the inversion between ~1-1.8 km at 1800 UTC on 22 September may be related to the vertical structure of the cold front. As the cold front was tilted rearward with height, the near-surface layer was in the post-frontal air mass, whereas air above ~1 km appears still to be in the pre-frontal air mass.

3.6 Vertical Structure of the Dust Plume Retrieved from CALIOP

Vertical cross-sections from the CALIOP data set over the CALIPSO orbital paths along the lines AB in Figure 3.2 are given in Figures 3.12 and 3.13. Over central Australia at 1600 UTC on 22 September, a dust layer reached a height of approximately 2 km between $\sim 20 - 25°$S and $138.4 - 137.3°$E (Figure 3.12a). Over western Australia, a well-mixed aerosol layer extended from the surface to around 0.5 km. There was also a small dust load over the northwestern tropical region of Australia ($\sim$ 15°S, 122.3°E) which was lifted to around 4 km (although this is a little difficult to see in Figure 3.12b). During southeastward transport, the top of the dust plumes varied substantially, depending on the various atmospheric processes discussed in Section 3.5.1, reaching up to 3 km over eastern Australia (Figure 3.13a) and the Tasman Sea (Figure 3.13b).

Figure 3.14 shows vertical profiles of regionally-averaged dust extinction coefficients at 532 nm over the CALIPSO orbital paths shown in Figure 3.2 (the latitude varies from $45 - 10°$S). The extinction coefficient measures attenuation of light passing through the atmosphere due to scattering and absorption by dust aerosols. Over central Australia, the dust layer had a strong extinction coefficient peak at around 0.4 km and a second weaker peak at around 1.9 km (Figure 3.14a), while eastern Australia was associated with one major extinction coefficient peak near the surface reaching 0.6 km^{-1} and a second peak at 2 km height with a value of $\sim$0.17 km^{-1} (Figure 3.14b). Over western Australia, two peaks close to the surface and around 1 km altitude were observed (Figure 3.14c), although the dust extinction coefficients over this area were substantially less (with a maximum value of 0.11 km^{-1}) than eastern Australia (with a maximum value of 0.6 km^{-1}). This indicates that only small quantities of dust were transported to western Australia, which is consistent with the eight-day MODIS data shown in Figure 3.5. High dust extinction coefficient values were observed over the Tasman Sea between 0.1 and 1.5 km above the ground, with three remarkable peaks at around 0.1, 0.6 and 1.1 km (Figure 3.14d). Although some dust particles were transported to the free atmosphere, primarily by strong ascending motion in the warm conveyor belt, the notable high dust extinction coefficients close to the sur-

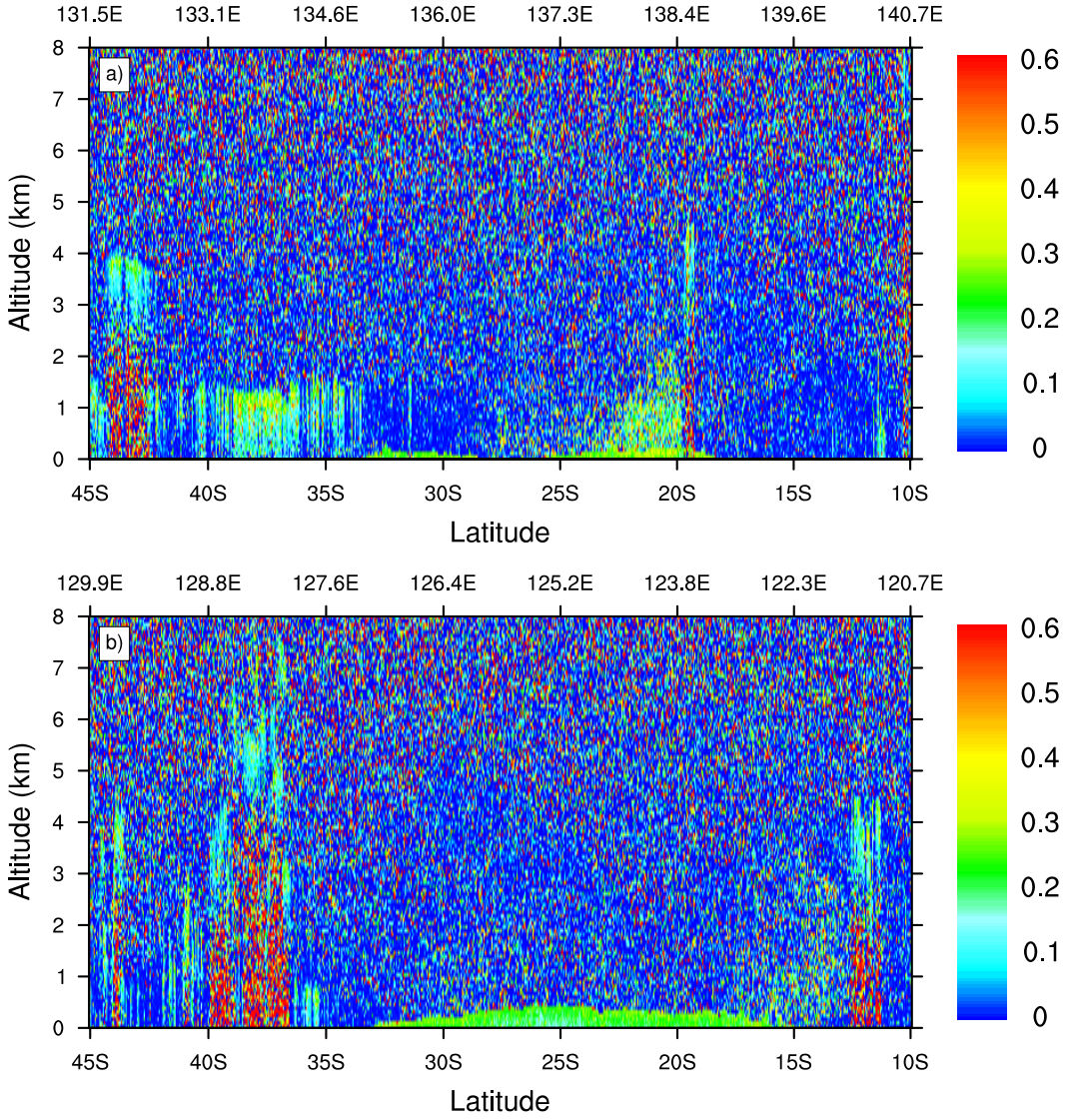

Figure 3.12. Depolarization ratio at 532 nm retrieved from the Level 1B CALIOP data sets during overpasses at around a) 1600 UTC on 22 September, and b) 1637 UTC on 23 September 2009, corresponding to the CALIPSO orbit paths shown in Figures 3.2a and 3.2c, respectively. The top X axis shows the longitude values.

face over eastern Australia and the Tasman Sea suggest that dust was mainly transported within the atmospheric boundary layer. This is not surprising since Australian deserts are not surrounded by high mountains, so that lack of orographic forcing could contribute to the dominance of low-level dust transport from Australia. Figure 3.14d also reveals that there was an elevated dust layer between 4-4.6 km above ground which was separated from the lower dust layer, indicating a weak two-layer structure to the dust plume during its transport over the Tasman Sea.

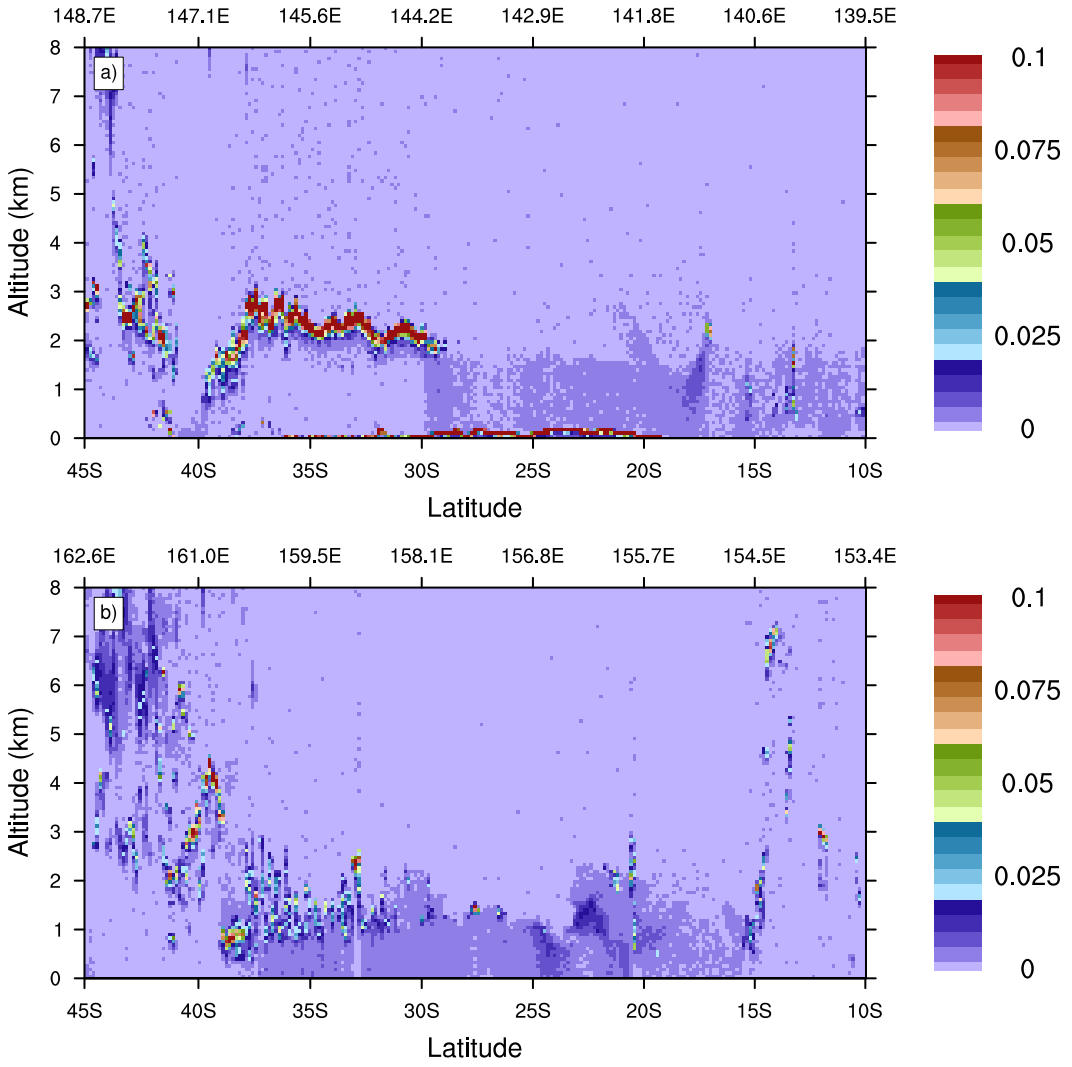

Figure 3.13. Total attenuated backscatter (km $^{-1}$ sr $^{-1}$) at 532 nm retrieved from the Level 1B CALIOP data set during overpasses at around a) 0400 UTC on 23 September, and b) 0300 on 24 September 2009, corresponding to the CALIPSO orbit paths shown in Figure 3.2b and 3.2d, respectively. The top X axis shows the longitude values.

3.7 Discussion and Conclusions

The dust event during 22-23 September 2009 over Australia has been simulated using the WRF/Chem model with the MOSAIC aerosol module comprising eight sectional bins less than 10 μm in diameter, the DUSTRAN module developed by *Shaw et al.* (2008), the YSU PBL scheme and meteorological conditions initialized using FNL reanalysis data from NCEP. The dust event was caused by the passage of a cold front associated with an intense extratropical cyclone over the Southern Ocean. The frontal system is particularly

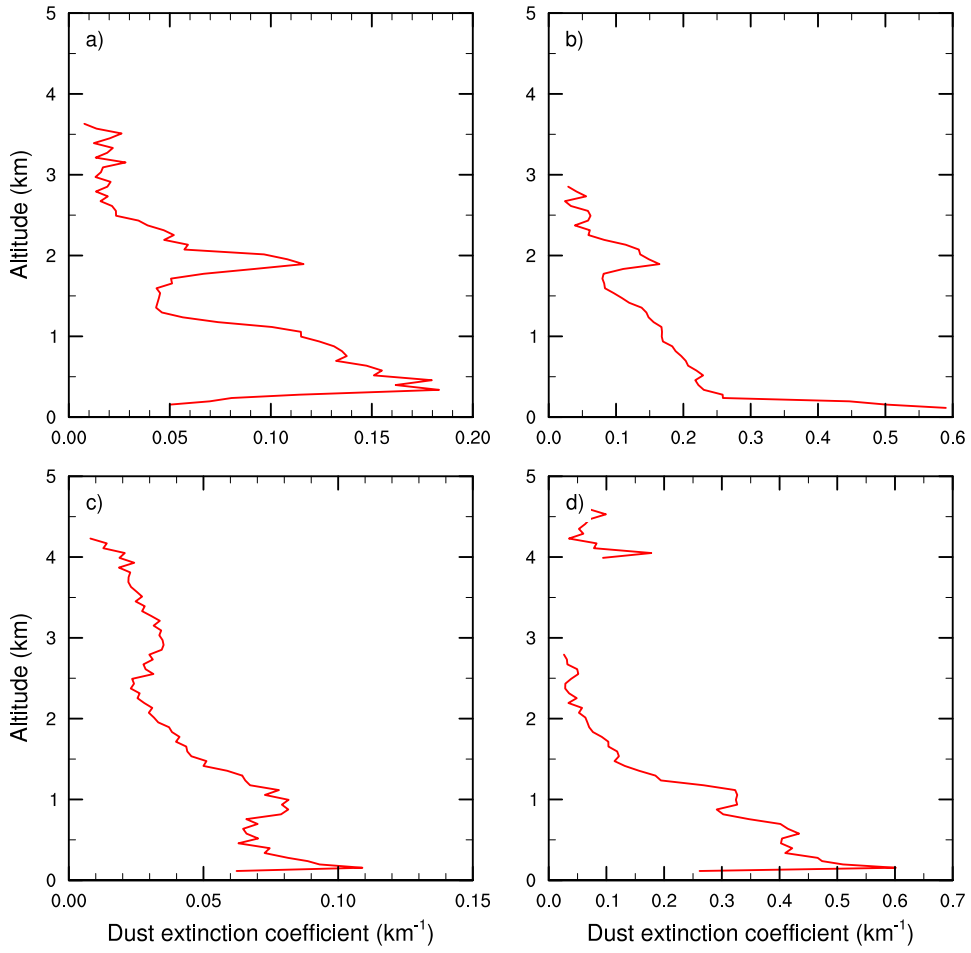

Figure 3.14. Vertical profiles of regionally averaged (corresponding to the CALIPSO orbit paths shown in Figure 3.2) dust aerosol extinction coefficients (km^{-1}) derived from CALIOP data set at around a) 1600 UTC on 22 September, b) 0400 UTC on 23 September, c) 1637 UTC on 23 September, and d) 0300 UTC on 24 September 2009. Note the different X axis scales in all panels.

noteworthy, as it produced a major contribution to both the upward and horizontal transport of dust. The export of dust from Australia was significant since there was a severe drought and low rainfall for the three years prior to the dust event (*Zhao and Running*, 2010; *Leys et al.*, 2011), and dust particles were not removed by rainout during the course of transport.

The simulated AOD was compared with satellite data and the model reproduced the dust pathway to the Tasman Sea and northern regions of Australia reasonably well. However, dust transport to northwestern Australia and finally to the Indian Ocean is overestimated by the model. Comparison of simulated results with ground-based measurements indi-

cates good performance of the model over the study area except for New South Wales, where dust concentrations were significantly underestimated, probably due to underprediction of dust emission from grazing land and mining areas over New South Wales. Furthermore, before and after the peak dust concentrations when wind speeds were weaker, the model overestimated the observed values primarily because the threshold friction velocity was assumed to be constant in the simulation, while in reality it should be increased for fine particles as a result of the increase of inter-particle cohesion forces. Analysis of ground-based measurements indicates that southeastern (New South Wales) and eastern (e.g. Brisbane and Toowoomba in Queensland) Australia were downwind of major dust sources that supplied huge amounts of dust, over a short time period, while northeastern regions (e.g. Townsville Port) were downwind of a source region that supplied less intense dust, but for a longer period (*Leys et al.*, 2011).

Simulation of dust transport routes and MODIS data (Figure 3.4) highlight two main transport pathways of Australian dust-laden air during such events. First, there is a pathway to the Tasman Sea off the southeast coast of Australia as a result of pre-frontal northwesterly winds and eastward moving frontal system, and to northern Australia and to the Coral Sea, Gulf of Carpentaria, Arafura Sea and Timor Sea by post-frontal southwesterly winds and associated anticyclonic circulation. The latitudinal transport of dust to northern Australia by the high-pressure circulation is similar to the Atlantic Ocean where the Azores-Bermuda anticyclonic circulation transports aerosol-laden air from the tropical Atlantic (originating from North African dust episodes and biomass burning) to subtropical regions (*Goudie and Middleton*, 2001). CALIOP observations indicate that transport of dust southeastwards to the Tasman Sea was significantly greater than to other regions. This is expected because of the prevailing westerlies through the mid-latitude troposphere combined with eastward moving frontal systems, as well as pre-frontal northwesterly winds that carry dust plumes to the Tasman Sea. Model results also revealed the potential for some limited transport of dust to the Indian Ocean caused by the anticlockwise circulation of the high-pressure system located over western and central Australia after the passage of the cold front, as well as the southeasterly trade winds over northern

tropical Australia, but such transport is not supported by the MODIS data and appears to be overestimated. Previous research only identified two exit paths of Australian dust: southeastward to the Tasman Sea associated with easterly moving frontal systems and northwestward to the Indian Ocean due to southeasterly trade winds in the north tropical regions (*Knight et al.*, 1995). However, our results show that quite significant amounts of dust may be transported to northern Australia (with eight-day AOD values more than 0.6 as shown in Figure 3.5), extending from the Coral Sea northeast of Australia to the Timor Sea to the northwest. This means that in addition to New Zealand to the southeast of Australia, countries to the north can also be affected by severe Australian dust storms.

Model simulation results indicate that there was a significant variation in boundary-layer structure during the passage of cold frontal systems across Australia. Boundary-layer depth was deeper behind the cold front due to strong cold advection over relatively warm surfaces. This region was also associated with the maximum PM_{10} concentrations as a result of strong near-surface wind speeds. This suggests that dust was mainly being picked up from the surface by post-frontal winds, consistent with the results of *Leys et al.* (2011). Dust particles were then mixed through the depth of the boundary layer behind the cold front, due to the substantial turbulent mixing in the well-mixed boundary layer. Over the area dominated by anticyclonic circulation, particle concentrations were low and less elevated. Large-scale descending motion trapped the particles in lower layers of the atmosphere, and subsequent horizontal transport toward low-pressure regions occurred by divergent winds around the fringes of the anticyclone. In the warm sector ahead of the cold front, boundary-layer depth was relatively shallow due to warm advection over cold surfaces. However, warm advection contributed to strong ascending motions in the conveyor belt along the frontal zone, which appears to contribute to transport of some dust to the free atmosphere. Indeed, simulation results suggest that the maximum height that the dust plume could reach (~8 km) was ahead of the cold front, suggesting that the warm conveyor belt is the most important mechanism for transporting particles from the boundary layer to the free atmosphere.

As we often observe stronger wind speeds in the free atmosphere than the boundary layer, dust particles within the free atmosphere tend to be transported longer distances and affect downwind regions further away from the source of dust. Furthermore, there is no dry deposition in the free atmosphere, and hence, dust particles have longer atmospheric lifetimes, which in turn enhance their climate forcing. Consequently, transport of particles from the boundary layer to the free atmosphere associated with the ascending motion along the leading edge of the cold front is a key process linking local dust sources to regional and global distribution of dust aerosols.

Analysis of CALIOP data indicates that dust originating from Australia can extend to more than 4 km above the ground (Figure 3.14). CALIOP observations detected a layer with high dust extinction coefficient values from near the surface to around 3 km over eastern Australia and the Tasman Sea (with a maximum value of 0.6 km^{-1} close to the surface). Another dust layer with a smaller dust extinction coefficient (with a maximum value of 0.15 km^{-1}) was observed at around 4-4.6 km over the Tasman Sea, which was unconnected with the near-surface dust layer. These results suggest that Australian dust can be transported towards New Zealand and beyond within both the lower and mid-troposphere. This two-layer dust transport is similar to the structures identified over eastern China and the western Pacific Ocean, associated with contributions from two major dust sources: the Gobi and Taklamakan deserts (*Huang et al.*, 2008).

Although model simulation results indicate that some of the dust can reach as high as ~8 km ahead of the cold front, these dust aerosols were not detected by the CALIOP data, except in Figure 3.14d where the previously mentioned elevated dust layer was observed. This might be caused by the fact that the orbit paths of the selected CALIOP data do not coincide with the location of the warm conveyor belt. In addition, simulation results indicate that significant amounts of Australian dust remained in the lower atmosphere, primarily within the boundary layer, and only relatively small quantities transported to an altitude of more than 4 km (Figures 3.8 and 3.10). Consequently, model simulations indicate that in this event most of the dust was transported within the lower atmosphere. Low-level transport of Australian dust was partly caused by the lack of significant orog-

raphy, so that dust plumes were less affected by upward motion induced by orographic forcing. This is in contrast to the Taklamakan desert where low-level dust transport is trapped by surrounding high mountains, so that orographic forcing advects dust vertically to the free atmosphere (*Uno et al.*, 2009), and hence a concentrated dust layer was observed at around 3 km (*Huang et al.*, 2008). However, the situation in Australia is similar to boundary-layer dust transport from the Gobi desert of southern Mongolia and northern China (*Uno et al.*, 2009). Also, with vigorous mixing occurring behind the cold front, the high near-surface PM_{10} concentrations shown in Figures 3.8 and 3.10 could be caused by the fact that dust particles are typically in the coarse particle size range and gravitational settling prevented significant amounts of them being transported to higher levels.

Since dust plumes were mostly transported in the lower atmosphere over the Tasman Sea, in contrast to the Saharan Air Layer (SAL) over the Atlantic Ocean (Liu2008), it is expected that dust aerosols would become mixed with other aerosols types, such as sea salt, leading to changes in chemical composition and size of the aerosols, which in turn affects their optical properties. The dominance of dust transport within the boundary layer also suggests that Australian dust aerosols only slightly perturb the surface temperature, because heating of the dust layer associated with absorption of radiation by dust aerosols offsets the surface cooling (due to reflection of shortwave radiation by dust) through exchange of heat between the dust layer and the surface by turbulent mixing within the atmospheric boundary layer (*Miller and Tegen*, 1998). This is in contrast to North African (*Liu et al.*, 2008) and Asian (Taklamakan) (*Huang et al.*, 2008) dust source regions where layers have been identified at much greater height above ground, which can have a larger surface cooling effect. Furthermore, since annual dust emission from Australia is significantly lower than North Africa and Asia (*Shao et al.*, 2007; *Rotstayn et al.*, 2009), this further supports the idea that Australian dust has a lesser impact on regional and global climate compared to the other main dust source areas in the Northern Hemisphere.

Model simulations show that dust is deposited largely over the Tasman Sea, where dry removal is the dominant process because dust was mainly transported within the boundary layer and lower troposphere, and therefore subject to deposition by gravitational settling

and turbulent eddies. The substantial dry deposition of Australian dust is evident by comparing the maximum PM_{10} concentrations over eastern Australia (~2600 μg m^{-3}) with those over the central (~1400 μg m^{-3}) and eastern (~400 μg m^{-3}) Tasman Sea. As Australian dust is high in iron content (*Rotstayn et al.*, 2009), the substantial dry deposition over the Tasman Sea can lead to phytoplankton blooms, and therefore can increase atmospheric CO_2 uptake.

The conclusions from this study are only based on a single dust event during 22-23 September 2009 and do not necessarily imply that dust transport paths and vertical distribution are similar for other dust episodes. Long-term observation and model simulation and their analysis are necessary to determine the typical vertical distribution and transport pathways of Australian dust.

Chapter 4

Feedback Between Windblown Dust and Boundary-layer Characteristics

Alizadeh Choobari, O., P. Zawar-Reza and A. Sturman (2012), Feedback between wind-blown dust and planetary boundary- layer characteristics: Sensitivity to boundary and surface layer parameterizations. ***Atmospheric Environment, 61*****, 294-304, doi:10.1016/j.atmosenv.2012.07.038.**

Abstract. Inclusion of direct radiative forcing by mineral dust is important for accurate simulation of meteorological conditions, and planetary boundary-layer (PBL) parameterization plays a critical role in proper representation of such forcing. The direct radiative forcing of mineral dust and its feedback effects on boundary-layer dynamics are investigated using the Weather Research and Forecasting with Chemistry (WRF/Chem) model. Furthermore, this study examines the sensitivity of dust radiative effects associated with two different PBL schemes: the Yonsei University (YSU) scheme with both Noah and RUC (Rapid Update Cycle) land-surface models (LSMs), and the Mellor-Yamada-Janjic (MYJ) scheme. By reflecting and absorbing solar radiation, dust aerosols are predicted to cool the atmosphere from the surface to near the boundary-layer top, while warm the boundary-layer top and lower free atmosphere by absorbing both solar and infrared radiation. The simulated surface cooling and heating at the boundary-layer top stabilizes the lower atmosphere, causing a reduction of boundary-layer depth. The stabilized atmosphere restricts vertical exchange of momentum, resulting in an overall decrease of wind speeds in the lower boundary layer and an increase within the upper boundary layer and lower free atmosphere. Use of the YSU-RUC scheme resulted in larger dust feedback effects on atmospheric characteristics, while the MYJ scheme produced lower radiative feedback effects because of lower dust concentrations and reduced vertical mixing of dust. The differences in radiative forcing by dust in model runs are found to be mainly due to

differences in PBL scheme, rather than the LSM used in the model.

Keywords: Radiative forcing by dust; Boundary layer; PBL parameterization; Land-surface model (LSM); WRF/Chem

4.1 Introduction

Approximately 35% of the Earth's land surface has the potential for dust emission (*Tegen and Fung*, 1994), so that dust is a major component of atmospheric aerosols, with an estimated global annual emission of 1950-2400 Tg (*Ginoux et al.*, 2004). The Australian continent is largely arid and is the driest inhabited continent of the world (*Botterill*, 2003), primarily due to low annual precipitation (*Prospero et al.*, 2002). Although large portions of the continent are arid, Australian average dust emission is small relative to major sources in the Northern Hemisphere (*Prospero et al.*, 2002). However, severe dust episodes comparable with moderate Northern Hemispheric dust events do occur, particularly in drought years (*Shao et al.*, 2007). Dust activity in Australia begins late in the year, usually September, peaking in December-February, and then decreasing in intensity until May (*Prospero et al.*, 2002). Although occasional dust activity is seen across northern Australia in the Carpentaria Basin, as well as some areas over New South Wales and Queensland, the largest and most persistent source of dust is Lake Eyre Basin in South Australia (*Prospero et al.*, 2002).

Mineral dust aerosols change the radiative balance of the atmosphere and Earth system directly by scattering and absorbing various radiation components in the atmosphere, which in turn affects surface energy fluxes and the structure of the atmospheric planetary boundary layer (PBL) (*Miller et al.*, 2004b). Furthermore, dust aerosols impact on the Earth's radiation budget semi-directly by influencing cloud cover and indirectly, by influencing cloud optical properties and lifetime (*Huang et al.*, 2006).

Numerous studies have shown that direct radiative forcing by dust aerosols has an impact on climate (e.g. *Perlwitz et al.*, 2001). By scattering and absorbing shortwave radia-

tion, mineral dust aerosols cool the Earth's surface (*Miller et al.*, 2004b). The absorbing nature of dust, on the other hand, has consequences for atmospheric heating (*Quijano et al.*, 2000). Cooling the surface and heating the atmosphere contribute to an increase in boundary-layer stability (*Perlwitz et al.*, 2001; *Miller et al.*, 2004b), restricting the downward transport of momentum within the PBL, resulting in a decrease of near-surface wind speeds (*Jacobson*, 2002). However, surface warming may occur through reduced cloud cover (*Mallet et al.*, 2009), which increases surface temperature and near-surface wind speed. In spite of this extant literature, further investigation is required to fully understand how dust-induced changes to the radiation balance affect atmospheric boundary-layer dynamics.

Regional radiative forcing by mineral dust is a key factor in understanding regional climate change. Yet, few modelling studies have investigated the regional radiative forcing of mineral dust over Australia. Indeed, investigations have mainly been carried out to understand dust transport pathways, leaving the radiative effects of Australian dust aerosols still an open question. This chapter therefore aims to investigate shortwave direct radiative forcing of mineral dust and subsequent feedback effects on atmospheric dynamics, by examining effects on temperature, horizontal wind speeds, and boundary-layer depth in cloudy conditions during a severe dust event that occurred on 22-23 September 2009 over the Australian region. A fully-coupled Weather Research and Forecasting with Chemistry (WRF/Chem) regional model has been applied for this purpose as it simulates aerosol processes simultaneously with meteorology (*Grell et al.*, 2005). The indirect effects of mineral dust are not considered in this study as the dust event was caused by the passage of a dry frontal system (i.e. without precipitation).

Different PBL and land-surface schemes adopt different assumptions in terms of transport of heat, momentum and moisture (*Hu et al.*, 2010), which may lead to differences in simulation of dust entrainment, its vertical mixing, horizontal transport and radiative feedback effects. The sensitivity of the WRF model results to the PBL parameterization has been extensively evaluated (e.g. *Hu et al.*, 2010). The results indicate that simulations with the Yonsei University (YSU) PBL scheme are in better agreement with observations

(*Hu et al.*, 2010) than the Mellor-Yamada-Janjic (MYJ) PBL scheme. However, there is a lack of investigation of the sensitivity of radiative forcing by dust to the PBL scheme and land-surface model (LSM) used in the WRF/Chem model. The YSU PBL scheme (with both the Noah and Rapid Update Cycle (RUC) LSMs) has been compared with the MYJ PBL scheme (with the Noah LSM) to better characterize the sensitivity of dust radiative feedback effects on the atmosphere to the PBL parameterization and land-surface processes.

Model results have been compared with available satellite data and ground-based measurements elsewhere (*Alizadeh Choobari et al.*, 2012a), and are not discussed here. Model description is presented in Section 4.2. The nature of the dust storm is the subject of Section 4.3. Section 4.4 outlines the radiative forcing by mineral dust and its feedback effects on boundary-layer dynamics, while Section 4.5 investigates sensitivity of such feedback effects to the PBL parameterization and LSM. Section 4.6 presents an overall conclusion.

4.2 Model Description and Experimental Setup

4.2.1 Model Description

A fully-coupled WRF/Chem regional model was applied for the days 20-26 September 2009. The physics options used in the initial simulation were the Yonsei University (YSU) PBL scheme (*Hong et al.*, 2006; *Hong*, 2010), the Noah LSM (*Ek et al.*, 2003) and the Monin-Obukhov surface layer scheme (*Obukhov*, 1971). The Lin (*Lin et al.*, 1983) and Grell 3D (*Grell*, 1993) schemes were used to represent cloud microphysics and convection processes. The Goddard shortwave scheme was used to include aerosol shortwave radiative effects and the Rapid Radiative Transfer Model (RRTM) was used for the longwave scheme (*Wild et al.*, 2000). The second part of the modelling used other PBL schemes and LSMs as described in Section 4.2.2.

The gas-phase chemical mechanism was the Carbon-Bond Mechanism version Z (CBM-Z, *Zaveri and Peters* (1999)), and photolysis was calculated using the Fast-J photolysis scheme (*Wild et al.*, 2000). The aerosol module was parameterized using the Model for Simulating Aerosol Interactions and Chemistry (MOSAIC) (*Zaveri et al.*, 2008), which adopts eight size sectional bins for aerosols less than 10 μm in diameter based on dry particle diameters. The refractive index was calculated by volume averaging for each size bin, and Mie theory was used to estimate the extinction efficiency, the scattering efficiency and the asymmetry factor. Optical properties were then calculated by summation over all size bins. The RE-analysis of the TROpospheric (RETRO) chemical composition over the past 40 years (`http://retro.enes.org/index.shtml`) and the Emission Database for Global Atmospheric Research (EDGAR) (`http://www.mnp.nl/edgar/introduction`) (on a $0.5^\circ \times 0.5^\circ$ and $1^\circ \times 1^\circ$ grid resolution, respectively) were applied to generate gridded anthropogenic emissions. Aerosols are mainly composed of black carbon, sulfate, nitrate, ammonium, organic matter, water and mineral dust.

The dust emission scheme is based on the dust transport (DUSTRAN) module developed by *Shaw et al.* (2008) which calculates the dust emission flux from the surface as:

$$F = \alpha C u_*^4 \left(1 - \frac{f_w u_{*t}}{u_*}\right) \quad for \;\; u_* \geq u_{*t} \tag{4.1}$$

where α depends on vegetation cover and ranges from zero to 1, C = 1.0×10^{-14} g cm^{-6} s^{-3} is an empirically derived coefficient, u_{*t} (cm s^{-1}) is the threshold friction velocity below which dust emission is zero, u_* (cm s^{-1}) is the friction velocity, and f_w is the soil wetness factor. A detailed description of the DUSTRAN scheme can be found in *Alizadeh Choobari et al.* (2012a). The real and imaginary parts of the refractive index of mineral dust were set to 1.55 + 0.003i following *Zhao et al.* (2010). The real part is relatively well defined, but the imaginary part is uncertain and the selected value is taken to be the midpoint of values ranging from 0.0004i to 0.006i as suggested in previous studies (e.g. *Dubovik et al.*, 2002).

The model domain covers Australia, New Zealand and the Tasman Sea using 230 × 170

grid points with a horizontal spacing of 27 km, and 27 vertical layers extending from the surface to 50 hPa, with a finer resolution in the lower part of the atmosphere. The National Centers for Environmental Prediction (NCEP) Final Analysis (FNL) re-analysis data were used as meteorological initial and boundary conditions.

4.2.2 Experimental Setup

Initially, two simulations were performed, both using the Monin-Obukhov surface layer scheme and the unified Noah LSM (referred to as YSU-Noah). The first comprised a model setup that did not include radiative effects of aerosols on atmospheric variables at all, despite the inclusion of dust. This model run is used as a control experiment. The second interactive experiment simulated the two-way interaction between atmospheric processes and aerosols, so that meteorological variables respond to the direct radiative effects of aerosols. Radiative forcing by dust and dynamic atmospheric response were calculated from the differences between the results of the two simulations (referred to as the anomalies). Note that throughout the manuscript the reference to boundary-layer depth and free atmosphere are for the control simulation unless the interactive simulation is specifically mentioned. The contribution of sea salt and biomass smoke to atmospheric aerosols was omitted here to mainly demonstrate the impact of dust aerosols.

In addition, four other simulations have been conducted. Two of them employed the YSU PBL parameterization with the Monin-Obukhov surface layer scheme and the RUC LSM (referred to as YSU-RUC). The radiative forcing by mineral dust was turned off and on for these two simulations, respectively. Two other experiments employed the MYJ (*Janjic*, 1990) PBL parameterization with the Monin-Obukhov (Janjic Eta) surface layer scheme and the unified Noah LSM (referred to as MYJ-Noah). Again, the radiative forcing by mineral dust for these two simulations was turned off and on, respectively. Table 4.1 summarizes the setup of all experiments.

Table 4.1. The setup of all modelled experiments that were conducted.

Experiments	PBL	LSM	Surface layer scheme	Radiative forcing
Experiment1[a]	YSU	Noah	Monin-Obukhov	off
Experiment2	YSU	Noah	Monin-Obukhov	on
Experiment3	YSU	RUC	Monin-Obukhov	off
Experiment4	YSU	RUC	Monin-Obukhov	on
Experiment5	MYJ	Noah	Monin-Obukhov (Janjic Eta)	off
Experiment6	MYJ	Noah	Monin-Obukhov (Janjic Eta)	on

[a] The control experiment

4.3 Dust Storm Features

The dust event of 22-23 September was characterized by an extratropical cyclone associated with an active cold front that crossed the Southern Ocean and influenced Australia (Figure 4.1a). Intense cold advection was evident over southern and central Australia, associated with the strong southwesterly winds identified by closely spaced isobars, allowing the dust to be picked up from the desert surfaces into the air. Consequently, notably high PM_{10} concentrations exceeding 4000 μg m^{-3} were simulated over central eastern Australia (the source of dust). By 0400 UTC on 23 September the cyclonic system had intensified and moved eastward, causing the dust to be transported to the Tasman Sea. Dust was also partly transported to northern Australia by a developing high-pressure circulation (Figure 4.1b, outside the source area of dust). The high-pressure system dominated over western and central Australia and the associated subsidence was able to trap dust aerosols close to the ground. Figure 4.1 clearly highlights the two main exit pathways of aerosol-laden air, to the Tasman Sea by the eastward propagating frontal system and to northern Australia by post-frontal southerly winds (*Alizadeh Choobari et al.*, 2012a).

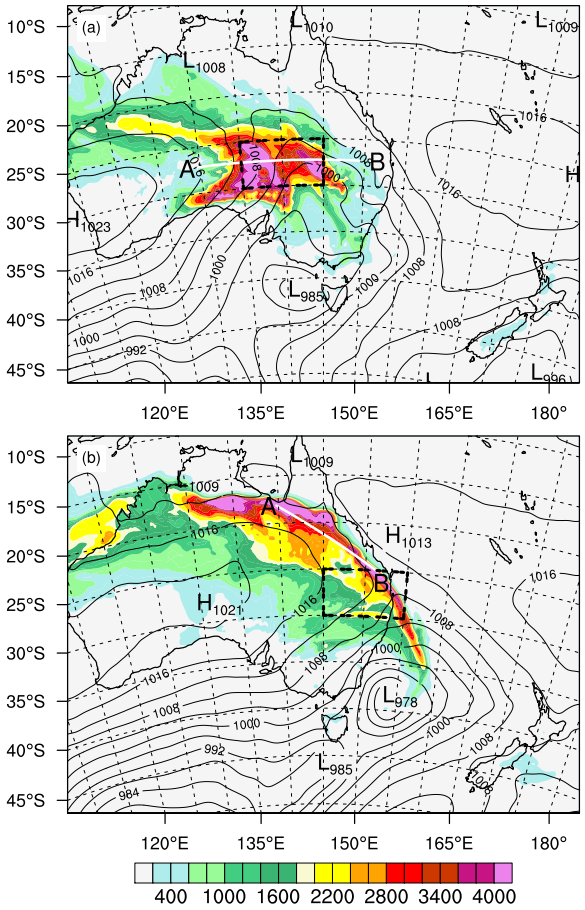

Figure 4.1. Spatial distribution of model simulated PM_{10} concentrations (colours, μg m^{-3}) and mean sea level pressure (solid black line, contour interval of 4 hPa) at 0400 UTC on a) 22 September and b) 23 September 2009. The lines AB mark the vertical cross-sections plotted in Figures 3.3, 3.4 and 3.10. The dashed boxes enclose the area corresponding to the regional average radiative forcing by dust shown in Figure 3.8.

4.4 Dust Feedback Effects on Boundary-layer Dynamics

4.4.1 Near-surface Air Temperature Response

The surface forcing is predicted to be negative beneath the heavy dust layer due to reflection and absorption of shortwave radiation by dust aerosol particles, with a maximum surface cooling of ~ -3°C (Figure 4.2). The geographic location of surface cooling mainly follows the distribution of surface PM_{10} concentrations in Figure 4.1, except over central eastern Australia (around 133 – 140°E) where the surface cooling by dust is predicted to be relatively small over the region with high surface PM_{10} concentrations (compared with

southeastern Australia). This is due to the fact that the dust layer was mainly concentrated near the surface (see Figure 4.3a), and hence absorption of radiation by dust partly compensates for the surface cooling due to reflection of shortwave radiation.

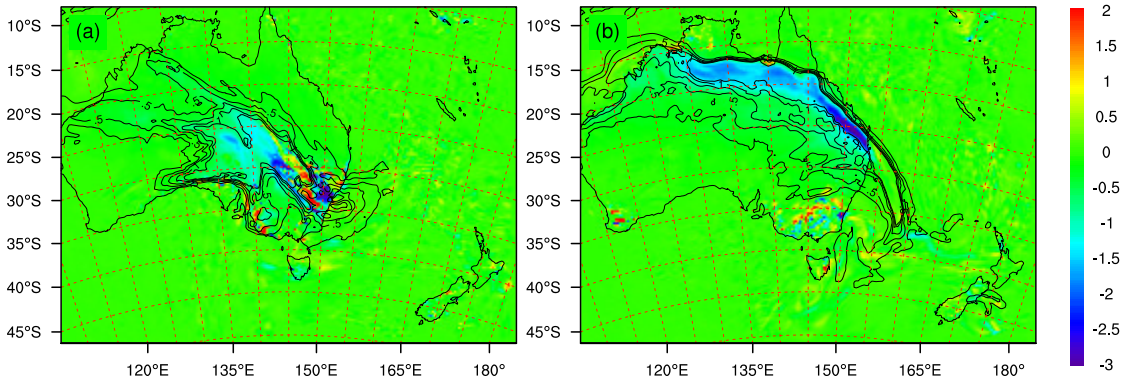

Figure 4.2. Surface temperature (colours, °C) response to radiative forcing by mineral dust and aerosol optical depth (contour interval of 0.25) simulated by the WRF/Chem model at 0400 UTC on a) 22 September and b) 23 September 2009.

The isolated positive values in Figure 4.2 are linked in part to the reduction of cloud fraction through evaporation of clouds as a result of absorption of radiation by dust aerosols, the so-called semi-direct effect (*Huang et al.*, 2006), which is further discussed in Section 4.3. Reduction of cloud cover allows more shortwave radiation to reach the surface, which increases the near-surface air temperature. Note that even in the absence of clouds, radiation absorption by dust aerosols can sometimes lead to a positive forcing. This can occur particularly over bright land surfaces which normally reflect high amounts of solar radiation. However, the existence of the low-level dust layer results in warming due to absorption of radiation which can then be transferred to the surface by turbulent eddies (*Bierwirth et al.*, 2009).

4.4.2 Vertical Cross-section Analysis

A vertical cross-section along the line labelled AB in Figure 4.1a at 0400 UTC (local time 1400 Eastern Standard Time) on 22 September 2009 is depicted in Figure 4.4a, showing the impact of dust on temperature, wind speed and boundary-layer depth. The decrease

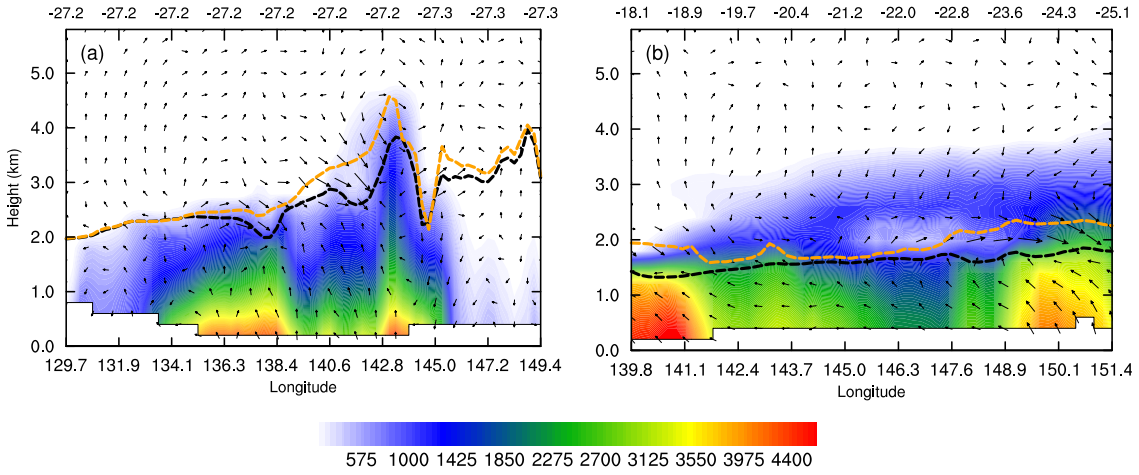

Figure 4.3. Vertical cross-sections (from A to B in Figure 3.1) of PM_{10} concentrations (colours, μg m^{-3}) and horizontal wind speed anomalies (m s^{-1}) at 0400 UTC on a) 22 September and b) 23 September 2009. The thick dashed black and orange lines indicate the boundary-layer depth (km) diagnosed by the model when radiative forcing by dust is on and off, respectively. The top X axis is latitude.

of atmospheric transmission due to the presence of dust caused a reduction of incoming shortwave radiation reaching the surface in the model simulation. Consequently, temperature is shown to decrease in the layer between the surface and near the boundary-layer top (Figure 4.4a). The cooling was greater near the surface, decreased with altitude and changed sign at the boundary-layer top. The absorption of both incoming and reflected shortwave radiation within the dust layer resulted in an increase of temperature at the boundary-layer top and in the lower part of the free atmosphere. Such contrasting cooling of the lower and warming of the upper layers is a unique feature of radiative forcing by absorbing aerosols such as dust. As dust-induced surface cooling and upper layer heating tends to stabilize atmospheric stratification, the boundary-layer depth is simulated to be decreased. The largest decreases are located over regions with substantial surface cooling, while a slight increase of boundary-layer depth at around 144°E (see Figure 4.4a) is caused by the surface warming effect of dust, as shown in Figure 4.5.

The response to radiative forcing by mineral dust is expected to produce both an increase and decrease of wind speeds within the lower atmosphere. Simulation results suggest that the surface cooling was associated with a decrease of wind speeds from the surface to near the top of the boundary layer, while the temperature increase at the boundary-layer top

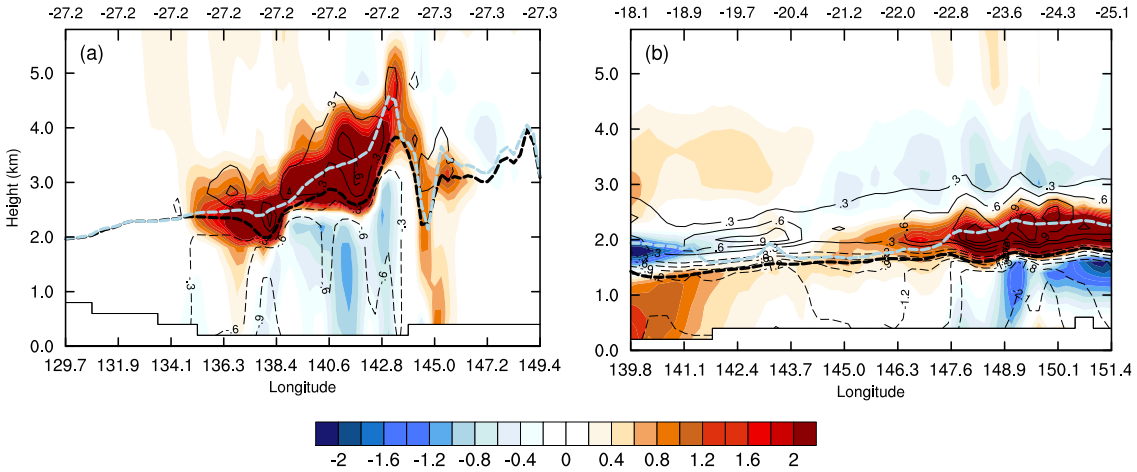

Figure 4.4. Vertical cross-sections (from A to B in Figure 3.1) of air temperature (contour interval of 0.3°C) and horizontal wind speed (colours, m s^{-1}) anomalies due to mineral dust radiative forcing at 0400 UTC on a) 22 September and b) 23 September 2009. The thick dashed black and blue lines indicate the boundary-layer depth (km) diagnosed by the model when radiative forcing by dust is on and off, respectively. The top X axis is latitude.

and in the lower free atmosphere was accompanied by an increase of wind speeds (Figure 4.4a). This is expected because the reduction of temperature near the surface and its increase at the boundary-layer top contribute to an increase in atmospheric stability, and hence, a decrease in vertical exchange of momentum. As upper level winds are generally stronger, this leads to a reduction of wind speed in the lower boundary layer, at the same time as its increase within the upper boundary layer and lower free atmosphere. The wind speed anomalies are more pronounced at the boundary-layer top and in the lower free atmosphere where wind speeds are generally stronger than near the surface. Notice that the increased wind speed propagation downwards from the free atmosphere at around 144 – 145°E (Figure 4.4a) appears to be caused by the surface warming effect of dust (as shown in Figure 4.5), associated with increased incident solar radiation at the surface due to a reduction in cloud cover.

A vertical cross-section along the line labelled AB in Figure 4.1b at 0400 UTC on 23 September 2009 (outside the source area of dust) is shown in Figure 4.4b. Similar to the source area of dust (Figure 4.4a), dust aerosols caused a decrease of temperature in the layer between the surface and near the top of the boundary layer, with a maximum

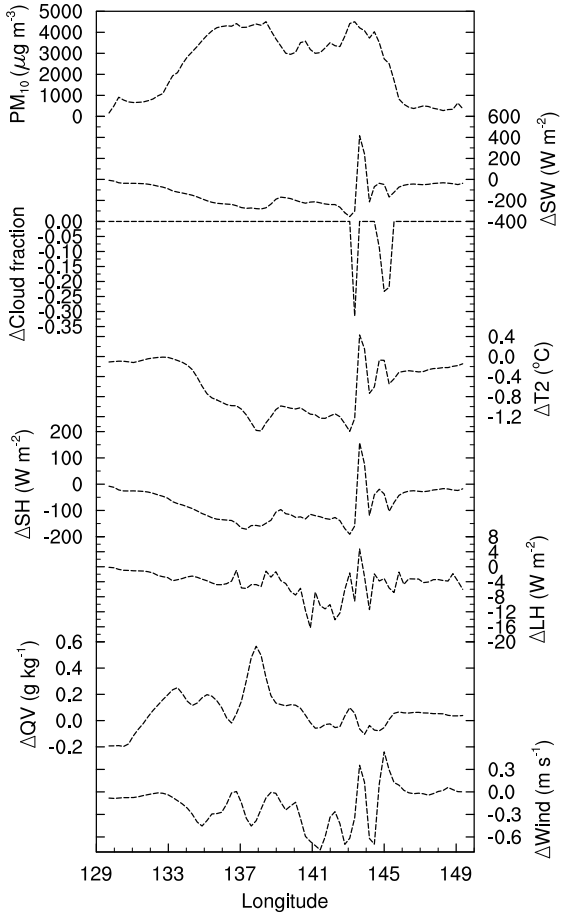

Figure 4.5. Simulated near-surface PM_{10} concentrations (μg m^{-3}), as well as incident shortwave radiation (W m^{-2}), air temperature at 2 metres (°C), surface sensible and latent heat fluxes (W m^{-2}), specific humidity at 2 metres (g kg^{-1}) and wind speed at 10 metres (m s^{-1}) anomalies along the line A to B in Figure 3.1a at 0400 UTC on 22 September 2009.

reduction closer to the surface. In contrast, an increase of temperature is simulated at the boundary-layer top and in the free atmosphere immediately above the boundary layer. Although dust concentrations in the lower atmosphere are higher in northeastern Australia (around 139.8 – 142.4°E) than eastern Australia (around 147.6 – 151.4°E, as shown in Figure 4.3b), temperature changes induced by dust are predicted to be more significant in the latter area, likely due to the presence of more elevated dust aerosols. The combined effect of near-surface cooling and warming within the upper boundary layer stabilized the PBL, thereby contributing to a reduction of boundary-layer depth as shown in Figure 4.4b. These temperature changes resulted in an overall decrease of wind speed in the lower layers of the boundary layer and its increase within the upper boundary layer and

in the lower free atmosphere over eastern Australia (around 143.7 – 151.4°E). This is not surprising as the more stable stratification of the atmosphere is expected to contribute to the reduction of downward transport of stronger wind speeds from the boundary-layer top. However, wind speeds are predicted to increase in the lower layers of the boundary layer and decrease within the upper boundary layer at around 139.8 – 142.4°E due to weaker wind speeds at the boundary-layer top and immediately above, relative to the lower layers (not shown). The weaker winds aloft may be associated with the centre of a large anticyclone located over central Australia (Figure 4.1b).

4.4.3 Horizontal Transect Analysis

Modelled surface PM_{10} concentrations and surface response to radiative forcing by mineral dust along the line labelled AB in Figure 4.1a at 0400 UTC on 22 September are given in Figure 4.5. Dust aerosols are predicted to cause an overall decrease of incident shortwave radiation reaching the surface, as well as a reduction of temperature at 2 metres and surface sensible and latent heat fluxes, with maximum values of -354 W m^{-2}, −1.6°C, -190 W m^{-2} and -18.6 W m^{-2}, respectively. As expected, the surface cooling effect is generally considered to be greater over regions with a higher atmospheric dust load. The smaller change in surface latent heat flux indicates that the reduction of shortwave radiation reaching the surface is balanced mainly through a reduction in surface sensible heat flux, primarily because the region is covered by arid land surfaces where soil moisture availability for evaporation is low.

The region of increased incoming shortwave radiation to the Earth's surface, and consequent positive feedback upon surface temperature and surface sensible and latent heat fluxes was simulated to occur at around 143.6°E with values of 408 W m^{-2}, 0.4°C, 155 W m^{-2} and 4 W m^{-2}, respectively. The near-surface positive forcing was caused by reduced cloud fraction (as shown in Figure 4.5) which resulted from increased air temperature and reduced relative humidity within clouds due to absorption of radiation by dust embedded within them. Note that when cloud fraction decreases, longwave radiation trapped

by clouds decreases, leading to a longwave radiative cooling effect, thereby partly offsetting the localized surface warming effect of dust. Although microphysical interactions of clouds and dust aerosols were not included in the simulations, cloud fraction was still affected by atmospheric changes associated with direct radiative forcing by dust aerosols. The reduction of cloud fraction in turn resulted in an increase of shortwave radiation reaching the surface, which increased surface heat exchanges between the land surface and atmosphere. Note that a slightly negative temperature change predicted to occur at around 144.7°E (~ -0.1°C), in spite of relatively high dust load, also appears to be caused by the reduction of cloud fraction.

Simulation results indicate that the dust forcing produced both a decrease and an increase of specific humidity at 2 metres and wind speed at 10 metres (Figure 4.5). Changes in wind speed range from -0.9 to 0.5 m s^{-1}, but the overall trend was a reduction, while changes in specific humidity range from -0.2 to 0.6 g kg^{-1}, with an overall increase.

The influence of radiative forcing by mineral dust on atmospheric dynamics along the line labelled AB in Figure 4.1b (outside the source area of dust) at 0400 UTC on 23 September is shown in Figure 4.6. Again, by reducing the incoming solar radiation, air temperature at 2 metres and surface sensible and latent heat fluxes were decreased, with maximum values of -337 W m^{-2}, -2.6°C, -173 W m^{-2} and -64.7 W m^{-2}, respectively. As there was no change in cloud fraction, the dust radiative effect was only associated with surface cooling. Similarly, related to the induced surface cooling, specific humidity at 2 metres decreased by up to -0.9 g kg^{-1}. Indeed, the decrease of surface temperature reduced evaporation from the surface (evident from negative surface latent heat flux anomalies), and resulted in a decrease in atmospheric specific humidity (*Yue et al.*, 2010). Note that although dust concentrations at around $148 - 152$°E are less than those at 140°E, there was greater reduction in air temperature at 2 metres, because dust plumes were simulated to be lifted to higher levels in the former region (see Figure 4.3b), and the elevated dust layer can cause more significant surface cooling (*Chung and Zhang*, 2004). In fact, there is little vertical exchange of the heat absorbed by mineral dust between the elevated dust layer and the surface when the dust layer is located well above the boundary layer.

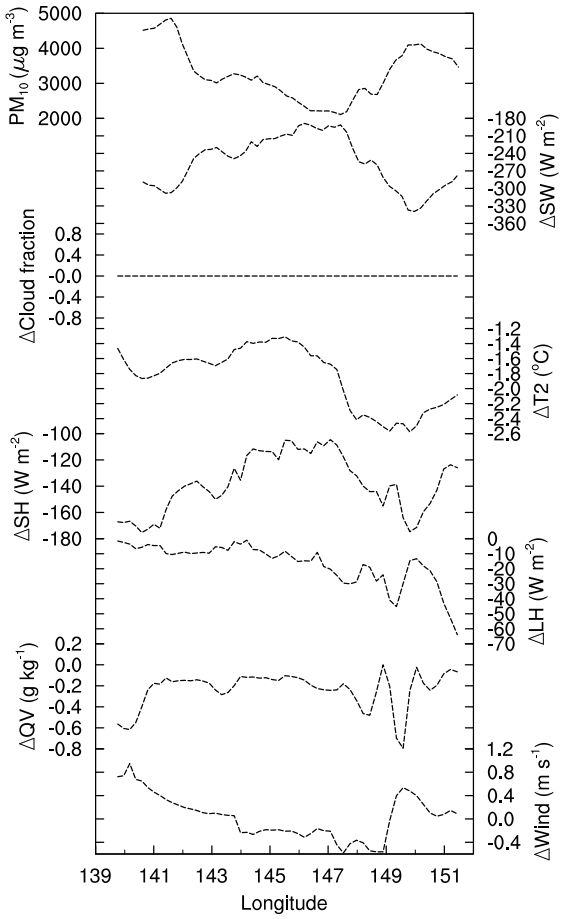

Figure 4.6. Same as Figure 3.5, except along the line A to B in Figure 3.1b at 0400 UTC on 23 September 2009.

Surface cooling is generally associated with a reduction of surface sensible and latent heat fluxes. As the value of surface latent heat flux depends upon soil moisture availability, which is larger over the tropical regions of northeastern Australia, surface latent heat flux anomalies (shown in Figure 4.6) substantially increased compared to the source of dust (shown in Figure 4.5). However, changes of surface sensible heat flux are still larger than surface latent heat flux. Similar to the source regions, mineral dust caused both a decrease and an increase of wind speed at 10 metres along the cross-section, ranging between a negative forcing of -0.7 m s^{-1} to a positive forcing of 1 m s^{-1} (Figure 4.6). As discussed earlier, an increase of wind speed at around 140 – 144°E appears to be caused by stronger wind speeds in the lower atmosphere than aloft.

4.4.4 Dust Aerosol Effects on Surface Pressure and Wind

Figure 4.7 shows mean sea level pressure (MSLP) changes induced by dust aerosols at 0400 UTC on 22 and 23 September 2009 (along the lines labelled AB in Figure 4.1). Overall, MSLP increased as a result of surface cooling and reduced surface heat fluxes by mineral dust. The MSLP increase is greater on 23 September due to stronger surface cooling (compare Figures 4.5 and 4.6). The positive surface pressure anomalies are expected to induce sinking motion, contributing to increased surface dry removal of dust particles.

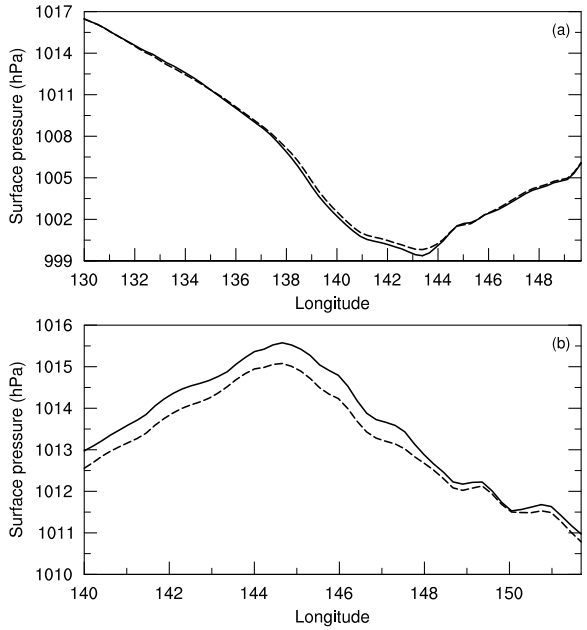

Figure 4.7. Simulated mean sea level pressure (hPa) (along the lines A to B in Figure 3.1) when radiative forcing by dust is on (solid line) and off (dashed line) at 0400 UTC on a) 22 September and b) 23 September 2009.

The surface cooling along with heating of the boundary-layer top and lower free atmosphere appears to be associated with a decrease of southwesterly winds within the lower boundary layer and an increase of westerly winds within the upper boundary layer and lower free atmosphere on 23 September 2009, as shown in the anomaly circulation in Figure 4.3b (specifically between $\sim 145 - 154$°E). The dust-induced surface cooling and the warming effect at the boundary-layer top and immediately above that possibly weaken

the near-surface temperature gradient between the Southern Ocean and northern Australia in the lower atmosphere, and strengthen it at the boundary-layer top. The consequence of this is a weakening of southwesterly wind flows in the lower boundary layer and strengthening of westerly winds at the boundary-layer top, as shown in Figure 4.3b.

4.4.5 Regional Mean Radiative Effects of Dust Aerosol

Modelled regional mean radiative forcing by dust (over the dashed boxes in Figure 4.1) during the local afternoon at 0400 UTC on 22 and 23 September is depicted in Figure 4.8. On both days, dust aerosols induced an average radiative cooling tendency of more than −0.5°C at low levels, and a warming impact of less than 0.5°C above the boundary-layer top. To evaluate the stability of the PBL associated with these temperature changes, the difference between Brunt Vaisala frequencies in the interactive and control simulations was examined. The Brunt Vaisala frequency is calculated as:

$$N^2 = \frac{g}{\theta}\frac{d\theta}{dz} \tag{4.2}$$

where θ (K) is potential temperature, g = 9.8 m s^{-2} is the local acceleration due to gravity, and z is geometric height. $N^2 > 0$ and $N^2 < 0$ represent stable and unstable stratification, respectively. Direct radiative forcing by dust was associated with slightly positive anomaly values of N^2 near the surface and at around 1.5-2.0 km height (Figure 4.8), showing that dust was acting to stabilize the lower atmosphere, which in turn can contribute to a decrease of vertical exchange of both momentum and heat. The average boundary-layer depth is also shown to be decreased by around 0.4 km and 0.1 km on 22 and 23 September, respectively. As upper level winds are generally stronger, less vertical mixing is associated with a reduction of near-surface wind speeds. Therefore, simulation results indicate an approximate 0.4 m s^{-1} and 0.3 m s^{-1} decrease of wind speeds in the lower boundary layer on 22 and 23 September, respectively. In contrast, wind speeds were simulated to be increased up to around 1.9 m s^{-1} and 1.4 m s^{-1} from around 1.7 km height upwards on

22 and 23 September, respectively (Figure 4.8). This suggests that, based on a regional average, there is a general negative correlation between the presence of dust aerosols and near-surface wind speeds, while the correlation is positive with wind strength in the upper boundary layer and lower free atmosphere.

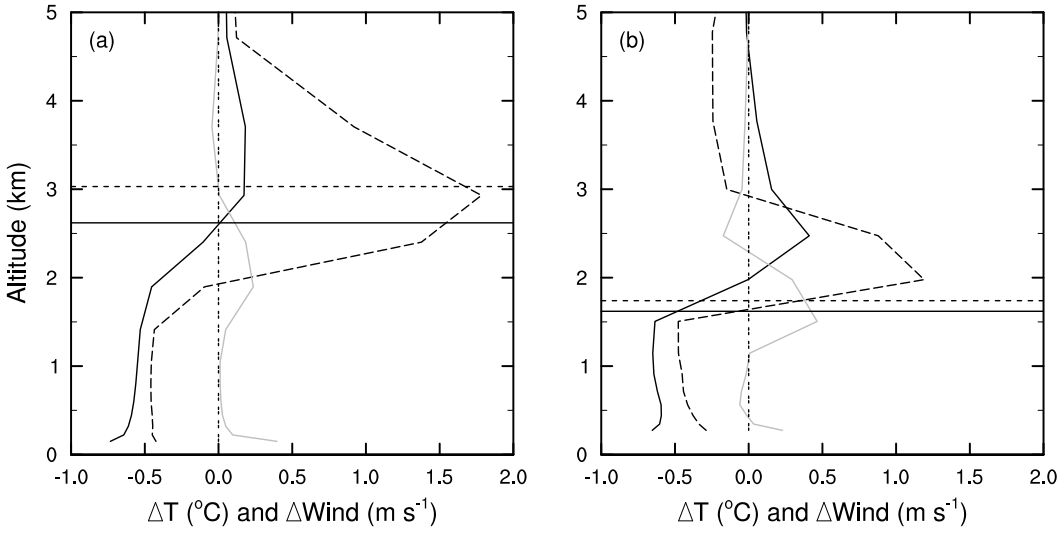

Figure 4.8. Regionally averaged profiles (over the dashed boxes in Figure 3.1) of potential temperature (solid black line, K), wind speed (dashed black line, m s^{-1}) and Brunt Vaisala frequency×10 (gray line) anomalies, as well as boundary-layer depth in the interactive (solid horizontal line, km) and control (dotted horizontal line, km) simulations at 0400 UTC on a) 22 September and b) 23 September 2009.

Table 4.2. Regional mean direct radiative forcing by dust (over the dashed boxes in Figure 3.1) and effects on boundary-layer characteristics at 0400 UTC (local afternoon at 1400 Eastern Standard Time), as well as their sensitivity to the PBL parameterization and land-surface model. SW, T2, SH, LH and QV represent dust-induced changes in incoming shortwave radiation, air temperature at 2 metres, surface sensible heat flux, surface latent heat flux and near-surface specific humidity, respectively.

PBL parameterization	YSU						MYJ		
Land-surface model	Noah			RUC			Noah		
	22 Sep	23 Sep	Mean	22 Sep	23 Sep	Mean	22 Sep	23 Sep	Mean
SW (W m^{-2})	-180.6	-155	-167.8	-245.0	-184.9	-215	-177.0	-130.0	-153.5
T2 (°C)	-0.9	-0.7	-0.8	-3.7	-2.2	-3.0	-0.9	-0.6	-0.8
SH (W m^{-2})	-104.3	-60.0	-82.2	-151.5	-77.7	-114.6	-105.8	-56.7	-81.3
LH (W m^{-2})	-4.9	-10.4	-7.6	-1.1	3.4	1.2	-4.2	-8.1	-6.2
QV (g kg^{-1})	0.06	-0.07	0	0.15	-0.05	0.05	0.03	-0.07	-0.04
Wind speed (m s^{-1})	-0.4	-0.23	-0.32	-0.48	-0.22	-0.35	-0.4	-0.2	-0.3

Table 4.2 shows the regional averages (over the dashed boxes in Figure 4.1) of modelled radiative forcing by dust, along with the effects on near-surface air temperature, surface

sensible and latent heat fluxes, near-surface specific humidity and near-surface wind speed at 0400 UTC on 22 and 23 September 2009 (analysis discussed in this section is only for the YSU-Noah scheme). Dust aerosols induced a reduction in shortwave radiation reaching the surface, air temperature at 2 metres, surface sensible and latent heat fluxes and wind speed at 10 metres. It is evident that changes in regional mean surface latent heat flux are larger outside the source area of dust on 23 September than over the desert regions on 22 September 2009. On a regional mean basis, near-surface specific humidity increased over the desert areas on 22 September (0.06 g kg^{-1}), but decreased outside the source area of dust on 23 September 2009 (-0.07 g kg^{-1}).

4.5 Sensitivity to PBL Parameterization and LSM

Within the WRF simulation, the choice of PBL parameterization plays a crucial role in regard to transport of energy, momentum, mass and moisture, while the LSM is important in determining soil moisture content, both of which may lead to differences in terms of dust entrainment, its radiative forcing and subsequent feedback effects on atmospheric characteristics. The YSU PBL scheme is a non-local closure model (taking into account non-local turbulent fluxes associated with large-scale eddies) with a counter-gradient term in the eddy-diffusion equation, and defines the PBL height as the height at which a critical Richardson number (Ri_{cr}) reaches a constant value of 0.25 over land, but a modified value over ocean as (*Hong*, 2010):

$$Ri_{cr} = 0.16\ (10^{-7} Ro)^{-0.18} \tag{4.3}$$

where Rossby number (Ro) is defined according to:

$$Ro = \frac{U_{10}}{f_0 z_0} \tag{4.4}$$

where U_{10} is the wind speed at 10 metres, f_0 the Coriolis parameter, and z_0 the surface roughness length. The MYJ PBL scheme is a local 2.5-level closure model, estimating

turbulent fluxes at each grid point based on atmospheric variables and their gradients at that point (*Hu et al.*, 2010). It is a turbulent kinetic energy (TKE)-based scheme and defines the PBL height at which 2×TKE first decreases to a minimum value of 0.2.

Model results for three different model runs (YSU-Noah, YSU-RUC and MYJ-Noah) when radiative forcing by dust is turned on are evaluated, as shown in Figure 4.9. Diurnal variation of air temperature at 2 metres over Bringelly (33.56°S, 150.45°E) and Alphington (37.46°S, 145.1°E) stations for the period 20-26 September 2009 is quite well simulated by the YSU-Noah and MYJ-Noah schemes (Figures 4.9a and 4.9b). The maximum temperatures simulated by the YSU-RUC scheme are higher than those simulated by the YSU-Noah and MYJ-Noah schemes. As a result, simulation with the YSU-RUC scheme generally overestimated the maximum air temperature (the convective unstable conditions), while the two simulations with the YSU-Noah and MYJ-Noah schemes better captured the observed temperatures. All three schemes overestimated near-surface wind speeds for both stations, with the largest positive bias in the simulation using the MYJ-Noah scheme for Bringelly station, while the YSU-Noah and YSU-RUC schemes showed better agreement with observed wind speeds over this region (Figures 4.9c and 4.9d). Comparison of observed PM_{10} concentrations over Brisbane (27.48°S, 153.03°E) and Toowoomba (27.55°S, 152.0°E) air quality monitoring sites with the simulations using the three different schemes is given in Figures 4.9e and 4.9f. A rapid increase of PM_{10} concentrations on 23 September is found in all three model simulations and the observations, although the model simulations predicted the dust arrival 2 hours before it was observed. The YSU-RUC scheme predicted higher PM_{10} concentrations than the YSU-Noah and MYJ-Noah schemes. As a result, the YSU-RUC scheme better simulated the maximum observed PM_{10} concentrations, but produced a larger overestimation during the rapid reduction in the observed dust following the peak. The overestimation of dust concentrations for all sets of simulations, when dust was actually settling back to the surface or being transported from the region, suggests that either dust deposition or transport processes were not well simulated or the source areas of dust were predicted to supply dust for a longer period of time than really occurred.

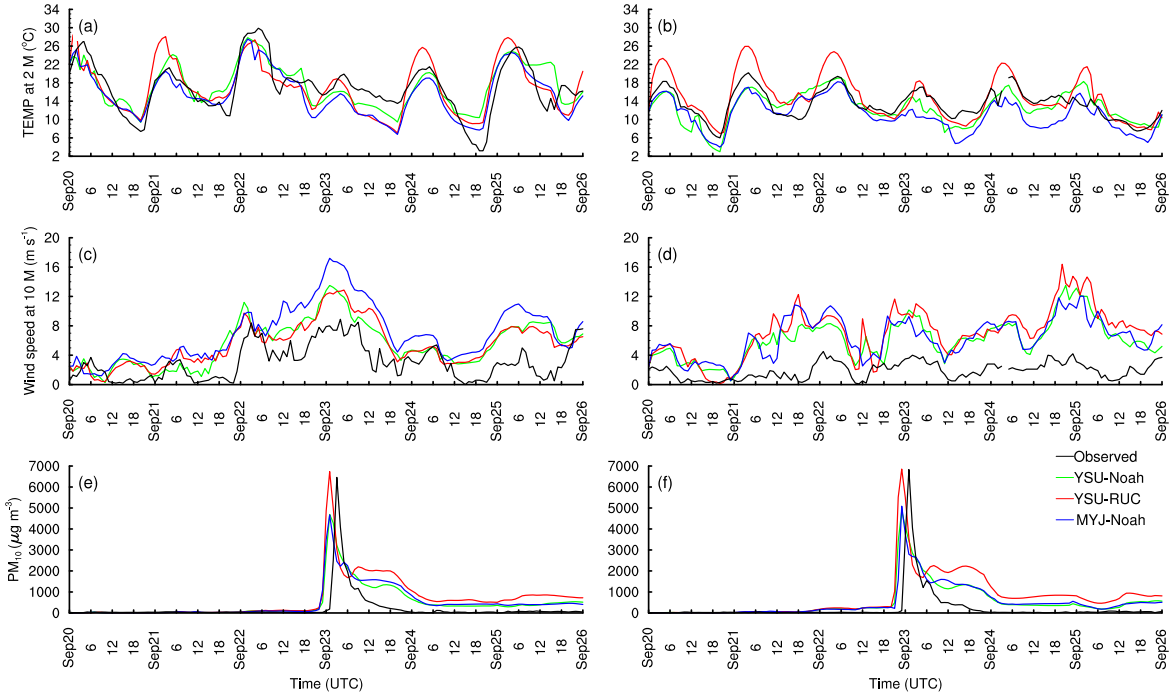

Figure 4.9. Simulated and observed air temperature at 2 metres (°C) for a) Bringelly (33.56°S, 150.45°E) and b) Alphington (37.46°S, 145.1°E) stations, wind speed at 10 metres (m s^{-1}) for c) Bringelly and d) Alphington stations, as well as PM_{10} concentrations (μg m^{-3}) for d) Brisbane (27.48°S, 153.03°E) and f) Toowoomba (27.55°S, 152.0°E) air quality monitoring sites.

Cross-sectional analysis of PM_{10} concentrations both over the source and outside the source area of dust reveals that in the YSU-RUC scheme the simulated dust load substantially increased compared to the YSU-Noah scheme (not shown). In contrast, use of the MYJ-Noah scheme was associated with a substantial reduction in dust load both in its magnitude and its vertical transport compared to the YSU-Noah and YSU-RUC schemes (not shown). As a result of increased dust-laden air, cooling in the lower layers of the boundary layer and warming in the upper boundary layer and lower free atmosphere are more pronounced in the simulation using the YSU-RUC scheme, and its pattern is very similar to temperature anomalies simulated by the YSU-Noah scheme (compare Figure 4.4a and Figure 4.10a). A reduced dust load for the MYJ-Noah scheme, on the other hand, resulted in a decrease of both cooling in the lower atmosphere and warming within the layers aloft (compare Figure 4.4a and Figure 4.10b). Another possible explanation for smaller dust radiative effects in simulations with the MYJ-Noah scheme is that the local MYJ scheme lacks sufficient vertical mixing (*Brown*, 1996) and has weaker entrain-

ment at the boundary-layer top (*Hu et al.*, 2010) compared to the non-local YSU scheme. Weaker vertical mixing transfers less dust from the surface to higher layers, while less entrainment at the boundary-layer top causes less dust to be advected from the boundary layer to the free atmosphere. Consequently, dust aerosols would remain mostly within the boundary layer for the MYJ-Noah scheme (not shown), and the low-level dust was shown have weaker radiative feedback effects (*Chung and Zhang*, 2004).

The simulated boundary-layer depth is relatively similar for the YSU-Noah and YSU-RUC schemes, but they differ substantially from the MYJ-Noah scheme. This is because the YSU scheme determines the boundary-layer depth using the critical Richardson number, while the MYJ scheme calculates the boundary-layer depth based on a TKE profile. As discussed earlier, the surface cooling and warming of the boundary-layer top by mineral dust was associated with a general decrease in boundary-layer depth. However, such a reduction is more significant in the YSU-RUC scheme (compare Figure 4.4a and Figure 4.10a), primarily because the surface cooling and warming of the boundary-layer top were more significant in the YSU-RUC scheme. Similar to changes in the vertical profile of temperature, the response of wind speed to radiative forcing by mineral dust using the YSU-RUC scheme is quite similar to the YSU-Noah scheme discussed in Section 4.2, with an overall decrease of wind speed in the lower boundary layer and its increase at the boundary-layer top and in the lower free atmosphere. However, the wind speed response to dust radiative effects is more significant in the YSU-RUC scheme. The MYJ-Noah scheme shows both a decrease and an increase of wind speed within the lower boundary layer and, at the same time, an increase at the boundary-layer top (Figure 4.10b). An overall increase in wind speed at the boundary-layer top is similar to the simulation results using the YSU scheme. However, wind speed decreased within the lower free atmosphere for the MYJ-Noah scheme, which is different to the results obtained for the YSU scheme.

Sensitivity of dust feedback effects to PBL parameterization and the LSM is evident in Table 4.2. The largest reduction of incident solar radiation reaching the ground surface is for the YSU-RUC scheme (with the anomaly value of -245 W m^{-2} on 22 September),

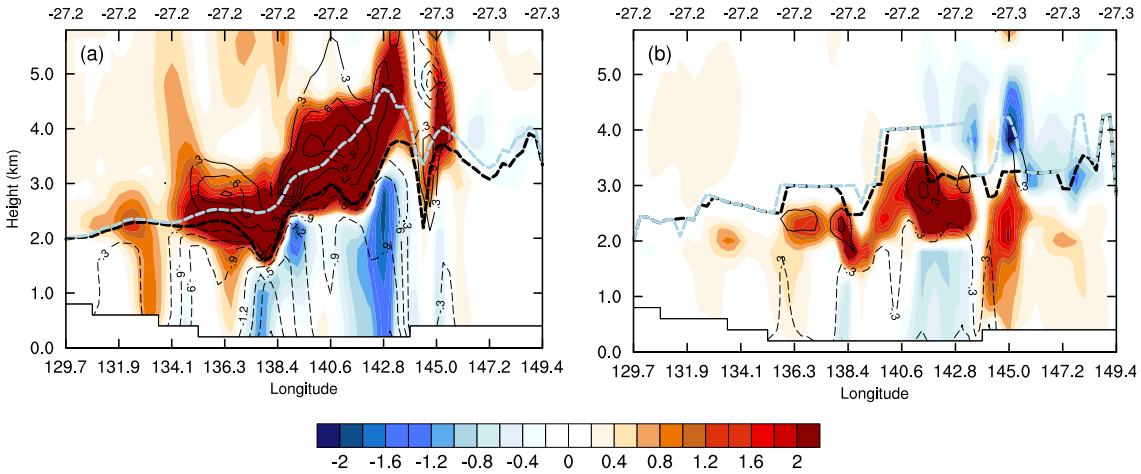

Figure 4.10. Vertical cross-sections (from A to B in Figure 3.1a of air temperature (contour interval of 0.3°C) and horizontal wind speed (colours, m s^{-1}) anomalies due to mineral dust radiative forcing at 0400 UTC on 22 September using a) the YSU-RUC and b) the MYJ-Noah schemes. The thick dashed black and blue lines indicate the boundary-layer depth diagnosed by the model when radiative forcing by dust is on and off, respectively. The top X axis is latitude.

leading to the most significant reduction of surface temperature (−3.7°C), surface sensible heat flux (-151.5 W m^{-2}), and wind speed at 10 metres (-0.48 m s^{-1}). This is expected because simulation with the YSU-RUC scheme predicted the highest dust load. In contrast, lower particle concentrations for the MYJ-Noah scheme resulted in the weaker dust feedback effects on atmospheric characteristics, both over the dust source areas and downwind regions (see Table 4.2).

4.6 Conclusions

Shortwave direct radiative forcing by mineral dust aerosols over Australia and sensitivity of such forcing to the PBL parameterization and LSM has been investigated using the WRF/Chem regional model. A near-surface temperature decrease of up to −3°C was simulated over regions with high dust load. The simulated values compare well with the effects of other major dust events that have occurred elsewhere. For example, *Mallet et al.* (2009) estimated a near-surface temperature forcing up to −4.5°C over North Africa during a dust event over the period 7-14 March 2006, with the refractive index of mineral

dust retrieved from the AErosol RObotic NETwork/PHOTONS (AERONET/PHOTONS) radiometers measurements based on the study of *Dubovik and King* (2000). The greater surface cooling effect over North Africa is due to higher dust emissions compared to those in Australia. It is also believed that African dust aerosols are frequently advected to significantly higher levels (*Liu et al.*, 2008) relative to Australia where dust aerosols have been shown to be transported mainly within the atmospheric boundary layer (*Alizadeh Choobari et al.*, 2012a). Different dust optical properties and surface albedos can also be an explanation for the differences.

By backscattering and absorbing solar radiation, dust aerosols decreased heat and moisture exchanges between the land surface and atmosphere, and ultimately reduced air temperature between the surface and near the top of the boundary layer. The air temperature reduction is weakened with altitude as the largest reduction of shortwave radiation occurred at the surface, similar to the results of *Yue et al.* (2010). At the boundary-layer top and in the lower free atmosphere, on the other hand, absorption of shortwave radiation by dust increased the air temperature. The simulated cooling at the surface and heating within the upper boundary layer and lower free atmosphere stabilize the atmosphere, resulted in a decreased boundary-layer depth. The surface cooling was also found to be associated with an increase of MSLP which is expected to induce subsidence, and may lead to an increase of dust removal through surface dry deposition, thereby reducing the lifetime of dust aerosols in the free atmosphere.

Despite substantial reductions in incident solar radiation reaching the ground associated with radiative forcing by dust, only a minor reduction of surface latent heat flux is simulated over the dust source area (Figure 4.5). This is expected because the majority of the land surface over the region is covered by desert, where surface latent heat flux is limited by a lack of soil moisture. Consequently, reduction of incoming shortwave radiation is mainly balanced by a reduction of surface sensible heat flux. Outside the dust source regions, on the other hand, the increased soil moisture content increased the sensitivity of surface latent heat flux to radiative forcing by dust.

Simulation results suggest that in some areas, cloud fraction was reduced due to evaporation of clouds associated with absorption of radiation by dust aerosols embedded within them. This resulted in an increase of shortwave radiation reaching the surface and hence an increase of near-surface air temperature and surface heat fluxes. This is consistent with previous studies that identified localized dissipation of clouds by dust and subsequent positive surface radiative forcing (*Huang et al.*, 2006; *Mallet et al.*, 2009; *Yue et al.*, 2010). As a result, simulation results suggest that dust-laden air over Australia can locally inhibit cloud formation. This dust effect on cloud fraction can lead to a local warming effect, but at a regional scale the dust cooling effect is still dominant, thereby offsetting the warming effect associated with greenhouse gases.

The increased stability of the atmosphere related to changes in the vertical temperature profile reduced the vertical exchange of horizontal momentum, leading to an overall decrease in near-surface wind speeds. In contrast, wind speeds were predicted to increase within the upper boundary layer and lower free atmosphere. In some regions, the localized surface warming effect associated with reduction of cloud fraction resulted in the increased wind speed propagating downwards from the boundary-layer top towards the surface. Furthermore, occasionally, when wind speeds were stronger in the boundary layer relative to the lower free atmosphere, the impact of dust on surface cooling and warming aloft contributed to positive and negative wind speed anomalies within the lower and upper boundary layer, respectively. The pattern of near-surface wind speed perturbation generated here is different from the results of *Miller et al.* (2004b), who identified only the reduction of near-surface wind speeds by dust aerosols, but is similar to the results of *Heinold et al.* (2007) and *Yue et al.* (2010).

The effect of dust aerosols on airflow has been identified elsewhere. For example, an increase of the northerly branch of the African Easterly Jet was noted by *Lau et al.* (2009) during Saharan dust events over West Africa, while *Tummon et al.* (2010) identified an increase of the southern branch of the African Easterly circulation due to biomass burning in southern Africa. Our results over Australia, however, indicate different radiative feedback effects on wind speeds in the lower and upper boundary layer, with the weak-

ening of southwesterly flows within the lower boundary layer and strengthening of the westerly flows at the boundary-layer top and in the lower free atmosphere. Consequently, over Australia, postfrontal southwesterly winds tend to generate dust suspension in the atmosphere (*Alizadeh Choobari et al.*, 2012a), but the dust may also in turn lead to a weakening of the near-surface southwesterly winds.

Dust radiative effects are sensitive to both PBL parameterization and the LSM selected. In general, simulated dust concentrations were higher using the YSU scheme (both for the Noah and RUC LSMs) than the MYJ scheme. As a result, although both the YSU and MYJ schemes showed similar cooling effects associated with radiative forcing by dust extending from the surface to near the boundary-layer top, the cooling effect was significantly higher when using the YSU scheme. Furthermore, simulations performed by the YSU scheme produced substantial warming effects of dust within the upper boundary layer and lower free atmosphere, while a slight warming effect only within the upper boundary layer was simulated by the MYJ scheme. Therefore, the YSU scheme (especially YSU-RUC) simulated a greater decrease in boundary-layer depth associated with the dust radiative effects. In addition, the dust feedback effects on the vertical profile of wind speeds using the YSU scheme were different from those simulated by the MYJ scheme. For example, overall wind speeds increased in the lower free atmosphere for the YSU scheme, whereas a negative feedback effect on wind speeds was predicted within the lower free atmosphere in the MYJ scheme. As MYJ is a local closure scheme, it produces less mixing in the convective boundary layer (*Brown*, 1996), and hence transfers less dust from the surface to the boundary-layer top. This effect combined with less entrainment of dust to the free atmosphere at the boundary-layer top results in less elevated dust with the simulation using the MYJ scheme compared to the YSU scheme. The lower-level dust layer predicted in the simulation performed using the MYJ scheme contributed to a decrease in the radiative surface cooling effect of the dust, so that this scheme simulated weaker dust feedback effects on vertical profiles of temperature and wind speed than those simulated using the YSU scheme. Relative similarity between dust radiative effects in simulations with the same PBL scheme (YSU-Noah and YSU-RUC) implies

that the differences in radiative forcing by dust between different schemes mainly arise from the PBL schemes themselves rather than differences in the LSMs.

Overall, analysis of the WRF/Chem simulation results highlights the importance of radiative forcing by mineral dust for the regional climate of Australia. This study provides an evaluation of not only direct forcing of mineral dust, but also its sensitivity to boundary-layer and land-surface schemes. Previous studies have mainly emphasized the importance of real and imaginary parts of the refractive index of mineral dust and its size to estimate the radiative forcing by mineral dust. Our results indicate that the choice of PBL and LSM schemes also plays a significant role in model-based assessment of such forcing. This study only examined the shortwave radiative forcing by mineral dust over Australia during a severe dust event. To better understand the climate impact of mineral dust over the region, we plan to conduct long-term multi-month simulations that include both shortwave and longwave radiative effects of dust. Further research will examine the sensitivity of the WRF/Chem model to a wider range of parameterization schemes, including the Mellor-Yamada-Nakanishi-Niino scheme (*Nakanishi and Niino*, 2004), so that the most appropriate options can be identified.

Chapter 5

Direct Radiative Forcing by Dust over Australia

Alizadeh Choobari, O., P. Zawar-Reza and A. Sturman (2013), Simulation of the spatial distribution of mineral dust and its direct radiative forcing over Australia. ***Tellus B, 65*****, 19856, doi:10.3402/tellusb.v65i0.19856.**

Abstract. Direct radiative forcing by mineral dust is important as it Direct radiative forcing by mineral dust is important as it significantly affects the climate system by scattering and absorbing shortwave and longwave radiation. The Multi-angle Imaging SpectroRadiometer (MISR) and Cloud-Aerosol Lidar with Orthogonal Polarization (CALIOP) aerosol data are used to observe mineral dust distribution over Australia. Additionally, the Weather Research and Forecasting with Chemistry (WRF/Chem) model is used to estimate direct radiative forcing by dust. At the surface, the model domain clear-sky shortwave and longwave direct radiative forcing by dust averaged for a 6-month period (austral spring and summer) was estimated to be -0.67 W m^{-2} and 0.13 W m^{-2}, respectively. The longwave warming effect of dust therefore offsets 19.4% of its shortwave cooling effect. However, over Lake Eyre Basin where coarse particles are more abundant, the longwave warming effect of dust offsets 60.9% of the shortwave cooling effect. At the top of the atmosphere (TOA), clear-sky shortwave and longwave direct radiative forcing was estimated to be -0.26 W m^{-2} and -0.01 W m^{-2}, respectively. This leads to a net negative direct radiative forcing of dust at the TOA, indicating cooling of the atmosphere by an increase in outgoing radiation. Shortwave and longwave direct radiative forcing by dust is shown to have a diurnal variation due to changes in solar zenith angle and in the intensity of infrared radiation. Atmospheric heating due to absorption of shortwave radiation was simulated, while the interaction of dust with longwave radiation was associated with atmospheric cooling. The net effect was cooling of the atmosphere near the surface (below 0.2 km), with warming of the atmosphere at higher altitudes.

5.1 Introduction

Mineral dust aerosols contribute more than half of the total global aerosol burden (*Textor et al.*, 2006) and have a significant influence on the climate system directly through scattering and absorption of solar and infrared radiation (*McCormick and Ludwig*, 1967; *Miller and Tegen*, 1998), semi-directly through changes in atmospheric temperature structure and the evaporation rate of cloud droplets (i.e. the cloud burning effect; *Hansen et al.*, 1997; *Ackerman et al.*, 2000; *Koren et al.*, 2004), and indirectly in a complex way through impact on optical properties of clouds (i.e. the cloud burning effect; *Gunn and Phillips*, 1957; *Liou and Ou*, 1989) and suppression (*Ferek et al.*, 2000; *Rosenfeld*, 2000) or enhancement (*Andreae et al.*, 2004) of precipitation formation. The direct radiative effect of dust has been investigated extensively using general circulation models (e.g. *Tegen et al.*, 1996) and more recently by applying regional and global models which incorporate a more physically-based dust emission scheme (e.g. *Darmenova et al.*, 2009; *Zhao et al.*, 2010; *Huneeus et al.*, 2011). These studies highlight the cooling effect of dust aerosols near the surface due to backscattering and absorption of shortwave radiation, and heating of the atmosphere above due to absorption of both shortwave and longwave radiation (*Alizadeh Choobari et al.*, 2012b, 2013a).

Australia is the major source of mineral dust in the Southern Hemisphere (*Prospero et al.*, 2002), with an estimated annual emission of 100 Tg (*Mitchell et al.*, 2010). It is believed that there will be drier conditions over most of Australia in response to future climate change (*McCarthy et al.*, 2001), leading to an increase in its natural dust emission (*Tegen et al.*, 2004). As such there is a critical need to understand optical properties of dust aerosols in this region. Yet, climate impacts of Australian dust remain largely unknown, partly because until recently aerosol processes have been treated independent from meteorology (*Grell et al.*, 2005), but also because unlike the major Northern Hemisphere sources of dust such as the Sahara, Australian dust appears not to be important in modifying climate on a global scale, as it is believed that it only accounts for about 5% of the global total dust emission (*Mitchell et al.*, 2010). However, mineral dust from Australia is

an important component of the atmosphere that affects regional climate through radiative impacts. A number of factors have improved our ability to better monitor dust aerosol distribution and understand its radiative properties over Australia. These include the rapid development of online and coupled aerosol-atmosphere models (*Grell et al.*, 2005), as well as the advent of satellites with the ability to measure mineral dust aerosols over bright land surfaces (*Kahn et al.*, 2005) and to identify their vertical distribution (*Leon et al.*, 2003). Recent field campaigns for identifying mineral composition of Australian dust (e.g *Qin and Mitchell*, 2009; *Radhi et al.*, 2010) have also contributed.

Lake Eyre Basin of central eastern Australia is the most important source of mineral dust in the Southern Hemisphere, with an average of 82 dusty days per year (*Bullard and McTainsh*, 2003). Dust storms in the basin occur throughout the year, but they are more frequent during spring (SON) and summer (DJF) (*Ekstrom et al.*, 2004). Dust emission within the basin is often associated with the passage of dry cold fronts (*Ekstrom et al.*, 2004; *Alizadeh Choobari et al.*, 2012a) in spring and summer. Note that, although passage of cold frontal systems across central Australia is more frequent during winter, the winter fronts are often associated with precipitation, thereby reducing the potential for dust entrainment (*Ekstrom et al.*, 2004). Mineral dust can be transported long distances to southeastern Australia in association with the eastward propagating frontal systems, reaching as far as New Zealand and beyond. It can also be transported to northern tropical Australia by postfrontal southerly winds, and subsequently to northwestern Australia and the Indian Ocean by southeasterly trade winds (*Alizadeh Choobari et al.*, 2012a).

Australian dust particle size and color is different from the Northern Hemisphere "dust belt" (*Kiefert et al.*, 1996; *Qin and Mitchell*, 2009; *Radhi et al.*, 2010). For example, a greater fraction of larger particles has been found for Australian dust compared to African dust (*Kiefert et al.*, 1996), suggesting that the optical properties of dust from Australia are different from the Sahara. Observations over Australia for identifying optical properties of mineral dust are rare, but a few field campaigns have been conducted over recent years. Using a cluster analysis of AErosol RObotic NETwork (AERONET) retrievals, *Qin and Mitchell* (2009) identified strong absorption of radiation by Australian dust compared

to the "dust belt" of the Northern Hemisphere. By conducting a field experiment, *Radhi et al.* (2010) investigated optical, physical and chemical characteristics of Australian dust. Their mineralogical analysis indicates that the iron content of Australian dust is higher than other major sources of dust in the Northern Hemisphere, similar to the results of *Qin and Mitchell* (2009). The results of these earlier studies have been used to set the refractive index of Australian dust for shortwave radiation.

To our knowledge, there have been few modelling studies that have investigated radiative forcing by mineral dust aerosols over Australia. Using the CSIRO (the Commonwealth Scientific and Industrial Research Organisation) global climate model, *Rotstayn et al.* (2010) showed that inclusion of radiative forcing by dust leads to better simulation of the spatial distribution of El Niño Southern Oscillation (ENSO) rainfall over Australia. *Rotstayn et al.* (2011) found that radiative forcing by mineral dust reduces precipitation over Australia in dry El Niño years, but increases it in wet La Niña years. Although these studies have provided an insight into the dust-induced changes of precipitation over Australia, estimates of the direct radiative effect of Australian dust are scarce. By investigating shortwave direct radiative forcing of Australian mineral dust, *Alizadeh Choobari et al.* (2012b) found that suspended dust modifies the boundary layer profile and stabilizes the lower atmosphere, leading to an overall reduction of wind speed near the surface, and its increase within the upper boundary layer and lower free atmosphere. However, this earlier study focused on an individual severe dust event during September 2009, leaving long-term effects of Australian dust radiative forcing still an open question. Furthermore, the direct effect of dust aerosols in the thermal infrared range over Australia remains unexplored.

This study therefore aims to improve understanding of the direct radiative effect of mineral dust over Australia by using the Weather Research and Forecasting with Chemistry (WRF/Chem) regional model. The objective of the study is two-fold: (1) to observe and simulate monthly variation of mineral dust over Australia during the drought period of austral spring and summer when dust outbreaks over central eastern Australia are most frequent; and (2) to simulate shortwave and longwave direct radiative forcing of mineral

dust at the surface and top of the atmosphere (TOA) over the region. While long-term averaged observation data were used to investigate monthly to seasonal variation of mineral dust distribution over the region, due to computational constraints model simulations were only conducted from September 2009 to the end of February 2010 during a dry El Niño year when dust outbreaks over central eastern Australia were significant.

The chapter is organized as follows. Sections 5.2 and 5.3 describe observations and the model set up used in this study. Monthly variation of mineral dust distribution, as observed by satellites and simulated by the WRF/Chem model, is discussed in Section 5.4. Simulated shortwave and longwave direct radiative forcing of mineral dust is the subject of Section 5.5. The atmospheric heating and cooling rates due to the interaction of mineral dust aerosols with shortwave and longwave radiation are discussed in Section 5.6, while Section 5.7 presents a discussion and an overall conclusion.

5.2 Observations

5.2.1 MISR

The Multi-angle Imaging SpectroRadiometer (MISR) instrument on board the sun-synchronized polar orbiting NASA Terra satellite has been used to measure aerosol optical depth (AOD) since February 2000. The MISR cloud/plume fraction and height product has a vertical resolution of 500 m. MISR observes at nine distinct zenith angles ranging from 70° aftward to 70° forward in four spectral bands centred at 446, 558, 672, and 866 nm. As a result, MISR can retrieve aerosol properties over both land and ocean including highly reflective land surfaces such as deserts (*Martonchik et al.*, 2004). The data used here are available daily and monthly AOD at 0.55 μm wavelength at a 0.5° × 0.5° horizontal resolution retrieved from the MISR satellite instrument for the Australian region.

5.2.2 CALIOP

The Cloud-Aerosol Lidar with Orthogonal Polarization (CALIOP) was launched on board the Cloud-Aerosol Lidar and Infrared Pathfinder Satellite Observations (CALIPSO) spacecraft in April 2006 (*Winker et al.*, 2007). CALIPSO is a sun-synchronized polar orbiting satellite which orbits the globe about 15 times per day, providing both day and night measurements. The data utilized here are dust extinction coefficients at 0.532 μm available from the CALIOP Level 3 aerosol profile monthly products with a horizontal resolution of 2° × 5° (latitude/longitude) and a vertical resolution of 60 m, and both daytime and nighttime CALIOP data are taken into consideration. A constant lidar ratio value of 40 sr at 0.532 μm is used in the CALIOP algorithm to retrieve mineral dust, which is lower than the lidar ratio of 55 ± 10 sr obtained from ground-based lidar observations. Furthermore, multiple scattering is ignored in the CALIOP retrievals (*Wandinger et al.*, 2010). Cloud-aerosol discrimination (CAD), an indicator to discriminate between clouds (positive CAD) and aerosols (negative CAD), is used to exclude extinction caused by clouds. Only aerosol layers having CAD scores between -100 and -20 are used in the CALIOP algorithm because layers with CAD scores between 20 and -20 are often the result of erroneous layer detection triggered by noise.

5.3 Model Description

The WRF/Chem regional model was applied to simulate mineral dust distribution and its optical properties over Australia. WRF is a nonhydrostatic, primitive equation model using terrain following coordinates (*Janjic*, 2003) that has been coupled with a chemistry module to integrate atmospheric chemistry and aerosols with the meteorological model (*Grell et al.*, 2005). As a result, the influence of meteorology on aerosol diffusion, transport and deposition, and the influence of aerosols on the state of the atmosphere are both considered.

The GOCART (Goddard Global Ozone Chemistry Aerosol Radiation and Transport) sim-

ple aerosol scheme was used, as this study only focuses on the simulation of dust particles. The GOCART dust scheme considers preferential sources based on erodible fraction (*Cavazos Guerra*, 2011) and calculates the vertical dust flux from the surface as (*Ginoux et al.*, 2001, 2004):

$$F = CS\, s_p u_{10}^2\, (u_{10} - u_{tp}) \qquad for \;\; u_{10} \geq u_{tp} \tag{5.1}$$

where C is an empirical proportionality constant and tuned to 1.9 μg s^2 m^{-5}, u_{10} is the horizontal wind speed at 10 m, u_{tp} is the threshold velocity for wind erosion of particle size p, below which there is no dust emission, s_p is the fraction of each size class of dust, and S is the fraction of sediments accumulated in the topographic depression regions having bare surfaces that are available for wind erosion (*Chin et al.*, 2003). The threshold velocity is believed to be the major source of uncertainty for dust emission (*Ginoux et al.*, 2012). It depends on surface properties and is a function of particle size, air and particle density, and the bonding effect of soil moisture. Dust particles can be blown into the atmosphere when wind speed at 10 m (u_{10}) exceeds the threshold velocity for a given particle size and density (u_{tp}) and surface wetness is smaller than the threshold value of 0.5. Surface wetness is taken into consideration because soil moisture increases the cohesion forces between soil particles (*Tegen*, 2003). Five discrete size bins of dust particles were considered, with idealized spherical shapes whose radii range from 0.1 to 10 μm. The five dust bins in the model are 0.1-1, 1-2, 2-3, 3-6 and 6-10 μm, with corresponding effective radii of 0.73, 1.4, 2.4, 4.5 and 8.0 μm. Consequently, direct radiative forcing of dust particles greater than 10 μm in radius is not considered in the current study. This implies that the radiative effect of dust may be underestimated over and near the source of dust where coarse particles are more abundant. The bin scheme adopted in this study is more realistic than the modal aerosol scheme that assumes that the shape of the size distribution does not change during transport (*Tegen*, 2003).

Dust particles can be transported by advection and eddy diffusion, while dry and wet deposition are removal processes. Dry deposition includes gravitational settling as a function

of particle size and air viscosity, and surface deposition as a function of surface type and atmospheric stability conditions (*Wesely*, 1989). The wet deposition scheme considers stratiform and convective precipitation (*Balkanski et al.*, 1993).

The Yonsei University (YSU) planetary boundary layer (PBL) parameterization (*Hong et al.*, 2006; *Hong*, 2010), the Noah land-surface model (*Chen and Dudhia*, 2001; *Ek et al.*, 2003) and the Monin-Obukhov surface layer scheme (*Obukhov*, 1971) were used in the simulation. The Morrison (*Morrison et al.*, 2009) and Grell 3D (*Grell*, 1993) schemes were used to represent cloud microphysics and convection processes. The rapid radiative transfer model for general circulation models (RRTMG) (*Mlawer et al.*, 1997) was used for both shortwave and longwave radiation to include the direct radiative effect of aerosols, while the indirect effects of mineral dust were not investigated in this study. The refractive index was calculated by volume averaging for each size bin, and Mie theory was used to estimate the extinction efficiency, the scattering efficiency and the asymmetry factor. Optical properties were then calculated by summation over all size bins. The refractive index of mineral dust for shortwave radiation was considered to be wavelength independent and its real part was set to 1.58, following the work of *Qin and Mitchell* (2009) over Australia. The imaginary part is uncertain and values ranging from 0.0004i to 0.006i have been suggested (e.g. *Dubovik et al.*, 2002). The value of 0.003i was used by *Zhao et al.* (2010) over the Sahara. However, *Radhi et al.* (2010)'s study indicates that Australian dust is rich in iron, with the iron content identified to be around 1.8 times larger than the Saharan dust. Accordingly, the imaginary part of the refractive index for shortwave radiation was considered to be 1.8 times greater than the value obtained over the Sahara, and set to 0.0054i. Due to insufficient information to constrain the refractive index of mineral dust for longwave radiation, the default setting of the WRF/Chem model was used, with the real and imaginary parts considered to be wavelength dependent and to vary for 16 longwave spectral bands (table 5.1).

The model domain covers Australia and New Zealand using 335×250 grid points at 20 km horizontal resolution, with 27 vertical layers. Two simulations with and without dust were performed in a way that the two-way interaction between atmospheric processes and

Table 5.1. Refractive index of mineral dust for 16 longwave spectral bands used in the WRF/Chem model.

	Refractive index	
Longwave (μm)	real	imaginary
3.1-3.8	1.51	0.018
3.8-4.2	1.5	0.0068
4.2-4.4	1.5	0.008
4.4-4.8	1.495	0.011
4.8-5.6	1.473	0.0245
5.6-6.8	1.432	0.061
6.8-7.2	1.447	0.105
7.2-8.5	1.242	0.093
8.5-9.3	1.557	0.373
9.3-10.2	2.917	0.65
10.2-12.2	1.822	0.26
12.2-14.3	1.911	0.319
14.3-15.9	1.508	0.263
15.9-20.0	1.748	0.462
20.0-28.6	2.904	0.857
28.6-1000	2.340	0.7

aerosols was included in the simulations. Direct radiative forcing of dust was calculated from the differences between the results of the two simulations. The simulation covers the period from 1 September 2009 to 28 February 2010 (referred to as the simulation period). Meteorological initial and boundary conditions were obtained from the National Centers for Environmental Prediction (NCEP) Final Analysis (FNL) re-analysis data at 1 ° resolution. The simulation was conducted by re-initializing meteorological conditions every 10 days with the FNL re-analysis data and the boundary conditions were updated every 6 hours. The chemical boundary conditions are from the default profiles in the WRF/Chem model.

5.4 Observed and Simulated Dust

Figure 5.1 shows monthly mean AOD at 0.55 μm over Australia from September 2009 to February 2010 retrieved from the MISR satellite instrument. High AOD values reaching 0.4 are present over central eastern Australia in all months, with peak values in Novem-

ber, although dust storm activity decreased substantially during January and February. There is also high aerosol loading over the tropical regions of northern Australia from September 2009 to January 2010 due to extensive biomass burning over the region (*Edwards et al.*, 2006). The peak AOD due to biomass burning is in October, both over the tropical regions of northern Australia and Indonesia, with a pronounced decrease in February, reflecting rainfall increases associated with complete establishment of the Australian summer monsoon season. Note that generally biomass burning takes place during the August-September dry season over Indonesia, but its relatively high aerosol loading during October to December is due to the El Niño warm phase (*Edwards et al.*, 2006) which caused significant drying in 2009 (*Zhao and Running*, 2010). The maximum and minimum domain averaged (50 – 5°S and 110 – 180°E) monthly mean AOD during the observed period was estimated to occur in October with 0.19 and February with 0.133, respectively (Figure 5.1).

Available daily and monthly mean variation of AOD values over the Lake Eyre Basin region (26 – 29°S and 137 – 139°E) retrieved from the MISR satellite instrument for the period 2001 to 2011 is shown in Figure 5.2. It is clear that dust activity over the basin started to increase in September, reached a peak in January, and began to decrease in March. Seasonally averaged AOD values was obtained to be 0.197 and 0.194 during spring (SON) and summer (DJF), respectively. In contrast, dust activity was substantially reduced over the region during autumn (MAM) and winter (JJA), with AOD values of 0.109 and 0.086, respectively. The maximum and minimum dust storm activity occurred in January and June with monthly mean AOD values of 0.212 and 0.077, respectively.

Figure 5.3 shows dust extinction coefficient (attenuation of light passing through the atmosphere by dust aerosols) profiles at 0.532 μm over Lake Eyre Basin (28°S and 137.5°E) for September 2009 to February 2010 retrieved from CALIOP. Dust extinction coefficients generally decrease with altitude (except in October when there is a second peak value of 0.043 km^{-1} at around 1.2 km height) and the peak values are located close to the surface in all months, indicating that Australian dust aerosols are mostly transported in the lower at-

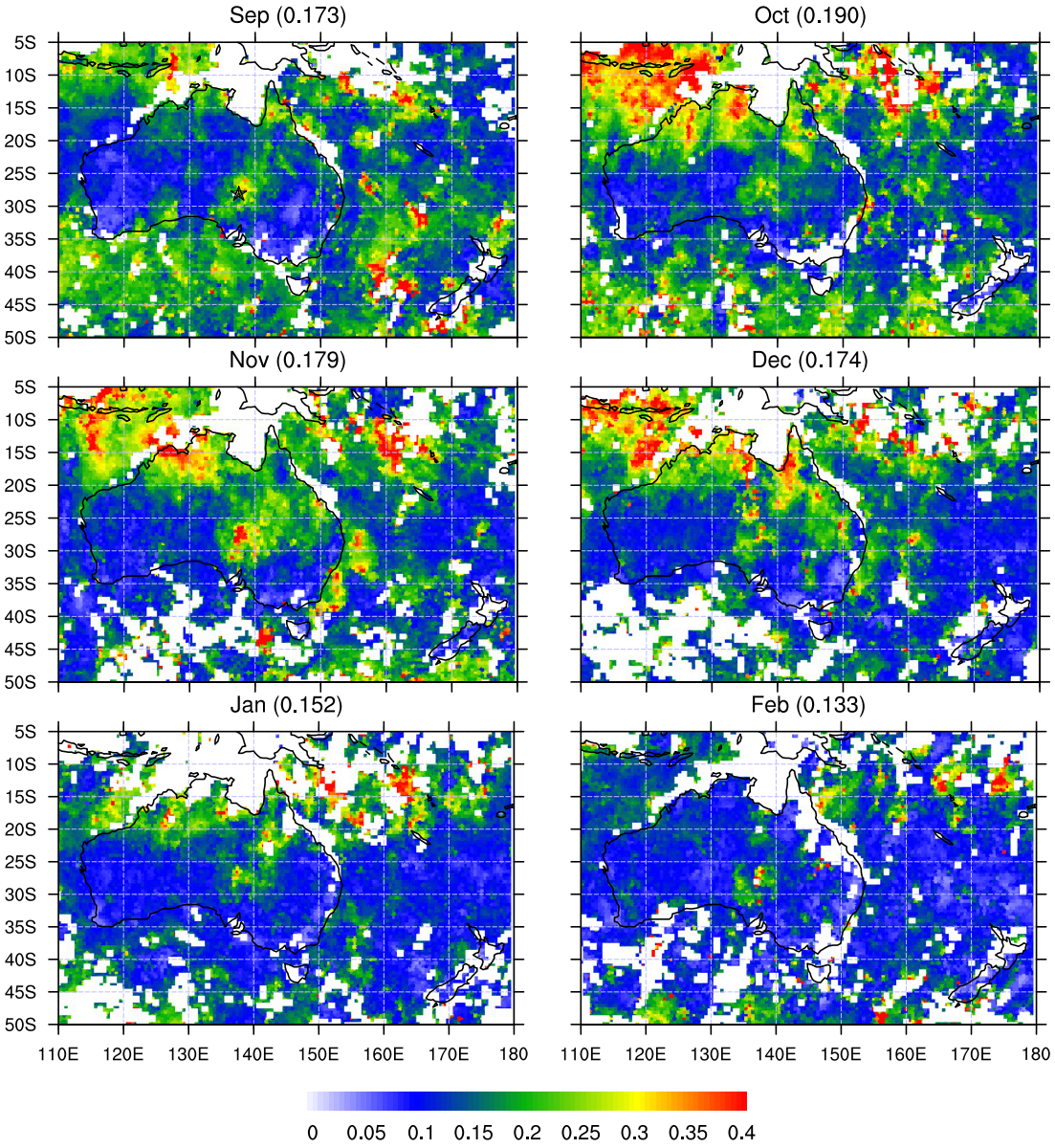

Figure 5.1. Aerosol optical depth (AOD) at 0.55 μm from September 2009 to February 2010 retrieved from the MISR instrument. Domain averaged (50 – 5°S and 110 – 180°E) monthly mean AOD is indicated in brackets for each panel. The location of Lake Eyre Basin is shown by the star.

mosphere and therefore expected to be mostly deposited near the dust source regions. The maximum dust extinction coefficients were observed in October 2009 and January 2010, with peak values reaching around 0.06 km^{-1} close to the surface. In contrast, the lowest dust extinction coefficient was observed in February 2010 when it reached a peak value of 0.017 km^{-1} near the surface. Seasonally averaged dust extinction coefficient profiles over

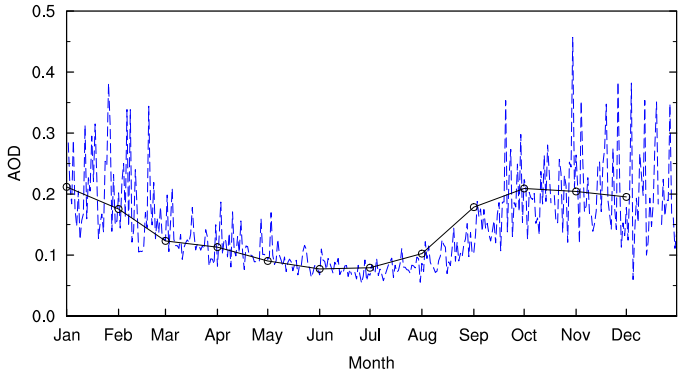

Figure 5.2. Daily (blue) and monthly mean (black) variation of AOD over Lake Eyre Basin (26 – 29°S and 137 – 139°E) retrieved from the MISR satellite instrument and averaged for the period 2001 to 2011.

Lake Eyre Basin from March 2009 to February 2010 are also compared in Figure 5.3g. Dust aerosols reach higher altitudes and have greater concentrations in spring than other seasons, with substantially reduced values in winter. However, the longer time (2006-2011) seasonally averaged dust extinction coefficient profiles (which provide typical dust profiles) indicate that dust activity is greater over Lake Eyre Basin during summer relative to spring (Figure 5.3h). This is in contrast to the results from long-term MISR data (2001-2011) that indicate slightly higher dust activity during spring.

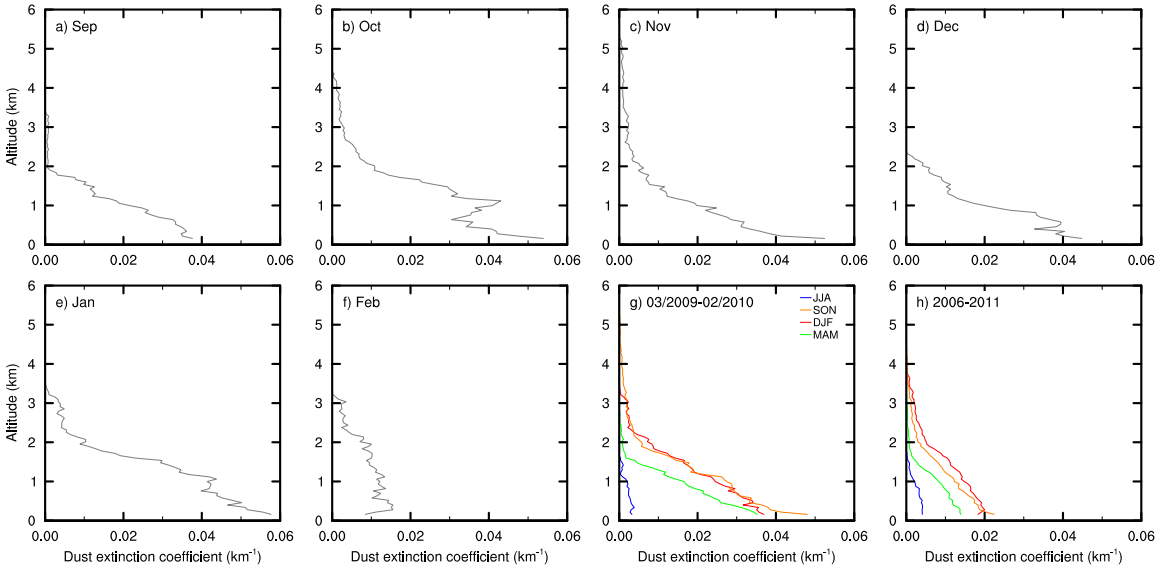

Figure 5.3. Dust extinction coefficient (km^{-1}) profiles at 0.532 μm from (a-f) September 2009 to February 2010, (g) in different seasons from March 2009 to February 2010 and (h) seasonally averaged for the 6-year period (2006-2011) over Lake Eyre Basin (28°S and 137.5°E), retrieved from CALIOP satellite lidar.

A dust aerosol layer extends from the surface to a height of around 4 km in spring and summer, which is higher than autumn and winter when the top of the dust layer reaches a height of around 2.5 km and 1.5 km, respectively (Figure 5.3h). This is due to the fact that more dust particles are entrained into the atmosphere during spring and summer (see Figure 5.2) and they can be carried to higher altitudes as a result of a deep mixed layer created by intense solar heating during warmer seasons. Note that Figure 5.3 indicates that seasonal mean aerosol extinction coefficients were significantly higher in 2009-2010 than the averaged values for the 6-year period from 2006 to 2011 (except for similar patterns in winter) as there was severe drought over the region during 2009 and early 2010 (*Zhao and Running*, 2010).

Monthly mean AOD over Lake Eyre Basin retrieved from the MISR and CALIOP instruments and the WRF/Chem model for September 2009 to February 2010 is shown in Figure 5.4. The MISR data show that the maximum and minimum AOD occurred in November 2009 (0.506) and January 2010 (0.204) respectively, while CALIOP data indicate that peaks occurred in October 2009 (0.057) and January 2010 (0.056), with minimum values observed in February 2010 (0.034). The maximum AOD in October and January retrieved from CALIOP was caused by large amounts of elevated dust compared to other months, while the minimum value in February is due to both less near-surface and elevated dust aerosols, as shown in Figure 5.3. Note that monthly mean AOD values from CALIOP are substantially less than those from MISR. The underestimation of AOD by CALIOP is due to the fact that a low lidar ratio is used in the CALIOP algorithm to retrieve mineral dust, multiple scattering is not taken into account in the CALIOP retrievals for dense dust layers (*Wandinger et al.*, 2010), and dense dust plumes can be misclassified as clouds (*Tsamalis and Chedin*, 2013). Furthermore, regions that are identified as clear air by the CALIOP feature finder are assumed to have an aerosol extinction coefficient of 0.0 km^{-1} in the CALIOP algorithm. Differences in the timing of maximum and minimum AOD values obtained from the MISR and CALIOP datasets are caused by differences between their sensors and their different spatial and temporal resolution (*Petrenko et al.*, 2012). Monthly mean simulated AOD values are greater than AOD values retrieved from

CALIOP, but less than those from MISR. The minimum AOD (0.084) is simulated in September and December 2009, while the maximum AOD (0.111) is predicted to be in January 2010. The WRF/Chem model simulated higher AOD during summer than spring, primarily due to drier land surfaces in summer.

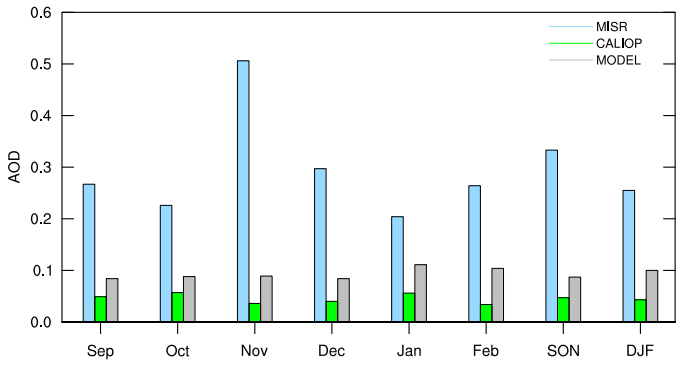

Figure 5.4. Monthly average AOD observed by the MISR and CALIOP satellite instruments and simulated by the WRF/Chem model over Lake Eyre Basin (28°S and 137.5°E) from September 2009 to February 2010.

Dust optical depth (DOD) at 0.55 μm over Australia averaged over the simulation period from September 2009 to February 2010 is shown in Figure 5.5. It clearly indicates that the most important source of dust is located over Lake Eyre Basin, with the averaged DOD reaching less than 0.2. Australian dust plumes are mostly carried through the northwestern corridor towards the Timor Sea and Indian Ocean. Transport of dust in a northward direction to tropical northern Australia and in an east to southeastward direction to the Coral and Tasman Seas and the Southern Ocean is also simulated by the model (Figure 5.5). It is also evident that dust from Lake Eyre Basin affects New Zealand during spring and summer.

5.5 Shortwave and Longwave Radiative Forcing by Dust

Figure 5.6 shows simulated clear-sky shortwave, longwave and net (shortwave + longwave) direct radiative forcing by mineral dust aerosols at the surface and TOA averaged for a 6-month period from September 2009 to February 2010. Shortwave radiative forcing is negative at the surface due to scattering and absorption of solar radiation by dust

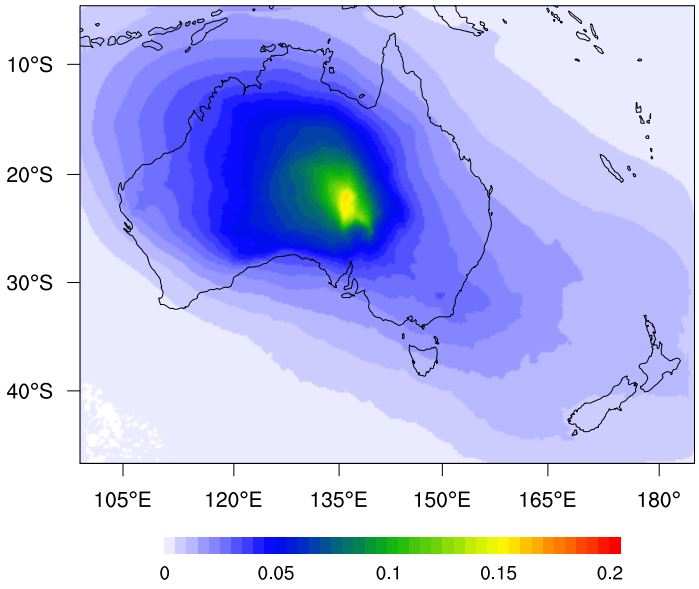

Figure 5.5. Simulated dust optical depth (DOD) at 0.55 μm averaged for a 6-month period from September 2009 to February 2010.

aerosols. Similarly, it is generally negative at the TOA, indicating an increase of outgoing shortwave radiation by dust aerosols. In contrast, mineral dust aerosols trap longwave radiation, thereby inducing positive longwave radiative forcing at the surface. At the TOA, both positive and negative longwave radiative forcing are simulated, and the domain averaged (over the entire domain shown in Figure 5.6) longwave radiative forcing is nearly zero. The net direct radiative forcing is negative at the surface as the shortwave cooling effect of dust outweighs the longwave warming effect. The net radiative forcing is also negative at the TOA, corresponding to a cooling of the atmosphere by an increase of outgoing radiation (increased reflection of radiation to space).

The domain averaged radiative forcing by mineral dust aerosols over the simulation period indicates that the longwave warming effect of dust (0.13 W m^{-2}) offsets 19.4% of its shortwave cooling effect (-0.67 W m^{-2}) at the surface (Figure 5.6). As a result, the net direct radiative forcing of dust has the negative value of -0.54 W m^{-2} at the surface because scattering and absorption of solar radiation dominates over the trapping of infrared radiation. Similarly, the net direct radiative forcing of mineral dust has a negative value of -0.27 W m^{-2} at the TOA. The difference between surface and TOA net radiative forcing

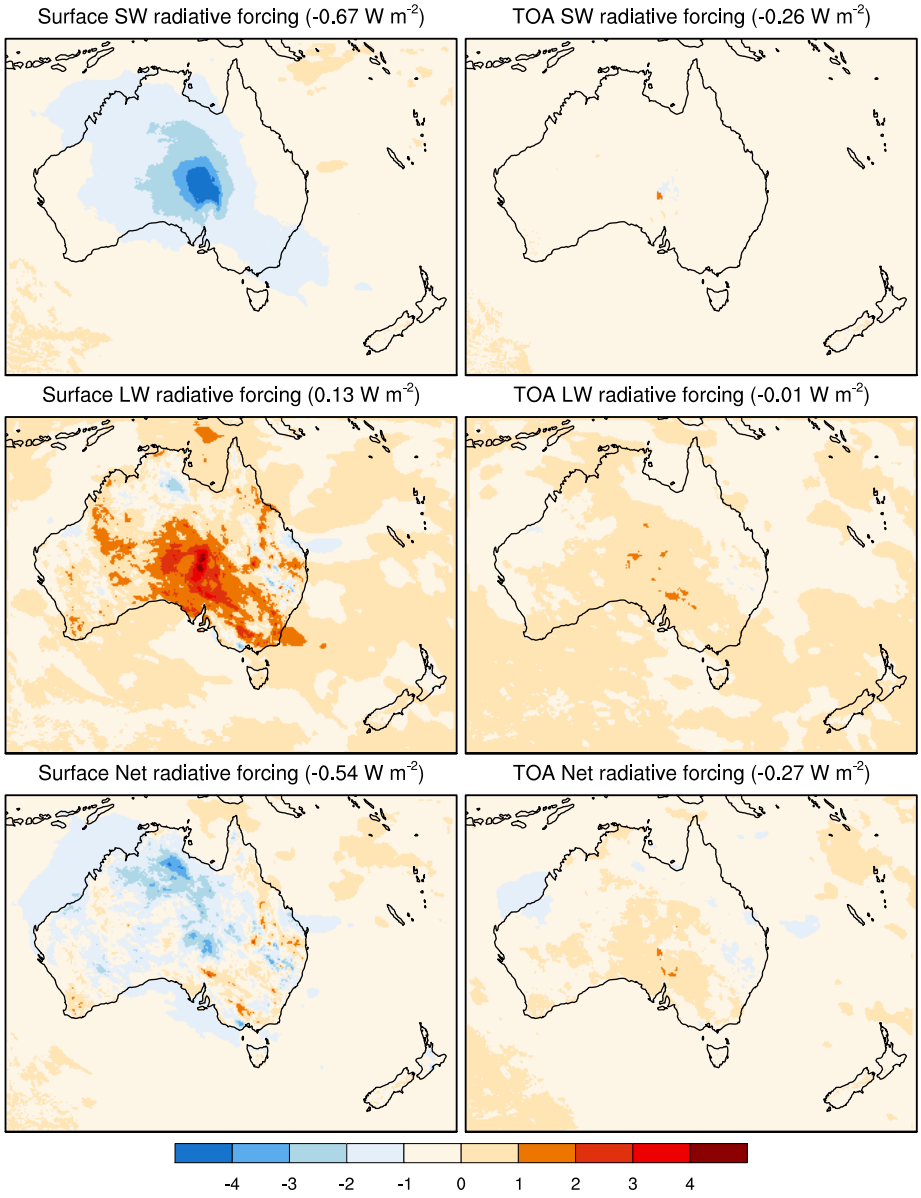

Figure 5.6. Simulated clear-sky shortwave, longwave and net (shortwave + longwave) direct radiative forcing (W m^{-2}) by dust aerosols at the surface and TOA averaged from September 2009 to February 2010. The domain averaged radiative forcing by dust averaged over the simulation period is indicated in brackets for each panel.

is a value of 0.27 W m^{-2} which represents the amount of radiation that is absorbed by mineral dust. Note that both shortwave and longwave radiative forcing of dust is higher over the dust source regions in central eastern Australia (as shown in Figure 5.6) because of higher AOD (Figure 5.5). The higher longwave radiative forcing over central eastern

Table 5.2. Simulated clear-sky monthly averaged shortwave, longwave and net (shortwave + longwave) direct radiative forcing (W m^{-2}) by dust aerosols at the surface and TOA over Lake Eyre Baisn (28°S and 137.5°E).

	SW (W m^{-2})		LW (W m^{-2})		Net (W m^{-2})	
	Surface	TOA	Surface	TOA	Surface	TOA
Sep	-5.61	-1.56	3.35	0.32	-2.26	-1.24
Oct	-6.35	-1.59	3.67	0.5	-2.68	-1.09
Nov	-6.47	-1.44	4.42	1.05	-2.05	-0.39
Dec	-7.14	-1.36	3.75	0.38	-3.39	-0.98
Jan	-9.83	-1.62	6.78	2.26	-3.05	0.64
Feb	-8.05	-1.68	4.49	1.16	-3.56	-0.52
Mean	-7.24	-1.54	4.41	0.94	-2.83	-0.6

Australia is also due to a stronger interaction between longwave radiation and coarse dust particles that are more abundant over and near the source regions.

Table 5.2 shows simulated clear-sky monthly mean and a 6-month averaged direct radiative forcing of dust at the surface and TOA over Lake Eyre Basin. Over the simulation period, the longwave warming effect of dust (4.41 W m^{-2}) offsets 60.9% of its shortwave cooling effect (-7.24 W m^{-2}) at the surface. At the TOA, the longwave warming effect of dust (0.94 W m^{-2}) accounts for 61% of its shortwave cooling effect (-1.54 W m^{-2}). Consequently, the net impact of dust is a negative forcing both at the surface and TOA, with values of -2.83 W m^{-2} and -0.6 W m^{-2}, respectively. The net negative forcing at the surface and TOA demonstrates a reduction of radiation reaching the surface and an increase of reflection of radiation to space, respectively. The difference between net radiative forcing at the surface and TOA is 2.23 W m^{-2}, representing the amount of radiation that is absorbed by mineral dust. Note that over Lake Eyre Basin, the longwave warming effect has a larger contribution to countering the shortwave cooling effect of dust (reaching 60.9% at the surface) compared to the domain averaged contribution (reaching 19.4% at the surface). This is because larger dust particles are more abundant over dust source regions, which therefore have a stronger interaction with longwave radiation.

Diurnal cycles of downward and upward shortwave and longwave fluxes at the surface and TOA over Lake Eyre Basin averaged over the simulation period for both dust and dust-free conditions are shown in Figure 5.7, and the corresponding daily averages are

given in brackets. At the surface, downward shortwave radiative forcing is negative due to absorption and backscattering of solar radiation by dust. It varies with solar zenith angle during daytime with stronger forcing in the early afternoon because the Sun's rays are near vertical and have their strongest intensity, but also because aerosol absorption decreases with increasing solar zenith angle (*Yu et al.*, 2006). In contrast, downward longwave radiative forcing by mineral dust is positive during both day and night. Daily average downward shortwave radiative forcing has a negative value of -8.9 W m^{-2}, while daily average downward longwave radiative forcing has a positive value of 3.7 W m^{-2}.

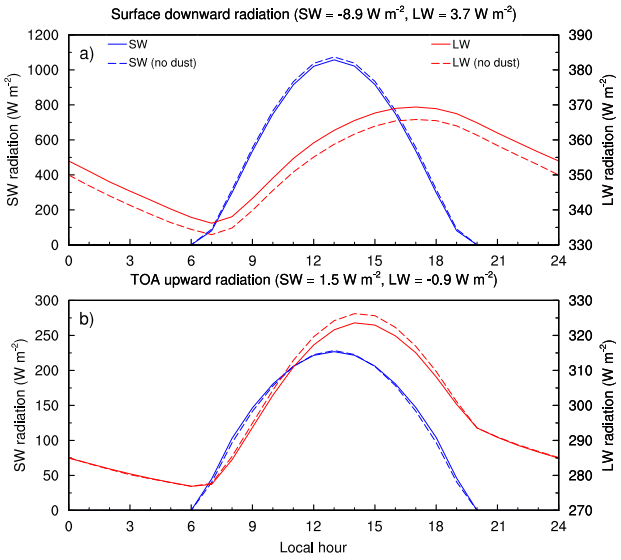

Figure 5.7. Clear-sky diurnal cycle of (a) downward shortwave and longwave radiation (W m^{-2}) at the surface and (b) upward shortwave and longwave radiation (W m^{-2}) at the TOA over Lake Eyre Basin (28°S and 137.5°E) averaged for a 6-month period from September 2009 to February 2010. The daily average shortwave and longwave radiative forcing by dust at the surface and TOA is indicated for each panel.

At the TOA, upward shortwave radiative forcing by dust is positive, with a daily average value of 1.5 W m^{-2}. In contrast, upward longwave radiative forcing overall is negative, with a daily average value of -0.9 W m^{-2}. This leads to a net upward daily mean radiative forcing of 0.4 W m^{-2}, meaning that mineral dust increases reflection of radiation to space, corresponding to a cooling of the atmosphere. Upward longwave radiative forcing by dust at the TOA is negative during daytime. This implies that during daytime mineral dust decreases scattering of longwave radiation to space. Upward shortwave direct radiative

forcing at the TOA has its lowest value at noon and in the early afternoon when the Sun's rays are near vertical and passing through fewer dust aerosols. This implies that the fraction of shortwave radiation scattered back to space is a function of solar zenith angle. Note that there is a lag between the maximum incoming longwave radiation at the surface and the maximum outgoing longwave radiation at the TOA in Figure 5.7. The reason for this is that the incoming longwave radiation at the surface is a function of the weighted average temperature of the column of atmosphere above Lake Eyre Basin and it takes a long time for the column of air to heat up, while the outgoing longwave radiation at the TOA is predominantly a function of land surface temperature that heats up very quickly in the early afternoon.

5.6 Atmospheric Heating and Cooling Rates

Atmospheric heating and cooling profiles due to the interaction of shortwave and longwave radiation with dust aerosols over Lake Eyre Basin averaged for spring and summer are shown in Figure 5.8. Due to absorption of radiation by dust, the shortwave heating effect of dust is simulated with a maximum rate of around 0.35 K day^{-1} and 0.45 K day^{-1} near the surface in spring and summer, respectively (Figure 5.8a). The shortwave heating effect has a decreasing trend with altitude, reflecting fewer and smaller dust particles at higher levels (as smaller dust particles are less absorbing). The shortwave heating of the atmosphere is a unique characteristic of absorbing aerosols such as mineral dust. In contrast, the longwave effect of dust in the atmosphere is negative with a rate reaching a value of around -0.6 K day^{-1} and -0.5 K day^{-1} near the surface in spring and summer, respectively, and a decreasing trend with altitude (Figure 5.8b). The longwave effect of dust cools the atmosphere because absorption of longwave radiation by mineral dust is less than its emission to the surface and TOA. Near the surface, large dust particles are generally present (particularly over dust source areas) that have a stronger interaction with longwave radiation, and because this interaction is present both during day and night, the longwave cooling rate of the atmosphere by dust dominates over the shortwave warming

effect. In contrast, shortwave atmospheric heating dominates at higher altitudes where there is less interaction between dust particles and longwave radiation due to presence of smaller size particles at higher altitudes. As a result, the net direct radiative impact of mineral dust produces cooling of the atmosphere near the surface (below around 0.2 km) with maximum rates of around -0.25 K day^{-1} and -0.09 K day^{-1} in spring and summer, respectively. In contrast, warming of the atmosphere aloft (above 0.2 km) is simulated with maximum rates of around 0.12 K day^{-1} and 0.18 K day^{-1} at 0.5 km height in spring and summer, respectively (Figure 5.8c). The cooling at the surface (Figure 5.6) and in the lower atmosphere (below around 0.2 km height), and warming the atmosphere aloft (Figure 5.8c) contributes to stabilizing the atmosphere over central eastern Australia.

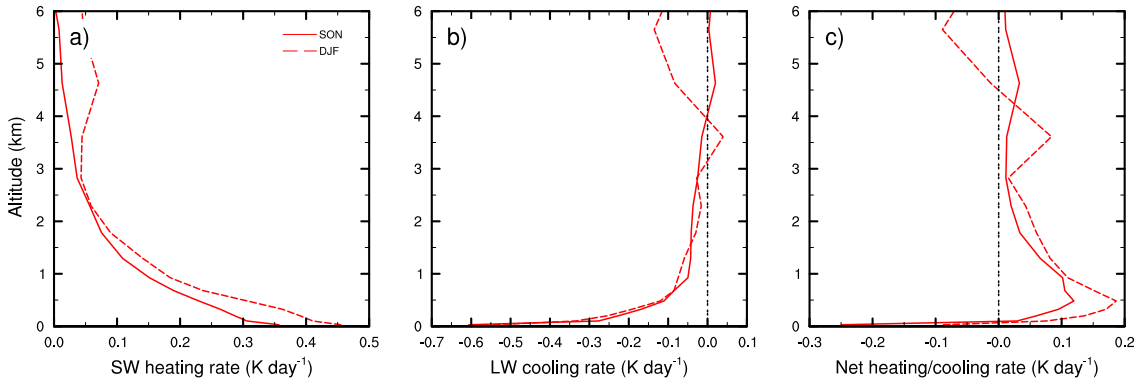

Figure 5.8. Simulated atmospheric heating and cooling profiles (K day^{-1}) due to the interaction of (a) shortwave, (b) longwave and (c) net (shortwave + longwave) radiation with dust aerosols averaged for austral spring (solid red line) and summer (dashed red line) over Lake Eyre Basin (28°S and 137.5°E).

It should be noted that although the net direct radiative effect of dust for the entire day is cooling the lower atmosphere and warming the layers above (Figure 5.8c), its impact on the vertical profile of potential temperature and subsequent impact on the stability of the atmosphere is different during day and night. During daytime, a reduction of shortwave radiation reaching the surface is associated with a decrease of potential temperature in the lower atmosphere and its increase in layers above, leading to an increase of atmospheric stability. During nighttime, on the other hand, trapping of the longwave radiation results in an increase of potential temperature in the lower atmosphere, and a decrease in atmospheric layers above, which in turn destabilizes the atmosphere.

5.7 Discussion and Conclusions

Shortwave and longwave direct radiative forcing by mineral dust aerosols over Australia has been investigated in a dry El Niño year during austral spring and summer when dust outbreaks over central eastern Australia are most frequent using the WRF/Chem regional model with the GOCART simple aerosol scheme. The model results are complemented by satellite data to investigate monthly variation of mineral dust distribution. There are some differences between the simulated and satellite retrievals of AOD which mainly arise from using the simplified GOCART dust emission scheme that considers preferential sources based on erodible fraction rather than individual soil particle properties (*Cavazos Guerra*, 2011). However, there are some uncertainties in the retrieved AOD from satellites, most notably associated with cloud contamination and variability of surface albedo over land (*Yu et al.*, 2006).

Mineral dust from interior Australia is simulated to be mainly transported in a north to northwest direction towards the tropical regions of northern Australia and the Indian Ocean, and an east to southeastward direction towards the Coral and Tasman Seas and the Southern Ocean. These transport pathways are consistent with the results of *Alizadeh Choobari et al.* (2012a) using the dust transport (DUSTRAN) module embedded within the WRF/Chem model for a single severe dust event over Australia during 22-23 September 2009. Retrieved dust extinction coefficient profiles from CALIOP indicate that on a long-term basis (2006-2011) the peak dust activity over Australia occurs during summer, followed by spring. The maximum dust activity in the spring-summer period is in agreement with the results of *Radhi et al.* (2010) using AERONET observations, who identified maximum aerosol content with coarse mode at this time of the year. The spring-summer peak is caused by strong winds associated with the passage of non-precipitating cold fronts (*Ekstrom et al.*, 2004) and dry conditions. The summer peak dust load simulated by the model and observed by CALIOP (for the period 2006-2011) is consistent with the results of *Ekstrom et al.* (2004) using ground-based measurements for the period 1960 to 1999, and *Mitchell et al.* (2010) using the AERONET observations at Tinga Tingana

(29°S and 139.59°E), Lake Eyre Basin for the period 2003 to 2007.

Mineral dust aerosols reach a maximum height of around 4 km over Lake Eyre Basin in spring and summer, which is lower than the dust layer over North Africa (*Liu et al.*, 2008) and the Taklimakan desert (*Huang et al.*, 2008). Dust concentrations over Lake Eyre Basin decrease substantially in autumn and winter when the top of the dust layer only reaches a height of around 2.5 km and 1.5 km, respectively. The lower elevation of Australian dust aerosols implies that they have a lower surface radiative cooling effect than "dust belts" of the Northern Hemisphere because there is little vertical exchange of the heat absorbed by mineral dust and the surface when the dust layer is located well above the boundary layer (*Chung and Zhang*, 2004).

Clear-sky domain averaged shortwave direct radiative forcing by dust averaged over the simulation period is estimated to be -0.67 W m^{-2} and -0.26 W m^{-2} at the surface and TOA, respectively. The shortwave surface cooling effect of dust is about 2.6 times larger than the TOA cooling effect because of dust aerosol absorption. The simulated shortwave cooling at the surface (-0.67 W m^{-2}) is less than the observed annual average global shortwave direct forcing over land and ocean (-10.3 W m^{-2}) (*Yu et al.*, 2006). The lower estimates of shortwave radiative forcing by dust over Australia simulated by the WRF/Chem model are expected because the model-based estimates of direct radiative forcing are generally smaller than the satellite-based estimates (*Yu et al.*, 2006). Such discrepancy partly arises because satellite-based direct radiative effect estimates are contaminated by clouds and are poorly constrained over land due to variability of surface albedo. Indeed, as outlined by *Yu et al.* (2006), the satellite-based direct radiative effect estimates are reduced and become more consistent with the model-based estimates after considering cloud contamination.

The domain averaged shortwave and longwave direct radiative forcing by mineral dust over Australia is substantially lower than model-based estimates over West Africa. For example, a -12.37 W m^{-2} shortwave cooling and 6.26 W m^{-2} longwave warming effect of mineral dust was simulated at the surface over West Africa during 1 May to 30 September

2006 using the WRF/Chem model (*Zhao et al.*, 2011), which is significantly higher than the -0.67 W m^{-2} shortwave cooling and 0.13 W m^{-2} longwave warming estimates obtained in the present study. This suggests a lesser impact of Australian dust on the Earth's climate system compared to other major dust sources in the Northern Hemisphere.

The atmospheric heating rate due to the interaction of shortwave radiation with dust aerosols is simulated because mineral dust absorbs both incoming and outgoing shortwave radiation. The maximum shortwave heating rate over Lake Eyre Basin occurred near the surface with a maximum value of about 0.4 K day^{-1} averaged over the simulation period and a decreasing trend with altitude. The shortwave heating of the atmosphere is similar to the results of *Zhao et al.* (2010), who identified a maximum shortwave heating rate of around 0.8 K day^{-1} but at 0.5 km height at Niamey airport during 13 January to 3 February 2006. In contrast, the effect of dust on longwave radiation in the atmosphere is found to be negative with a maximum rate of around -0.55 K day^{-1} near the surface averaged over the simulation period, and a rapid decrease with altitude. The cooling of the atmosphere due to interaction of suspended dust with longwave radiation is similar to the results of *Zhao et al.* (2011) over West Africa who attributed such cooling to the increased atmospheric outgoing longwave radiation by dust aerosols. Therefore, dust induces contrasting longwave cooling and shortwave warming of the atmosphere. Near the surface (below 0.2 km) where larger dust particles are more abundant, the longwave cooling effect of the atmosphere by dust is greater than the shortwave warming effect of the atmosphere. In contrast, at higher altitudes (above 0.2 km) where smaller dust particles are more abundant, the opposite is true. This leads to a net cooling of the atmosphere near the surface (below 0.2 km), and warming of the atmosphere above, which has consequences for increasing the stability of the atmosphere. This increased stability due to direct radiative forcing of mineral dust is consistent with previous studies (e.g. *Miller et al.*, 2004b).

This study only examined the direct radiative forcing by mineral dust over Australia during a 6-month period of austral spring and summer in a dry El Niño year, while such forcing is expected to have lower values in neutral or wet La Niña years. Therefore, the

results do not necessarily provide a comprehensive climatology of the direct radiative forcing by dust aerosols over Australia. To fully understand the regional climate impact of mineral dust over Australia, long-term multi-year simulations that include both direct and indirect effects need to be conducted.

Chapter 6

Conclusions

The aim of this study was to address transport, vertical distribution, direct radiative forcing and impact of mineral dust on boundary layer dynamics over Australia based on the WRF/Chem model simulations, while supporting measurements have been used to identify three dimensional distribution of Australian dust. Simulations were conducted both for a case study on 22-23 September 2009 when a severe dust event occurred in response to the passage of an extratropical cold frontal system, and for a longer time period during spring and summer in a dry El Niño year when dust storm activities are strongest over Lake Eyre Basin, the most active persistent source of dust over Australia. To our knowledge, this study is the first attempt to quantify direct radiative forcing by mineral dust and its subsequent impact on regional scale atmospheric dynamics over Australia.

Frontal systems play a significant contribution to entrainment of mineral dust particles from desert areas of Australia and their subsequent long-range transport. Variation of the boundary layer structure during the passage of cold fronts, as well as strong ascending motion in the warm conveyor belt along the leading edge of the cold front and descending motion over the regions that are dominated by post-frontal anticyclonic circulation play important roles in the vertical distribution of dust particles across Australia. Boundary layer depth is deeper behind the cold front due to strong cold advection over relatively warm surfaces. This region is also associated with the maximum dust concentrations as a result of strong near-surface wind speeds. This suggests that dust is mainly picked up from the surface by post-frontal winds over Australia, consistent with the results of *Leys et al.* (2011) for the same dust event. Dust particles are then mixed through the depth of the boundary layer behind the cold front due to substantial turbulent mixing in the well-mixed boundary layer. However, over the area that is dominated by anticyclonic circulation, particle concentrations are low and less elevated. Indeed, large-scale descending

motion traps the particles in lower layers of the atmosphere, while subsequent horizontal transport toward low-pressure regions occurs by divergent winds around the fringes of the anticyclone. In the warm sector ahead of the cold front, boundary layer depth is relatively shallow due to warm advection over cold surfaces. However, warm advection contributes to strong ascending motions in the conveyor belt along the frontal zone, contributing to transport of some dust to the free atmosphere. Despite the strong ascending motions ahead of the cold front, it has been shown that Australian dust plumes are mostly transported in the lower atmosphere. Indeed, mineral dust aerosols reach a maximum seasonally averaged height of around 4 km over Lake Eyre Basin during peak dust activity in spring and summer, which is lower than the North African (*Liu et al.*, 2008) and Asian (Taklimakan) (*Huang et al.*, 2008) dust source regions where dust layers have been observed at much greater height above ground.

Two major exit pathways of Australian dust have been identified: (1) eastward to southeastward by pre-frontal northwesterly winds and eastward propagating frontal systems; and (2) north to northeastward to tropical Australia by post-frontal south to southwesterly winds, and subsequent transport of dust towards northwestern Australia and the Indian Ocean by the anticyclonic circulation behind the cold front and southeasterly trade winds that dominate over northern tropical Australia. It is noteworthy that our results show that quite significant amounts of dust can be transported to northern Australia, a feature that has been neglected in previous studies that found two major exit pathways of Australian dust to the southeast and northwest (*Knight et al.*, 1995; *McGowan et al.*, 2005; *McTainsh et al.*, 2005; *Shao*, 2008).

The spring-summer maximum dust activity over Lake Eyre Basin has been identified using the MISR and CALIOP satellite data, which is consistent with the results of *Mitchell et al.* (2010) and *Radhi et al.* (2010) using AERONET observations and *Ekstrom et al.* (2004) using ground-based measurements. The spring-summer peak is caused by strong winds associated with the passage of non-precipitating cold fronts (*Ekstrom et al.*, 2004) and dry conditions during these seasons.

Shortwave direct radiative forcing by mineral dust is shown to be associated with the daytime cooling of the atmosphere from the surface to near the boundary layer top due to backscattering and absorption of solar radiation, but warming of the boundary layer top and lower free atmosphere because of absorption of shortwave radiation. Cooling of the atmosphere near the surface has been also noted in previous studies over other major sources of dust in the Northern Hemisphere. For example, *Mallet et al.* (2009) identified substantial surface cooling of -4.5°C over North Africa during a dust event over the period 7-14 March 2006. The combination of cooling of the lower atmosphere and warming of the upper boundary layer reduces the vertical exchange of horizontal momentum, and results in a decrease of wind speed in the lower boundary layer and its increase within the upper boundary layer and lower free atmosphere, although locally an increase of wind speed has also been identified. The pattern of both decrease and increase of near-surface wind speed identified in the current study is similar to the results of *Heinold et al.* (2007) and *Yue et al.* (2010).

Both shortwave and longwave direct radiative forcing by mineral dust aerosols in clear-sky conditions has also been investigated over Australia during spring and summer in a dry El Niño year. Over the Australian region, the spring-summer averaged clear-sky shortwave direct radiative forcing of dust has a cooling effect of -0.67 W m^{-2} and -0.26 W m^{-2} at the surface and TOA, respectively. The shortwave cooling at the surface is due to scattering and absorption of incoming solar radiation by dust aerosols, while the cooling at the TOA indicates increased shortwave reflection to space. In contrast, mineral dust traps longwave radiation, which is associated with a warming effect at the surface. Longwave direct radiative forcing of dust in clear-sky conditions is simulated to be 0.13 W m^{-2} and -0.01 W m^{-2} at the surface and TOA, respectively. Consequently, the spring-summer averaged net direct radiative forcing of dust is simulated to cause cooling both at the surface and TOA with values of -0.54 W m^{-2} and -0.27 W m^{-2}, respectively. The net negative direct radiative forcing of dust at the TOA corresponds to a cooling of the atmosphere by an increase of outgoing radiation (which is largely dominated by increased shortwave reflection to space), and is similar to the results of *Qin and Mitchell* (2009)

over Australia using AERONET observations. It should be noted that our estimates of shortwave and longwave direct radiative forcing of dust over Australia are substantially lower than model-based estimates over West Africa (e.g. *Zhao et al.*, 2011), suggesting less impact of Australian dust on the Earth's climate system compared to other major dust sources in the Northern Hemisphere.

Shortwave and longwave direct radiative forcing by mineral dust at the surface and TOA is shown to have a diurnal variation due to changes in solar zenith angle and in the intensity of longwave radiation emitted from the surface, with maximum reduction of incoming solar radiation at the surface and minimum backscattering of solar radiation to the TOA at noon. Furthermore, mineral dust produces contrasting daytime negative and nighttime positive upward longwave radiative forcing at the TOA.

It is likely that phenomena such as the El Niño Southern Oscillation (ENSO) are responsible for inter-annual variation of mineral dust emission and subsequent dust transport pathways over Australia, and analysis of the effect of such inter-annual controls would make a useful follow-up study to the current one. In addition, dust particle size distribution over Australia needs to be quantified and its difference with the other important sources of dust can be identified. Previous studies suggest that climate models underestimate the size of the global dust cycle (*Kok*, 2011), and such quantitative analysis can be used for evaluation of numerical simulation studies. How dust particles evolve during transport also remains largely unexplored over Australia. Possible future changes in dust emission and its transport over Australia, and how these changes will affect the climate system and environment need to be determined in the future.

The vertical distribution of Australian dust particles and the height at which they are transported, as well as meteorological processes relevant to the transport need to be further investigated. In particular, differences and similarities between dust transport pathways and meteorology processes in the Southern Hemisphere and the Northern Hemisphere (where extensive literature exists) can be be identified. In such studies, analysis of vertical profiles of dust obtained from the AERONET surface network sites over Australia can be

used for calibration of space-borne instruments and evaluation of numerical simulation studies.

As the refractive index of mineral dust depends on the mineralogy and composition of dust over a given region, the predominant mineralogical composition and optical properties of dust over Australia need to be determined. Future investigation is recommended to identify microphysical properties of dust over Australia as they are crucial to climate effects (both direct and indirect effects).

The present study only examined the direct radiative effect of dust over Australia. To fully understand the regional climate impact of Australian dust, long-term multi-year simulations that include direct, semi-direct and indirect effects of mineral dust need to be conducted. Furthermore, current estimates of the direct radiative forcing by dust are model derived, and observation based studies also need to be conducted.

References

Ackerman, A. S., O. B. Toon, D. E. Stevens, A. J. Heymsfield, V. Ramanathan, and E. J. Welton (2000), Reduction of tropical cloudiness by soot, *Science*, *288*(5468), 1042–1047, doi:10.1126/science.288.5468.1042.

Albrecht, B. A. (1989), Aerosols, cloud microphysics, and fractional cloudiness, *Science*, *245*(4923), 1227–1230.

Alizadeh Choobari, O., P. Zawar-Reza, and A. Sturman (2012a), Atmospheric forcing of the three-dimensional distribution of dust particles over Australia: A case study, *J. Geophys. Res.*, *117*, D11,206, doi:10.1029/2012JD017748.

Alizadeh Choobari, O., P. Zawar-Reza, and A. Sturman (2012b), Atmospheric forcing of the three-dimensional distribution of dust particles over Australia: A case study, *J. Geophys. Res.*, *117*, D11,206, doi:10.1029/2012JD017748.

Alizadeh Choobari, O., P. Zawar-Reza, and A. Sturman (2013a), Low level jet intensification by mineral dust aerosols, *Ann. Geophys.*, *31*, 625–632, doi:10.5194/angeo-31-625-2013.

Alizadeh Choobari, O., P. Zawar-Reza, and A. Sturman (2013b), Simulation of the spatial distribution of mineral dust and its direct radiative forcing over Australia, *Tellus B*, *65*, 19,856, doi:10.3402/tellusb.v65i0.19856.

Andreae, M. O., D. Rosenfeld, P. Artaxo, A. A. Costa, G. P. Frank, K. M. Longo, and M. A. F. Silva-Dias (2004), Smoking rain clouds over the Amazon, *Science*, *303*(5662), 1337–1342, doi:10.1126/science.1092779.

Arimoto, R., B. J. Huebert, A. D. Clarke, Y. Shinozuka, R. J. Weber, S. A. Guazzotti, R. C. Sullivan, D. A. Sodeman, K. A. Prather, I. N. Sokolik, Y. J. Kim, Y. P. Kim, P. K. Quinn, T. S. Bates, T. L. Anderson, J. R. Anderson, S. Gong, I. Uno, and M. Chin (2006), Characterization of Asian Dust during ACE-Asia, *Global Planet. Change*, *52*(1), 23–56.

Astitha, M., G. Kallos, C. Spyrou, W. O'Hirok, J. Lelieveld, and H. A. C. Denier van der Gon (2010), Chemically aged and mixed aerosols over the Central Atlantic Ocean - potential impacts, *Atmos. Chemis. Phys. Discuss.*, *10*(2), 5185–5231.

Balkanski, Y. J., D. J. Jacob, G. M. Gardner, W. C. Graustein, and K. K. Turekian (1993), Transport and residence times of tropospheric aerosols inferred from a global three-dimensional simulation of 210Pb, *J. Geophys. Res.*, *98*(D11), 20,573–20,586.

Bierwirth, E., M. Wendisch, A. Ehrlich, B. Heese, M. Tesche, D. Althausen, A. Schladitz, D. Muller, S. Otto, T. Trautmann, T. Dinter, W. Von Hoyningen-Huene, and R. Kahn (2009), Spectral surface albedo over morocco and its impact on radiative forcing of saharan dust, *Tellus B*, *61*(1), 252–269.

Binkowski, F., and U. Shankar (1995), The Regional Particulate Matter Model 1. Model description and preliminary results, *J. Geophys. Res.*, *100*(D12), 26,191–26,209, doi:10.1029/95JD02093.

Bluestein, H. B. (1992), *Synoptic-dynamic meteorology in midlatitudes.*, Oxford University Press, New York.

Bolin, B., G. Aspling, and C. Persson (1973), *Residence time of atmospheric pollutants: as dependent on source characteristics, atmospheric diffusion processes and sink mechanisms*, Institute of Meteorology, University of Stockholm, Stockholm.

Botterill, L. C. (2003), Uncertain climate: the recent history of drought policy in Australia, *Aus. J. Pol. His.*, *49*(1), 61–74.

Breon, F. M., and S. Colzy (2000), Global distribution of cloud droplet effective radius from POLDER polarization measurements, *Geophys. Res. Lett.*, *27*(24), 4065–4068.

Brown, A. R. (1996), Evaluation of parametrization schemes for the convective boundary layer using large-eddy simulation results, *Boundary-Layer Meteorol.*, *81*(2), 167–200.

Bullard, J. E., and G. H. McTainsh (2003), Aeolian-fluvial interactions in dryland environments: examples, concepts and Australia case study, *Prog. Phys. Geog.*, *27*(4), 471–501.

Cavazos Guerra, C. d. C. (2011), Modelling the atmospheric controls and climate impact of mineral dust in The Sahara Desert, Ph.D. thesis, University College London.

Chapman, E. G., W. I. Gustafson, R. C. Easter, J. C. Barnard, S. J. Ghan, M. S. Pekour, and J. D. Fast (2009), Coupling aerosol-cloud-radiative processes in the WRF-Chem model: Investigating the radiative impact of elevated point sources, *Atmos. Chemis. Phys.*, *9*(3), 945–964.

Chen, F., and J. Dudhia (2001), Coupling an advanced land surface-hydrology model with the Penn State-NCAR MM5 modeling system. Part I: Model implementation and sensitivity, *Mon. Weather Rev.*, *129*(4), 569–585.

Cheng, C., W. Wang, and J. Chen (2007), A modelling study of aerosol impacts on cloud microphysics and radiative properties, *Q. J. R. Meteorol. Soc.*, *133*(623), 283–297.

Chin, M., P. Ginoux, R. Lucchesi, B. Huebert, R. Weber, T. Anderson, S. Masonis, B. Blomquist, A. Bandy, and D. Thornton (2003), A global aerosol model forecast for the ACE-Asia field experiment, *J. Geophys. Res.*, *108*, D23, doi:10.1029/2003JD003642.

Chung, C. E., and G. J. Zhang (2004), Impact of absorbing aerosol on precipitation: Dynamic aspects in association with convective available potential energy and convective parameterization closure and dependence on aerosol heating profile, *J. Geophys. Res.*, *109*, D22,103, doi:10.1029/2004JD004726.

Darmenova, K., I. N. Sokolik, Y. Shao, B. Marticorena, and G. Bergametti (2009), Development of a physically based dust emission module within the Weather Research and Forecasting (WRF) model: Assessment of dust emission parameterizations and input parameters for source regions in Central and East Asia, *J. Geophys. Res.*, *114*, D14,201, doi:10.1029/2008JD011236.

Dubovik, O., and M. D. King (2000), A flexible inversion algorithm for retrieval of aerosol optical properties from Sun and sky radiance measurements, *J. Geophys. Res.*, *105*(D16), 20,673–20,696.

Dubovik, O., B. Holben, T. F. Eck, A. Smirnov, Y. J. Kaufman, M. D. King, D. Tanre, and I. Slutsker (2002), Variability of absorption and optical properties of key aerosol types observed in worldwide locations, *J. Atmos. Sci.*, *59*(3), 590–608.

Durant, A. J., S. P. Harrison, I. M. Watson, and Y. Balkanski (2009), Sensitivity of direct radiative forcing by mineral dust to particle characteristics, *Progress Phys. Geog.*, *33*(1), 80–102, doi: 10.1177/0309133309105034.

Eckhardt, S., A. Stohl, H. Wernli, P. James, C. Forster, and N. Spichtinger (2004), A 15-year climatology of warm conveyor belts, *J. Climate*, *17*(1), 218–237.

Edwards, D. P., L. K. Emmons, J. C. Gille, A. Chu, J.-L. Attie, L. Giglio, S. W. Wood, J. Haywood, M. N. Deeter, S. T. Massie, D. C. Ziskin, and J. R. Drummond (2006), Satellite-observed pollution from Southern Hemisphere biomass burning, *J. Geophys. Res.*, *111*, D14,312, doi:10.1029/2005JD006655.

Eguchi, K., I. Uno, K. Yumimoto, T. Takemura, A. Shimizu, N. Sugimoto, and Z. Liu (2009), Trans-pacific dust transport: integrated analysis of NASA/CALIPSO and a global aerosol transport model, *Atmos. Chemis. Phys.*, *9*(9), 3137–3145.

Ek, M. B., K. E. Mitchell, Y. Lin, E. Rogers, P. Grunmann, V. Koren, G. Gayno, and J. D. Tarpley (2003), Implementation of Noah land surface model advances in the National Centers for Environmental Prediction operational mesoscale Eta model, *J. Geophys. Res.*, *108*(D22), 8851, doi:10.1029/2002JD003296.

Ekstrom, M., G. H. McTainsh, and A. Chappell (2004), Australian dust storms: temporal trends and relationships with synoptic pressure distributions (1960-99), *Int. J. Climatol.*, *24*(12), 1581–1599, doi: 10.1002/joc.1072.

Engelstaedter, S., I. Tegen, and R. Washington (2006), North African dust emissions and transport, *Earth Sci. Rev.*, *79*(1), 73–100.

Fecan, F., B. Marticorena, and G. Bergametti (1998), Parametrization of the increase of the aeolian erosion threshold wind friction velocity due to soil moisture for arid and semi-arid areas, *Annales Geophys.*, *17*(1), 149–157.

Ferek, R. J., Q. F. Liu, B. A. Albrecht, D. Babb, T. Garrett, P. V. Hobbs, S. Strader, D. Johnson, J. P. Taylor, K. Nielsen, A. S. Ackerman, and Y. Kogan (2000), Drizzle suppression in ship tracks, *J. Atmos. Sci.*, *57*(16), 2707–2728.

Forster, P., V. Ramaswamy, P. Artaxo, T. Berntsen, R. Betts, D. W. Fahey, J. Haywood, J. Lean, D. C. Lowe, G. Myhre, J. Nganga, R. Prinn, G. Raga, M. Schulz, and R. V. Dorland (2007), *Changes in atmospheric constituents and in radiative forcing*, Cambridge University Press, Cambridge.

Fung, I. Y., S. K. Meyn, I. Tegen, S. C. Doney, J. G. John, and J. K. B. Bishop (2000), Iron supply and demand in the upper ocean, *Global Biogeochem. Cycl.*, *14*(1), 281–295.

Gaiero, D. M., F. Brunet, J.-L. Probst, and P. J. Depetris (2007), A uniform isotopic and chemical signature of dust exported from Patagonia: Rock sources and occurrence in southern environments, *Chem. Geology*, *238*(1), 107–120.

Garcia, O. E., F. J. Exposito, J. P. Diaz, and A. M. Diaz (2011), Radiative forcing under mixed aerosol conditions, *J. Geophys. Res.*, *116*, D01,201, doi:10.1029/2009JD013625.

Gillani, N. V., and W. E. Wilson (1983), Gas-to-particle conversion of sulfur in power plant plumesII. Observations of liquid-phase conversions, *Atmos. Environ. (1967)*, *17*(9), 1739–1752.

Ginoux, P., M. Chin, I. Tegen, J. Prospero, B. Holben, O. Dubovik, and S. Lin (2001), Sources and distributions of dust aerosols simulated with the GOCART model., *J. Geophys. Res.*, *106*(D17), 20,255–20,273, doi:10.1029/2000JD000053.

Ginoux, P., J. Prospero, O. Torres, and M. Chin (2004), Long-term simulation of global dust distribution with the GOCART model: correlation with North Atlantic Oscillation., *Environ. Model. Software*, *19*(2), 113–128, doi:10.1016/S1364-8152(03)00114-2.

Ginoux, P. A., J. M. Prospero, T. E. Gill, C. Hsu, and M. Zhao (2012), Global-scale attribution of anthropogenic and natural dust sources and their emission rates based on MODIS Deep Blue aerosol products, *Rev. Geophys.*, *50*, RG3005, doi:10.1029/2012RG000388.

Goncalves, F. L. T., A. M. Ramos, S. Freitas, M. A. Silva Dias, and O. Massambani (2002), In-cloud and below-cloud numerical simulation of scavenging processes at Serra Do Mar region, SE Brazil, *Atmos. Environ.*, *36*(33), 5245–5255.

Goudie, A. S., and N. J. Middelton (2006), *Desert Dust in the Global System*, Springer.

Goudie, A. S., and N. J. Middleton (2001), Saharan dust storms: nature and consequences, *Earth Sci. Rev.*, *56*(1), 179–204.

Grell, G. A. (1993), Prognostic evaluation of assumptions used by cumulus parameterizations, *Mon. Weather Rev.*, *121*(3), 764–787.

Grell, G. A., S. E. Peckham, R. Schmitz, S. A. McKeen, G. Frost, W. C. Skamarock, and B. Eder (2005), Fully coupled "online" chemistry within the WRF model., *Atmos. Environ.*, *39*(37), 6957–6975, doi: 10.1016/j.atmosenv.2005.04.027.

Griffin, D. W., C. A. Kellogg, V. H. Garrison, and E. A. Shinn (2002), The global transport of dust, *American Scientist*, *90*(3), 228.

Gunn, R., and B. B. Phillips (1957), An experimental investigation of the effect of air pollution on the initiation of rain, *J. Meteorol.*, *14*(3), 272–280.

Hansell, R. A., S. C. Tsay, Q. Ji, N. C. Hsu, M. J. Jeong, S. H. Wang, J. S. Reid, K. N. Liou, and S. C. Ou (2010), An assessment of the surface longwave direct radiative effect of airborne Saharan dust during the NAMMA field campaign, *J. Atmos. Sci.*, *67*(4), 1048–1065.

Hansen, J., M. Sato, and R. Ruedy (1997), Radiative forcing and climate response., *J. Geophys. Res.*, *102*(D6), 6831–6864, doi:10.1029/96JD03436.

Haywood, J., and O. Boucher (2000), Estimates of the direct and indirect radiative forcing due to tropospheric aerosols: A review, *Rev. Geophys.*, *38*(4), 513–543.

Haywood, J. M., R. P. Allan, I. Culverwell, T. Slingo, S. Milton, J. Edwards, and N. Clerbaux (2005), Can desert dust explain the outgoing longwave radiation anomaly over the Sahara during July 2003?, *J. Geophys. Res.*, *110*, D05,105, doi:10.1029/2004JD005232.

Heinold, B., J. Helmert, O. Hellmuth, R. Wolke, A. Ansmann, B. Marticorena, B. Laurent, and I. Tegen (2007), Regional modeling of Saharan dust events using LM-MUSCAT: Model description and case studies, *J. Geophys. Res.*, *112*, D11,204, doi:10.1029/2006JD007443.

Heintzenberg, J. (2009), The SAMUM1 experiment over Southern Morocco: overview and introduction, *Tellus B*, *61*(1), 2–11.

Hofmann, D. J., J. H. Butler, E. J. Dlugokencky, J. W. Elkins, K. Masarie, S. A. Montzka, and P. Tans (2006), The role of carbon dioxide in climate forcing from 1979 to 2004: introduction of the Annual Greenhouse Gas Index, *Tellus B*, *58*(5), 614–619.

Hong, S. Y. (2010), A new stable boundary-layer mixing scheme and its impact on the simulated East Asian summer monsoon, *Q. J. R. Meteorol. Soc.*, *136*(651), 1481–1496, doi:10.1002/qj.665.

Hong, S. Y., Y. Noh, and J. Dudhia (2006), A new vertical diffusion package with an explicit treatment of entrainment processes, *Mon. Weather Rev.*, *134*(9), 2318–2341, doi:10.1175/MWR3199.1.

Hu, X. M., J. W. Nielsen-Gammon, and F. Q. Zhang (2010), Evaluation of three planetary boundary layer schemes in the WRF model, *J. Geophys. Res.*, *49*(9), 1831–1844.

Huang, J., P. Minnis, B. Chen, Z. Huang, Z. Liu, Q. Zhao, Y. Yi, and J. K. Ayers (2008), Long-range transport and vertical structure of Asian dust from CALIPSO and surface measurements during PACDEX, *J. Geophys. Res.*, *113*, D23,212, doi:10.1029/2008JD010620.

Huang, J., Q. Fu, J. Su, Q. Tang, P. Minnis, Y. Hu, Y. Yi, and Q. Zhao (2009), Taklimakan dust aerosol radiative heating derived from CALIPSO observations using the Fu-Liou radiation model with CERES constraints, *Atmos. Chem. Phys.*, *9*(12), 4011–4021.

Huang, J. P., B. Lin, P. Minnis, T. H. Wang, X. Wang, Y. X. Hu, Y. H. Yi, and J. K. Ayers (2006), Satellite-based assessment of possible dust aerosols semi-direct effect on cloud water path over East Asia, *Geophys. Res. Lett.*, *33*(19), doi:10.1029/2006GL026561.

Huneeus, N., F. Dentener, T. Diehl, R. Easter, D. Fillmore, S. Ghan, P. Ginoux, A. Grini, L. Horowitz, D. Koch, M. Krol, M. Schulz, W. Landing, X. Liu, N. Mahowald, R. Miller, J. Morcrette, G. Myhre, J. Penner, J. Perlwitz, P. Stier, T. Takemura, Y. Balkanski, C. Zender, J. Griesfeller, J. Prospero, S. Kinne, S. Bauer, O. Boucher, and M. Chin (2011), Global dust model intercomparison in AeroCom phase I, *Atmos. Chem. Phys.*, *11*(15), 7781–7816, doi:10.5194/acp-11-7781-2011.

Husar, R. B., D. M. Tratt, B. A. Schichtel, S. R. Falke, F. Li, D. Jaffe, S. Gasso, T. Gill, N. S. Laulainen, F. Lu, M. C. Reheis, Y. Chun, D. Westphal, B. N. Holben, C. Gueymard, I. McKendry, N. Kuring, G. C.

Feldman, C. McClain, R. J. Frouin, J. Merrill, D. DuBois, F. Vignola, T. Murayama, S. Nickovic, W. E. Wilson, K. Sassen, N. Sugimoto, and W. C. Malm (2001), Asian dust events of April 1998., *J. Geophys. Res.*, *106*(D16), 18,317–18,330, doi:10.1029/2000JD900788.

IPCC (1994), *Climate Change 1994: Radiative Forcing of Climate Change and an Evaluation of the IPCC IS92 Emission Scenarios*, Cambridge Univ. Press, New York, Cambridge University Press, 1994.

Jacobson, M. Z. (2002), Control of fossil-fuel particulate black carbon and organic matter, possibly the most effective method of slowing global warming, *J. Geophys. Res.*, *107*(D19), 4410, doi:10.1029/2001JD001376.

Janjic, Z. (1990), The step-mountain coordinate - physical package, *Mon. Weather Rev.*, *118*(7), 1429–1443.

Janjic, Z. I. (2003), A nonhydrostatic model based on a new approach, *Meteorol. Atmos. Phys.*, *82*(1), 271–285, doi:10.1007/s00703-001-0587-6.

Jickells, T. D., K. A. Hunter, H. Kawahata, N. Kubilay, J. laRoche, P. S. Liss, N. Mahowald, J. M. Prospero, A. J. Ridgwell, I. Tegen, R. Torres, Z. S. An, K. K. Andersen, A. R. Baker, G. Bergametti, N. Brooks, J. J. Cao, P. W. Boyd, and R. A. Duce (2005), Global iron connections between desert dust, ocean biogeochemistry, and climate, *Science*, *308*(5718), 67–71.

Johnson, D. B. (1982), The role of giant and ultragiant aerosol particles in warm rain initiation, *J. Atmos. Sci.*, *39*(2), 448–460.

Kahn, R., R. Gaitley, J. Martonchik, D. Diner, K. Crean, and B. Holben (2005), MISR global aerosol optical depth validation based on two years of coincident AERONET observations, *J. Geophys. Res.*, *110*, D10S04, doi:10.1029/2004JD004706.

Karydis, V. A., P. Kumar, D. Barahona, I. N. Sokolik, and A. Nenes (2011), On the effect of dust particles on global cloud condensation nuclei and cloud droplet number, *J. Geophys. Res.*, *116*, D23,204, doi:10.1029/2011JD016283.

Kaufman, Y. J., I. Koren, L. A. Remer, D. Tanr, P. Ginoux, and S. Fan (2005), Dust transport and deposition observed from the Terra-Moderate Resolution Imaging Spectroradiometer (MODIS) spacecraft over the Atlantic Ocean, *J. Geophys. Res.*, *110*(D10), D10S12, doi:0.1029/2003JD004436.

Kiefert, L., G. H. McTainsh, and W. G. Nickling (1996), Sedimentological characteristics of Saharan and Australian dusts, *The Impact of Desert Dust Across the Mediterranean*, *11*, 183–190.

Knight, A. W., G. H. McTainsh, and R. W. Simpson (1995), Sediment loads in an Australian dust storm: implications for present and past dust processes, *Catena*, *24*(3), 195–213.

Koch, D., and A. D. Del Genio (2010), Black carbon semi-direct effects on cloud cover: review and synthesis., *Atmos. Chem. Phys.*, *10*(16), 7685–7696.

Kok, J. F. (2011), A scaling theory for the size distribution of emitted dust aerosols suggests climate models underestimate the size of the global dust cycle, *Proceedings of the National Academy of Sciences of the United States of America*, *108*(3), 1016–1021.

Koren, I., Y. J. Kaufman, L. A. Remer, and J. V. Martins (2004), Measurement of the effect of Amazon smoke on inhibition of cloud formation, *Science*, *303*(5662), 1342–1345, doi:10.1126/science.1089424.

Koren, I., Y. J. Kaufman, D. Rosenfeld, L. A. Remer, and Y. Rudich (2005), Aerosol invigoration and restructuring of Atlantic convective clouds., *Geophys. Res. Lett.*, *32*(14), L14,828, doi:10.1029/2005GL023187.

Koren, I., Y. J. Kaufman, R. Washington, M. C. Todd, Y. Rudich, J. Vanderlei Martins, and D. Rosenfeld (2006), The Bodélé depression: a single spot in the Sahara that provides most of the mineral dust to the Amazon forest, *Environ. Res. Lett.*, *1*(1), 014,005.

Korsholm, U. S. (2009), Integrated modeling of aerosol indirect effects, Ph.D. thesis, Danish Meteorological Institute.

Kowol-Santen, J., M. Beekmann, S. Schmitgen, and K. Dewey (2001), Tracer analysis of transport from the boundary layer to the free troposphere, *Geophys. Res. Lett.*, *28*(15), 2907–2910, doi:10.1029/2001GL012908.

Lau, K. M., K. M. Kim, Y. C. Sud, and G. K. Walker (2009), A GCM study of the response of the atmospheric water cycle of West Africa and the Atlantic to Saharan dust radiative forcing, *Annales Geophys.*, *27*(10), 4023–4037.

Leon, J.-F., D. Tanre, J. Pelon, Y. J. Kaufman, J. M. Haywood, and B. Chatenet (2003), Profiling of a Saharan dust outbreak based on a synergy between active and passive remote sensing, *J. Geophys. Res.*, *108*(D18), 8575.

Levin, Z., A. Teller, E. Ganor, and Y. Yin (2005), On the interactions of mineral dust, sea-salt particles, and clouds: A measurement and modeling study from the Mediterranean Israeli Dust Experiment campaign., *J. Geophys. Res.*, *110*(D20), 1–19, doi:10.1029/2005JD005810.

Leys, J. F., S. K. Heidenreich, C. L. Strong, G. H. McTainsh, and S. Quigley (2011), PM_{10} concentrations and mass transport during "Red Dawn" - Sydney 23 September 2009., *Aeolian Res.*, *3*(3), 327–342.

Li, Z., Z. Zang, Q. B. Li, Y. Chao, D. Chen, Z. Ye, Y. Liu, and K.-N. Liou (2012), A three-dimensional variational data assimilation system for multiple aerosol species with WRF/Chem and an application to PM2.5 prediction, *Atmos. Chemis. Phys. Discuss.*, *12*(5), 13,515–13,552.

Liao, H., and J. H. Seinfeld (1998), Radiative forcing by mineral dust aerosols: sensitivity to key variables, *J. Geophys. Res.*, *103*(D24), 31,637–31,645.

Lin, J. C., T. Matsui, R. A. Pielke Sr, and C. Kummerow (2006), Effects of biomass-burning-derived aerosols on precipitation and clouds in the Amazon Basin: a satellite-based empirical study, *J. Geophys. Res.*, *111*, D19,204.

Lin, Y. L., R. D. Farley, and H. D. Orville (1983), Bulk parameterization of the snow field in a cloud model, *J. Clim. Appl. Meteorol.*, *22*(6), 1065–1092.

Liou, K., and S. Ou (1989), The role of cloud microphysical processes in climate: An assessment from a one-dimensional perspective, *J. Geophys. Res.*, *94*(D6), 8599–8607.

Liu, Z., A. Omar, M. Vaughan, J. Hair, C. Kittaka, Y. Hu, K. Powell, C. Trepte, D. Winker, C. Hostetler, R. Ferrare, and R. Pierce (2008), CALIPSO lidar observations of the optical properties of Saharan dust: A case study of long-range transport, *J. Geophys. Res.*, *113*, D07,207, doi:10.1029/2007JD008878.

Mallet, M., P. Tulet, D. Serca, F. Solmon, O. Dubovik, J. Pelon, V. Pont, and O. Thouron (2009), Impact of dust aerosols on the radiative budget, surface heat fluxes, heating rate profiles and convective activity over West Africa during March 2006., *Atmos. Chem. Phys.*, *9*(18), 7143–7160.

Mansoori, J. (1995), Islamic Republic of Iran. In: Scott DA, editor. A directory of wetlands in the Middle East. available from http://www.earthspace.org/rl/es15056/scd01h.html.

Martonchik, J. V., D. J. Diner, R. Kahn, B. Gaitley, and B. N. Holben (2004), Comparison of MISR and AERONET aerosol optical depths over desert sites, *Geophys. Rese. Lett.*, *31*, L16,102, doi:10.1029/2004GL019807.

McCarthy, J. J., O. F. Canziani, N. A. Leary, D. J. Dokken, and K. S. e. White (Eds.) (2001), *Climate Change 2001: Impacts, Adaptations, and Vulnerability*, Cambridge University Press: Cambridge, UK.

McCormick, R. A., and J. H. Ludwig (1967), Climate modification by atmospheric aerosols, *Science (New York, N.Y.)*, *156*(3780), 1358–1359, doi:10.1126/science.156.3780.1358.

McGowan, H., and A. Clark (2008), Identification of dust transport pathways from Lake Eyre, Australia using Hysplit, *Atmos. Environ.*, *42*(29), 6915–6925, doi:10.1016/j.atmosenv.2008.05.053.

McGowan, H. A., and J. Soderholm (2012), Laser ceilometer measurements of Australian dust storm highlight need for reassessment of atmospheric dust plume loads, *Geophys. Res. Lett.*, *39*, L02,804, doi: 10.1029/2011GL050319.

McGowan, H. A., G. H. McTainsh, P. ZawarReza, and A. P. Sturman (2000), Identifying regional dust transport pathways: application of kinematic trajectory modelling to a transtasman case, *Earth Surf. Proc. Landforms*, *25*(6), 633–647.

McGowan, H. A., B. Kamber, G. H. McTainsh, and S. K. Marx (2005), High resolution provenancing of long travelled dust deposited on the Southern Alps, New Zealand, *Geomorphology*, *69*(1-4), 208–221.

McKendry, I. G., J. P. Hacker, R. Stull, S. Sakiyama, D. Mignacca, and K. Reid (2001), Long-range transport of Asian dust to the Lower Fraser Valley, British columbia, Canada., *J. Geophys. Res.*, *106*(D16), 18,361–18,370, doi:10.1029/2000JD900359.

McTainsh, G., Y. Chan, H. McGowan, J. Leys, and K. Tews (2005), The 23rd October 2002 dust storm in eastern Australia: characteristics and meteorological conditions., *Atmos. Environ.*, *39*(7), 1227–1236.

Miller, R. L., and I. Tegen (1998), Climate response to soil dust aerosols., *J. Climate*, *11*(12), 3247–3267.

Miller, R. L., and I. Tegen (1999), Radiative forcing of a tropical direct circulation by soil dust aerosols., *J. Atmos. Sci.*, *56*(14), 2403–2433.

Miller, R. L., I. Tegen, and J. Perlwitz (2004a), Surface radiative forcing by soil dust aerosols and the hydrologic cycle, *J. Geophys. Res.*, *109*, D04,203, doi:10.1029/2003JD004085.

Miller, R. L., J. Perlwitz, and I. Tegen (2004b), Feedback upon dust emission by dust radiative forcing through the planetary boundary layer., *J. Geophys. Res.*, *109*, D24,209, doi:10.1029/2004JD004912.

Miller, R. L., R. V. Cakmur, J. Perlwitz, I. V. Geogdzhayev, P. Ginoux, D. Koch, K. E. Kohfeld, C. Prigent, R. Ruedy, G. A. Schmidt, and I. Tegen (2006), Mineral dust aerosols in the NASA Goddard Institute for Space Sciences ModelE atmospheric general circulation model, *J. Geophys. Res.*, *111*, D06,208, doi:10.1029/2005JD005796.

Mitchell, R. M., S. K. Campbell, and Y. Qin (2010), Recent increase in aerosol loading over the Australian arid zone, *Atmos. Chemis. Phys.*, *10*(4), 1689–1699, doi:10.5194/acpd-9-21619-2009.

Mlawer, E. J., S. J. Taubman, P. D. Brown, M. J. Iacono, and S. A. Clough (1997), Radiative transfer for inhomogeneous atmospheres: RRTM, a validated correlated-k model for the longwave, *J. Geophys. Res.*, *102*(D14), 16,663–16,682.

Morrison, H., G. Thompson, and V. Tatarskii (2009), Impact of cloud microphysics on the development of trailing stratiform precipitation in a simulated squall line: Comparison of one- and two-moment schemes, *Mon. Weather Rev.*, *137*(3), 991–1007.

Moulin, C., and I. Chiapello (2006), Control of atmospheric export of dust from North Africa by the North Atlantic Oscillation., *Geophys. Res. Lett.*, *33*(18), 691–694.

Nakanishi, M., and H. Niino (2004), An improved MellorYamada level-3 model with condensation physics: Its design and verification, *Boundary-Layer Meteorol.*, *112*(1), 1–31.

Obukhov, A. M. (1971), Turbulence in an atmosphere with a non-uniform temperature, *Boundary-Layer Meteorol.*, *2*(1), 7–29.

Perlwitz, J., I. Tegen, and R. L. Miller (2001), Interactive soil dust aerosol model in the GISS GCM 1. Sensitivity of the soil dust cycle to radiative properties of soil dust aerosols, *J. Geophys. Res.*, *106*(D16), 18,167–18,192, doi:10.1029/2000JD900668.

Perry, K. D., T. A. Cahill, R. A. Eldred, D. D. Dutcher, and T. E. Gill (1997), Long-range transport of North African dust to the eastern United States, *J. Geophys. Res.*, *102*(D10), 11,225–11,238, doi:10.1029/97JD00260.

Petrenko, M., C. Ichoku, and G. Leptoukh (2012), Multi-sensor Aerosol Products Sampling System (MAPSS), *Atmos. Measur. Techniq.*, *5*, 913–926, doi:10.5194/amt-5-913-2012.

Podgorny, I. A., and V. Ramanathan (2001), A modeling study of the direct effect of aerosols over the tropical Indian Ocean, *J. Geophys. Res.*, *106*(D20), 24,097–24,105.

Pope, C. A., R. T. Burnett, M. J. Thun, E. E. Calle, D. Krewski, K. Ito, and G. D. Thurston (2002), Lung cancer, cardiopulmonary mortality, and long-term exposure to fine particulate air pollution, *J. American Medical Assoc.*, *287*(9), 1132–1141.

Prospero, J. M. (1999), Long-term measurements of the transport of African mineral dust to the southeastern United States: Implications for regional air quality, *J. Geophys. Res.*, *104*(D13), 15,917–15,927.

Prospero, J. M., and P. J. Lamb (2003), African droughts and dust transport to the Caribbean: Climate change implications, *Science*, *302*(5647), 1024–1027.

Prospero, J. M., P. Ginoux, O. Torres, S. E. Nicholson, and T. E. Gill (2002), Environmental characterization of global sources of atmospheric soil dust identified with the Nimbus 7 Total Ozone Mapping Spectrometer (TOMS) absorbing aerosol product., *Rev. Geophys.*, *40*(1), 1002, doi:10.1029/2000RG000095.

Qin, Y., and R. M. Mitchell (2009), Characterisation of episodic aerosol types over the Australian continent, *Atmos. Chem. Phys.*, *9*(6), 1943–1956, doi:10.5194/acp-9-1943-2009.

Quijano, A. L., I. N. Sokolik, and O. B. Toon (2000), Radiative heating rates and direct radiative forcing by mineral dust in cloudy atmospheric conditions., *J. Geophys. Res.*, *105*(D10), 12,207–12,219, doi: 10.1029/2000JD900047.

Radhi, M., M. A. Box, G. P. Box, R. M. Mitchell, D. D. Cohen, E. Stelcer, and M. D. Keywood (2010), Optical, physical and chemical characteristics of Australian continental aerosols: results from a field experiment, *Atmos. Chem. Phys.*, *10*(13), 5925–5942, doi:10.5194/acp-10-5925-2010.

Rajot, J. L., S. Triquet, A. Maman, N. Mouget, A. Zakou, P. Formenti, S. Alfaro, K. Desboeufs, S. Chevaillier, B. Chatenet, A. Gaudichet, E. Journet, and B. Marticorena (2008), AMMA dust experiment: An overview of measurements performed during the dry season special observation period (SOP0) at the Banizoumbou (Niger) supersite, *J. Geophys. Res.*, *113*(D23), D00C14.

Remer, L. A., Y. J. Kaufman, D. Tanre, S. Mattoo, D. A. Chu, J. V. Martins, R. R. Li, C. Ichoku, R. C. Levy, R. G. Kleidman, T. F. Eck, E. Vermote, and B. N. Holben (2005), The MODIS aerosol algorithm, products, and validation, *J. Atmos. Sci.*, *62*(4), 947–973.

Rosenfeld, D. (1999), TRMM observed first direct evidence of smoke from forest fires inhibiting rainfall, *Geophys. Res. Lett.*, *26*(20), 3105–3108.

Rosenfeld, D. (2000), Suppression of rain and snow by urban and industrial air pollution, *Science*, *287*(5459), 1793–1796, doi:10.1126/science.287.5459.1793.

Rosenfeld, D., and W. Woodley (2000), Deep convective clouds with sustained supercooled liquid water down to -37.5 degrees C, *Nature*, *405*(6785), 440–442.

Rosenfeld, D., U. Lohmann, G. Raga, C. O'Dowd, M. Kulmala, S. Fuzzi, A. Reissell, and M. Andreae (2008), Flood or drought: *H*ow do aerosols affect precipitation?., *Science*, *321*(5894), 1309–1313.

Rotstayn, L. D., M. D. Keywood, B. W. Forgan, A. J. Gabric, I. E. Galbally, J. L. Gras, A. K. Luhar, G. H. McTainsh, R. M. Mitchell, and S. A. Young (2009), Possible impacts of anthropogenic and natural aerosols on Australian climate: a review, *Int. J. Climatol.*, *29*(4), 461–479.

Rotstayn, L. D., M. A. Collier, M. R. Dix, Y. Feng, H. B. Gordon, S. P. O'Farrell, I. N. Smith, and J. Syktus (2010), Improved simulation of Australian climate and ENSO-related rainfall variability in a global climate model with an interactive aerosol treatment, *Int. J. Climatol.*, *30*(7), 1067–1088, doi:10.1002/joc.1952.

Rotstayn, L. D., M. A. Collier, R. M. Mitchell, Y. Qin, S. K. Campbell, and S. M. Dravitzki (2011), Simulated enhancement of ENSO-related rainfall variability due to Australian dust, *Atmos. Chemis. Phys.*, *11*(13), 6575–6592, doi:10.5194/acp-11-6575-2011.

Seinfeld, J. H., and S. N. Pandid (1997), *Atmos. Chemis. Phys.*, John Wiley, New York.

Shao, Y. (2008), *Physics and Modelling of Wind Erosion*, vol. 37., Springer Science, New York.

Shao, Y., J. F. Leys, G. H. McTainsh, and K. Tews (2007), Numerical simulation of the October 2002 dust event in Australia, *J. Geophys. Res.*, *112*, D08,207, doi:10.1029/2006JD007767.

Shaw, W. J., K. J. Allwine, B. J. Fritz, F. C. Rutz, J. P. Rishel, and E. G. Chapman (2008), An evaluation of the wind erosion module in DUSTRAN., *Atmos. Environ.*, *42*(8), 1907–1921.

Sinclair, V. A., S. L. Gray, and S. E. Belcher (2008), Boundary-layer ventilation by baroclinic life cycles, *Q. J. R. Meteorol. Soc.*, *134*(635), 1409–1424.

Sinclair, V. A., S. E. Belcher, and S. L. Gray (2010), Synoptic controls on boundary-layer characteristics, *Boundary-Layer Meteorol.*, *134*(3), 387–409.

Sokolik, I., and O. Toon (1996), Direct radiative forcing by anthropogenic airborne mineral aerosols., *Nature*, *381*(6584), 681–683.

Sokolik, I. N., D. M. Winker, G. Bergametti, D. A. Gillette, G. Carmichael, Y. J. Kaufman, L. Gomes, L. Schuetz, and J. E. Penner (2001), Introduction to special section: Outstanding problems in quantifying the radiative impacts of mineral dust, *J. Geophys. Res.*, *106*(D16), 18,015–18,027.

Solomos, S., G. Kallos, J. Kushta, M. Astitha, C. Tremback, A. Nenes, and Z. Levin (2011), An integrated modeling study on the effects of mineral dust and sea salt particles on clouds and precipitation, *Atmos. Chemis. Phys.*, *11*(2), 873–892, doi:10.5194/acp-11-873-2011.

Sun, J. M., M. Y. Zhang, and T. S. Liu (2001), Spatial and temporal characteristics of dust storms in China and its surrounding regions, 1960-1999: Relations to source area and climate, *J. Geophys. Res.*, *106*(D10), 10,325–10,333.

Takemura, T., I. Uno, T. Nakajima, A. Higurashi, and I. Sano (2002), Modeling study of long-range transport of Asian dust and anthropogenic aerosols from East Asia, *Geophys. Res. Lett.*, *29*(24), 2158.

Tao, W. K., J. P. Chen, Z. Q. Li, C. Wang, and C. D. Zhang (2012), Impact of aerosols on convective clouds and precipitation, *Rev. Geophys.*, *50*, RG2001, doi:10.1029/2011RG000369.

Targino, A. C., R. Krejci, K. J. Noone, and P. Glantz (2006), Single particle analysis of ice crystal residuals observed in orographic wave clouds over scandinavia during INTACC experiment, *Atmos. Chem. Phys.*, *6*(7), 1977–1990.

Tegen, I. (2003), Modeling the mineral dust aerosol cycle in the climate system, *Quaternary Sci. Rev.*, *22*(18), 1821–1834, doi:10.1016/S0277-3791(03)00163-X.

Tegen, I., and I. Fung (1994), Modeling of mineral dust in the atmosphere: Sources, transport, and optical thickness, *J. Geophys. Res.*, *99*(D11), 22,897–22,914.

Tegen, I., and I. Fung (1995), Contribution to the atmospheric mineral aerosol load from land-surface modification., *J. Geophys. Res.*, *100*(D9), 18,707–18,726, doi:10.1029/95JD02051.

Tegen, I., A. Lacis, and I. Fung (1996), The influence on climate forcing of mineral aerosols from disturbed soils., *Nature*, *380*(6573), 419–422, doi:10.1038/380419a0.

Tegen, I., M. Werner, S. P. Harrison, and K. K. E. (2004), Relative importance of climate and land use in determining present and future global soil dust emission., *Geophys. Res. Lett.*, *31*, L05,105, doi: 10.1029/2003GL019216.

Teller, A., and Z. Levin (2006), The effects of aerosols on precipitation and dimensions of subtropical clouds: a sensitivity study using a numerical cloud model, *Atmos. Chem. Phys.*, *6*(1), 67–80.

Tesche, M., S. Gross, A. Ansmann, D. Muller, D. Althausen, V. Fredenthaler, and M. Esselborn (2011), Profiling of Saharan dust and biomassburning smoke with multiwavelength polarization Raman lidar at Cape Verde, *Tellus B*, *63*(4), 649–676.

Textor, C., M. Schulz, S. Guibert, S. Kinne, Y. Balkanski, S. Bauer, T. Berntsen, T. Berglen, O. Boucher, M. Chin, F. Dentener, T. Diehl, R. Easter, H. Feichter, D. Fillmore, S. Ghan, P. Ginoux, S. Gong, J. E. Kristjansson, M. Krol, A. Lauer, J. Lamarque, X. Liu, V. Montanaro, G. Myhre, J. Penner, G. Pitari, S. Reddy, O. Seland, P. Stier, T. Takemura, and X. Tie (2006), Analysis and quantification of the diversities of aerosol life cycles within Aerocom, *Atmos. Chemis. Phys.*, *6*(7), 1777–1813, doi: 10.5194/acp-6-1777-2006.

Trewin, B., and H. Vermont (2010), Changes in the frequency of record temperatures in Australia, 1957-2009, *Aus. Meteorol. Oceanogr. J.*, *60*(2), 113–119.

Tsamalis, C., and A. Chedin (2013), Dust aerosol optical depth above Sahara and Arabian Peninsula from CALIOP: comparison with MODIS and MISR, paper presented at CALIPSO, CloudSat, EarthCARE J. Work., Paris, France, 18-22 June 2012, *15*, EGU General Assembly 2013.

Tummon, F., F. Solmon, C. Liousse, and M. Tadross (2010), Simulation of the direct and semidirect aerosol effects on the southern Africa regional climate during the biomass burning season, *J. Geophys. Res.*, *115*, D19,206, doi:10.1029/2009JD013738.

Twomey, S. (1974), Pollution and the planetary albedo, *Atmos. Environ.*, *8*, 1251–1256.

Twomey, S. (1977), The influence of pollution on the shortwave albedo of clouds, *J. Atmos. Sci.*, *34*(7), 1149–1152.

Twomey, S. A., M. Piepgrass, and T. L. Wolfe (1984), An assessment of the impact of pollution on global cloud albedo, *Tellus B*, *36B*(5), 356–366.

Uno, I., K. Eguchi, K. Yumimoto, T. Takemura, A. Shimizu, M. Uematsu, Z. Liu, Z. Wang, Y. Hara, and N. Sugimoto (2009), Asian dust transported one full circuit around the globe, *Nat. Geosci.*, *2*(8), 557–560, doi:10.1038/NGEO583.

Wandinger, U., M. Tesche, P. Seifert, A. Ansmann, D. Muller, and D. Althausen (2010), Size matters: Influence of multiple scattering on CALIPSO light-extinction profiling in desert dust, *Geophys. Res. Lett.*, *37*, L10,801, doi:10.1029/2010GL042815.

Wesely, M. L. (1989), Parameterization of surface resistances to gaseous dry deposition in regional-scale numerical models, *Atmos. Environ.*, *41*, 52–63.

Wild, O., X. Zhu, and M. J. Prather (2000), Fast-J: Accurate simulation of in- and below-cloud photolysis in tropospheric chemical models, *J. Atmos. Chem.*, *37*(3), 245–282.

Winker, D. M., W. H. Hunt, and M. J. McGill (2007), Initial performance assessment of CALIOP, *Geophys. Res. Lett.*, *34*, L19,803, doi:10.1029/2007GL030135.

Woodward, S. (2001), Modeling the atmospheric life cycle and radiative impact of mineral dust in the Hadley Centre climate model, *J. Geophys. Res.*, *106*(D16), 18,155–18,166, doi:10.1029/2000JD900795.

Yoshioka, M., N. M. Mahowald, A. J. Conley, W. D. Collins, D. W. Fillmore, C. S. Zender, and D. B. Coleman (2007), Impact of desert dust radiative forcing on Sahel precipitation: Relative importance of dust compared to sea surface temperature variations, vegetation changes, and greenhouse gas warming, *J. Climate*, *20*(8), 1445–1467.

Yu, H., Y. J. Kaufman, M. Chin, G. Feingold, L. A. Remer, T. L. Anderson, Y. Balkanski, N. Bellouin, O. Boucher, S. Christopher, P. DeCola, R. Kahn, D. Koch, N. Loeb, M. S. Reddy, M. Schulz, T. Takemura, and M. Zhou (2006), A review of measurement-based assessments of the aerosol direct radiative effect and forcing, *Atmos. Chem. Phys.*, *6*, 613–666, doi:10.5194/acp-6-613-2006.

Yue, X., H. Wang, Z. Wang, and K. Fan (2009), Simulation of dust aerosol radiative feedback using the Global Transport Model of Dust: 1. Dust cycle and validation, *J. Geophys. Res.*, *114*, D10,202.

Yue, X., H. Wang, H. Liao, and K. Fan (2010), Simulation of dust aerosol radiative feedback using the GMOD: 2. Dust-climate interactions, *J. Geophys. Res.*, *115*(D4), D10,202, doi:10.1029/2008JD010995.

Zaveri, R. A., and L. K. Peters (1999), A new lumped structure photochemical mechanism for large-scale applications, *J. Geophys. Res.*, *104*(D23), 30,387–30,415, doi:10.1029/1999JD900876.

Zaveri, R. A., R. C. Easter, J. D. Fast, and L. K. Peters (2008), Model for simulating aerosol interactions and chemistry (MOSAIC), *J. Geophys. Res.*, *113*, D13,204.

Zender, C. S., H. Bian, and D. Newman (2003), Mineral Dust Entrainment and Deposition (DEAD) model: Description and 1990s dust climatology, *J. Geophys. Res.*, *108*(D14), 4416, doi:10.1029/2002JD002775.

Zender, C. S., R. L. Miller, and I. Tegen (2004), Quantifying mineral dust mass budgets: Terminology, constraints, and current estimates, *EOS Transactions*, *85*(48), 509–512.

Zhang, Y. (2008), Online-coupled meteorology and chemistry models: history, current status, and outlook., *Atmos. Chem. Phys.*, *8*(11), 2895–2932.

Zhao, C., X. Liu, L. Leung, B. Johnson, S. McFarlane, W. Gustafson, J. Fast, and R. Easter (2010), The spatial distribution of mineral dust and its shortwave radiative forcing over North Africa: modeling sensitivities to dust emissions and aerosol size treatments, *Atmos. Chemis. Phys.*, *10*(18), 8821–8838, doi:10.5194/acp-10-8821-2010.

Zhao, C., X. Liu, L. R. Leung, and S. Hagos (2011), Radiative impact of mineral dust on monsoon precipitation variability over West Africa, *Atmos. Chem. Phys.*, *11*(5), 1879–1893, doi:10.5194/acp-11-1879-2011.

Zhao, M., and S. W. Running (2010), Drought-induced reduction in global terrestrial net primary production from 2000 through 2009, *Science*, *329*(5994), 940–943, doi:10.1126/science.1192666.

Zhu, A., V. Ramanathan, F. Li, and D. Kim (2007), Dust plumes over the Pacific, Indian, and Atlantic oceans: Climatology and radiative impact, *J. Geophys. Res.*, *112*, D16,208, doi:10.1029/2007JD008427.